Exploration des interactions nanosurface-biologiques/environnementales par Förster resonance energy transfer des complexes de lanthanides vers les points quantiques

Ruifang Su

Normandie Université

UNIVERSITÉ DE ROUEN NORMANDIE

THÈSE

Pour obtenir le diplôme de doctorat

Spécialité CHIMIE

Préparée au sein de l'Université de Rouen Normandie

Probing nanosurface-environment interactions by FRET from lanthanide complexes to quantum dots

Présentée et soutenue par
RUIFANG SU

Thèse soutenue le 06/12/2023 devant le jury composé de		
MME ALINE NONAT	CHARGE DE RECHERCHE, UNIVERSITE STRASBOURG	Rapporteur du jury
MME UTE RESCH-GENGER	DIRECTEUR DE RECHERCHE, BAM Institute for Materials Research and Testing	Rapporteur du jury
M. XAVIER FRANCK	DIRECTEUR DE RECHERCHE, Université de Rouen Normandie	Membre du jury
M. THIBAULT GALLAVARDIN	CHARGE DE RECHERCHE, Université de Rouen Normandie	Membre du jury
MME CHLOÉ GRAZON	CHARGE DE RECHERCHE, UNIVERSITE DE BORDEAUX	Membre du jury
M. THOMAS JUST SØRENSEN	PROFESSEUR DES UNIVERSITES, Université de Copenhague (Danemark)	Membre du jury
M. NIKO HILDEBRANDT	PROFESSEUR DES UNIVERSITES, Université de Rouen Normandie	Directeur de thèse

Thèse dirigée par NIKO HILDEBRANDT (CHIMIE ORGANIQUE, BIOORGANIQUE, REACTIVITE, ANALYSE)

ED 508 NC Normande de Chimie

Laboratoire Cobra Chimie organique, Bioorganique, Réactivité et Analyse.

Pour obtenir le diplôme de doctorat

Spécialité CHIMIE

Préparée au sein de l'Université de Rouen Normandie et à l'Université de Copenhague

Probing nanosurface-biological/environment interactions by Förster resonance energy transfer from lanthanide complexes to quantum dots

Présentée et soutenue par

Ruifang SU

Thèse soutenue le 06/12/2023 devant le jury composé de		
MME. Aline NONAT	Chargé de recherche CNRS Université de Strasbourg	Rapporteur et examinatrice
MME. Ute RESCH-GENGER	Directeur de recherche Bundesanstalt für Materialforschung und-prüfung (BAM) (Allemagne)	Rapporteur et examinatrice
M. Xavier FRANCK	Directeur de recherche CNRS Université de Rouen Normandie	Président du jury
M. Thibault GALLAVARDIN	Chargé de recherche CNRS Université de Rouen Normandie	Membre invité
MME. Chloé GRAZON	Chargé de recherche CNRS Université de Bordeaux	Examinatrice
M. Thomas Just SØRENSEN	Professeur Université de Copenhague (Danemark)	Directeur de thèse
M. Niko HILDEBRANDT	Professeur Université de Rouen Normandie	Directeur de thèse

Thèse dirigée par Prof. Niko HILDEBRANDT (Université de Rouen Normandie) et Prof. Thomas Just SØRENSEN (Université de Copenhague)

To obtain the Doctorate Degree

in CHEMISTRY

Prepared at the Université de Rouen Normandie and the University of Copenhagen

Probing nanosurface-biological/environment interactions by Förster resonance energy transfer from lanthanide complexes to quantum dots

Presented and defended by

Ruifang SU

Thesis defended on 06/12/2023 before the committee composed of		
MME. Aline NONAT	CNRS researcher Université de Strasbourg	Thesis reviewer and examiner
MME. Ute RESCH-GENGER	Research director Bundesanstalt für Materialforschung und-prüfung (BAM) (Germany)	Thesis reviewer and examiner
M. Xavier FRANCK	CNRS researcher director Université de Rouen Normandie	President of the jury
M. Thibault GALLAVARDIN	CNRS researcher Université de Rouen Normandie	Invited member
MME. Chloé GRAZON	CNRS researcher Université de Bordeaux	Examiner
M. Thomas Just SØRENSEN	Professor University of Copenhagen (Denmark)	Thesis supervisor
M. Niko HILDEBRANDT	Professor Université de Rouen Normandie	Thesis supervisor

Thesis supervised by Prof. Niko HILDEBRANDT (Université de Rouen Normandie) and Prof. Thomas Just SØRENSEN (University of Copenhagen)

ACKNOWLEDGMENT

Acknowledgment

First, I would like to express my heartfelt gratitude to my supervisor, Prof. Dr. Niko Hildebrandt, our Captain FRET! He gave me the chance to join this inclusive, international, and harmonious group, where I have studied and worked in a supportive and joyful atmosphere. His patient guidance and unwavering support not only facilitated the smooth progress of my project but also gave me the courage to face challenges and overcome difficulties. His dedication and passion for research, innovative and rich ideas, cheerful communication style, and caring attitude towards students have positively impacted me. He is a great role model for my learning.

I sincerely appreciate my supervisor at the University of Copenhagen, Prof. Dr. Thomas Just Sørensen. I am thankful for his warm welcome into the vibrant and cooperative TJS group. Throughout my studies there, he devoted a substantial amount of time and effort to guide and advance my research and offered valuable insights into career planning and personal development. His broad international perspective, cutting-edge academic expertise, and selfless sharing and communication have greatly benefited me.

I sincerely thank all collaborators and co-authors of my publications. Special thanks to Dr. Igor Medintz, Prof. Dr. Xue Qiu, and Dr. Kimihiro Susumu for their patient and helpful replies to my questions regarding the experimental materials.

I would like to express my sincere thanks to Dr. Aline Nonat and Dr. Ute Resch-Genger for being the reviewers of my thesis.

I am very grateful for the help and support provided by past and current members of the nanoFRET group and TJS group. Special thanks to Dr. Jiajia Guo, Dr. Laura Francés-Soriano, Dr. Mariia Dekaliuk, and Dr. Jingyue Xu for their scientific and technical guidance at the beginning of my studies and their practical tips for living in France; to Federico Pini, Peremobowei Iyanu Diriwari, Capucine Chaar for their support, companionship, and assistance during my Ph.D. study and in dealing with the administration; and to Dr. Laura Grenier, Dr. Nicolaj Kofod, Dr. Lea Nielsen, Villads Nielsen, and Magnus Wied for their technical guidance and encouragement. Thanks to all my group members for the enjoyable work and coffee

moments we shared.

My sincere thank goes to Asst. Prof. Junsheng Chen for answering my questions about quantum dot properties; to Yang Wang and Vassillis Mouchtouris for working late together in the lab and sharing delicious food with me.

My deep gratitude also goes to my dear friend, Dr. Anne Nsubuga, for her assistance with the French translation in this thesis, and for her unwavering kindness and support. Sincere thanks to my dear friend, Nour Fayad, for her warm companionship during lab work, conferences, and travel, and for her consistent, sincere assistance, and concern for me. They make my time in Rouen enjoyable and unforgettable.

I gratefully acknowledge the financial support from XL-Chem graduate school (ANR-18-EURE-0020 XL CHEM), the Region Normandie, and the University of Copenhagen.

Lastly, I would like to thank my lovely family and friends for their support, care, and companionship, and my boyfriend Junyan Lin for always being by my side, supporting and encouraging me.

LIST OF PUBLICATIONS

List of publications

Original publications (including publications in preparation)

1. **Ruifang Su**, Nicolaj Kofod, Kimihiro Susumu, Igor L. Medintz, Niko Hildebrandt, and Thomas Just Sørensen. Quantum dot-based FRET assays for simultaneous temperature-DNA sensing. In preparation.

2. **Ruifang Su**, Kimihiro Susumu, Igor L. Medintz, Thomas Just Sørensen, and Niko Hildebrandt. Multiplexed picomolar nucleic acid sensing using time-resolved terbium-to-quantum dot FRET. In preparation.

3. Laura Francès Soriano, **Ruifang Su**, P. Iyanu Diriwari, Thomas Just Sørensen, Sebastian A. Diaz, Igor L. Medintz, and Niko Hildebrandt. FRET Materials for Biosensing. Invited review by *Angewandte Chemie International Edition*. In preparation.

4. **Ruifang Su**, Yu-Tang Wu, Sofia Doulkeridou, Xue Qiu, Thomas Just Sørensen, Kimihiro Susumu, Igor L. Medintz, Paul M. P. van Bergen en Henegouwen, and Niko Hildebrandt. A Nanobody-on-Quantum Dot Displacement Assay for Rapid and Sensitive Quantification of the Epidermal Growth Factor Receptor (EGFR). *Angewandte Chemie International Edition* **2022**, 61(33), e202207797.

5. Hui-Jun Fu, **Ruifang Su**, Lin Luo, Zi-Jian Chen, Thomas Just Sørensen, Niko Hildebrandt, and Zhen-Lin Xu. Rapid and Wash-Free Time-Gated FRET Histamine Assays Using Antibodies and Aptamers. *ACS Sensors* **2022**, 7, 1113-1121.

6. Ying Li, **Ruifang Su**, Hongxia Li, Jiajia Guo, Niko Hildebrandt, and Chunyan Sun. Fluorescent Aptasensors: Design Strategies and Applications in Analyzing Chemical Contamination of Food. *Analytical Chemistry* **2022**, 94 (1), 193-224.

Oral presentations

1. **Ruifang Su**, Yu-Tang Wu, Sofia Doulkeridou, Xue Qiu, Thomas Just Sørensen, Kimihiro Susumu, Igor L. Medintz, Paul M. P. van Bergen en Henegouwen, and Niko Hildebrandt.

Nanobody-on-quantum dot displacement assay for EGFR based on Förster resonance energy transfer. *16ème édition des Journées Nord Ouest Européennes des Jeunes Chercheurs*, Caen, France, **09/06/2022**.

2. **Ruifang Su**, Thomas Just Sørensen, Kimihiro Susumu, Igor L. Medintz, and Niko Hildebrandt. DNA hybridization-modulated terbium-to-quantum dot FRET barcoding for temporal multiplexing and imaging. *FRET Community Satellite Meeting at MAF*, Gothenburg, Sweden, **15/09/2022**.

3. **Ruifang Su**, Yu-Tang Wu, Sofia Doulkeridou, Xue Qiu, Thomas Just Sørensen, Kimihiro Susumu, Igor L. Medintz, Paul M. P. van Bergen en Henegouwen, and Niko Hildebrandt. Nanobody displacement immunoassay for EGFR based on Tb-to-quantum dots FRET. *6th Inorganic Graduate Student Seminar*, Copenhagen, Denmark, **28/04/2023**.

Poster presentations

1. **Ruifang Su**, Yu-Tang Wu, Sofia Doulkeridou, Xue Qiu, Thomas Just Sørensen, Kimihiro Susumu, Igor L. Medintz, Paul M. P. van Bergen en Henegouwen, and Niko Hildebrandt. Nanobody-on-quantum dot FRET-based immunoassay for simple and sensitive detection of EGFR. *17th Conference on Methods and Applications of Fluorescence (MAF)*, Gothenburg, Sweden, **12/09/2022**.

2. **Ruifang Su**, Kimihiro Susumu, Igor L. Medintz, Niko Hildebrandt, and Thomas Just Sørensen. Temperature/peptide-DNA dual sensing based on terbium-to-quantum dot Förster resonance energy transfer. *11th International Conference on f-elements (ICFE-11)*, Strasbourg, France, **25/08/2023**.

3. **Ruifang Su**, Kimihiro Susumu, Igor L. Medintz, Thomas Just Sørensen and Niko Hildebrandt. Temporal multiplexing of ssDNA based on tunable terbium-to-quantum dot Förster resonance energy transfer. *20th International Conference on Luminescence*, Paris, France, **30/08/2023**.

CONTENTS

Contents

CHAPTER 1

Introduction

1. Introduction

The Nobel Prize in Chemistry in 2023 was awarded to Moungi G. Bawendi, Louis E. Brus, and Alexei I. Ekimov, who made significant contributions to the discovery and synthesis of quantum dots (QDs), and "added colour to nanotechnology" [1]. These tiny, colorful, and unique nanoparticles offer innovative applications in various domains and play a crucial role in advancing materials science, photonics, energy technologies, and life sciences.

Due to the quantum confinement effect, QDs exhibit exceptional photophysical properties superior to conventional organic dyes [2], including high absorption cross sections, narrow and symmetric photoluminescence (PL) emission peaks, and size-dependent PL emission wavelengths, which makes them favorable alternatives of traditional dyes for biosensing and imaging [3], [4]. Apart from the replacement of organic dyes, QDs have also gained increasing attention as versatile energy transfer (ET) candidates (donors or acceptors) within a nano-scale biological context [5]. Due to the nontrivial surface areas of QDs, functional biomolecules (e.g., proteins, antibodies, single-stranded (ss)DNA) and/or luminescent materials (ET donors or acceptors) can be conjugated to QDs, which allows nano-surface biological or environmental probing [5], [6].

In the ET-based assays, Förster resonance energy transfer (FRET) has become one of the most promising technologies for biosensing because of its high distance sensitivity on a biomolecular interaction scale (ca. 1-20 nm) [7]. QDs have shown to be excellent FRET donors for a large variety of organic dyes, fluorescent proteins, polymers, and metal nanoparticles (NPs) [8]–[10]. However, organic dyes and fluorescent proteins often suffer from poor photostability and self-quenching, as well as the influence of auto-fluorescence background. To overcome these drawbacks, a FRET pair composed of lanthanide-based compounds or NPs donors and QDs as acceptors has been proposed and advanced [11], [12]. Compared with organic dyes and fluorescent proteins, QDs possess great photostability and brightness, and the lanthanides-based donors exhibit super-long PL lifetime (up to milliseconds) [13], [14], which allows the time-resolved (TR) or time-gated (TG) detection to suppress all the auto-fluorescence background (nanoseconds scale). Notably, the PL lifetime of FRET-quenched donors or FRET-sensitized acceptors can be tuned by FRET efficiencies, which provide great potential for temporal

multiplexing [15]. Besides, both lanthanide probes and QDs possess narrow, distinguishable emission peaks, which provides the possibility of spectral multiplexing by using various QDs as multiple acceptors [16].

Several sophisticated concepts of lanthanide and QD-based luminescent biosensing or multiple probing have been presented [17]–[19]. Although the proofs-of-concept showed highly promising features for advanced sensing applications, their optimization, simplification, and adaption to daily use in a broad range of applications are challenges that still need to be overcome. Moreover, the influence of environmental changes (e.g., temperature) and biological interactions on the photophysical and energy transfer properties of lanthanides on NP surfaces has been largely underexplored. Therefore, this thesis aims to investigate the biomolecular interactions (taking protein binding and DNA hybridization as the representative cases) on QDs surface by lanthanide-to-QD FRET assays (a terbium complex was used as the representative lanthanide-based compound in this work) and the temperature effect on the QD-based FRET systems.

The thesis contains nine chapters. Following this introduction (**Chapter 1**), there is the research background (**Chapter 2**) on FRET theory, FRET applications, lanthanides, and QDs. **Chapters 3**, **4**, and **5** present three individual studies, including introduction, materials and methods, results and discussion, and conclusion. The summary and outlook of the whole work are discussed in **Chapter 6**, followed by the abbreviations, bibliography, and "Panorama du sujet en français".

In the first study, the QD-surface protein interactions probing based on terbium complex-to-QD FRET was investigated by taking the epidermal growth factor receptor (EGFR, an important biomarker for various kinds of human malignancies) [20], [21], as a protein model. Two small engineered nanobodies (NB1 and NB2) against EGFR were produced with different C-terminal tags (hexahistidine (His_6), biotin, and cysteine (Cys) tags). We show that they can be efficiently attached to three of the most widely used biocompatible QDs with three common surface coatings, compact zwitterionic ligands (CL4), amino-polyethylene-glycol (PEG), and streptavidin (sAv), respectively. To demonstrate the biosensing functionality of this versatile bioconjugation toolkit, three wash-free and rapid FRET sandwich immunoassays for the quantification of EGFR were developed. As shown in **Figure 1.1A**, NB2 are labeled with His_6

(NB2-H), Cys (NB2-C), and biotin (NB2-B) tags, respectively, while NB1 is labeled with Lumi4-Tb complex (Tb-NB1). Then NB2-H, NB2-B, and NB2-C are respectively attached onto QD625-CL4, QD705-sAv, and QD705-PEG, to form NB2-H-QD625-CL4, NB2-B-QD705-sAv, and NB2-C-QD705-PEG conjugates. Since NB1 and NB2 bind to different domains of EGFR noncompetitively, their conjugates were successfully used to detect the soluble EGFR (sEGFR, a prognostic and predictive biomarker for metastatic breast cancer) in immunological sandwich assays, with similar limit of detection (LOD) of 0.5±0.2 nM (NB2-C-QD705-PEG), 0.7±0.2 nM (NB2-B-QD705-sAv), and 0.8±0.2 nM (NB2-H-QD625-CL4) sEGFR, respectively. We then developed a new biosensing concept (**Figure 1.1B**), in which His_6-tagged NBs (NB1-H) were displaced from the QD surface by non-competitive binding of NB1 to EGFR. This new assay format, which required only a single type of NB and no QD bioconjugation, was applied for the quantification of sEGFR and soluble EGFR variant III (sEGFRvIII, a prognostic biomarker for glioblastoma). The detection limit of 80±20 pM (16±4 ng mL^{-1}) was 3-fold lower than the clinical cut-off concentration for sEGFR and up to 10-fold lower compared to the abovementioned three conventional sandwich FRET assays that required a pair of different nanobodies. The NB-displacement assay significantly decreases cost and labor (for antibody screening and production and bioconjugation), strongly facilitates assay-kit assembly and storage (only one type of Tb-NB conjugate and one type of unlabeled QD), provides rapid (mix-and-measure) analysis, and can quantify relevant biomarkers at clinically relevant concentrations.

My contribution to this study includes the design of the experiments, preparation of NB-Tb conjugates, optimization of reaction conditions, performance of displacement immunoassay experiments, data analysis and interpretation, and the writing of the manuscript. Dr. Yu-tang Wu contributed to the NB-QD conjugates preparation and sandwich immunoassay experiments. Sofia Doulkeridou prepared the nanobodies. Prof. Xue Qiu helped with the design of the study. Dr. Kimihiro Susumu prepared the QD625-CL4. All authors contributed to the editing and writing of the manuscript and approved its final version for the journal. (**Ruifang Su**, Yu-Tang Wu, Sofia Doulkeridou, Xue Qiu, Thomas Just Sørensen, Kimihiro Susumu, Igor L. Medintz, Paul M. P. van Bergen en Henegouwen, and Niko Hildebrandt. A Nanobody-on-Quantum Dot Displacement Assay for Rapid and Sensitive Quantification of the Epidermal Growth Factor

Receptor (EGFR). *Angewandte Chemie International Edition* **2022**, 61(33), e202207797. Paper 4 in the original publications list).

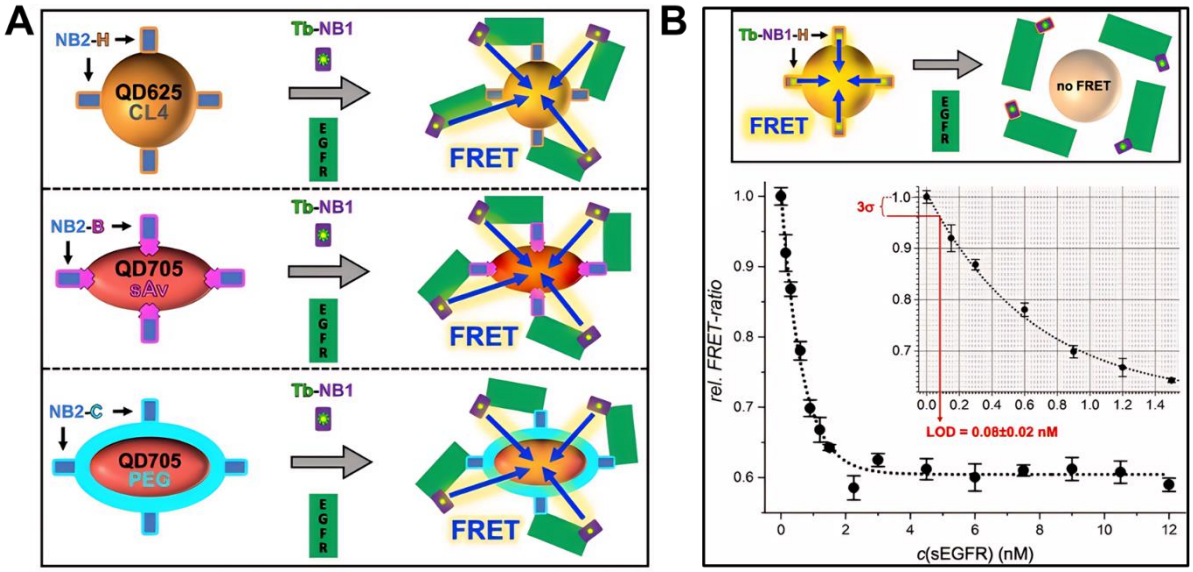

Figure 1.1. Schematic representation of immunoassays for EGFR detection. **(A)** Principle of the NB-based Tb-to-QD FRET sandwich immunoassays. **(B) Top**: Principle of Tb-to-QD FRET NB displacement immunoassays. **Bottom**: NB displacement FRET immunoassay calibration curves with a LOD of 0.08±0.02 nM sEGFR.

In the second study, a temporal multiplexing strategy is presented for DNA target sensing based on the TG PL measurement of three different Lumi4-Tb complex (Tb)-to-QD FRET probes with temporally distinct PL decays adjusted by the Tb-QD distance. Different Tb-QD FRET probes were functionalized by different peptide-cDNAs (part of the complementary DNA sequence of target DNA) and used as distinct PL probes. Magnetic beads (MBs) were functionalized with another cDNAs (another part of a complementary sequence of the target DNA) through biotin-streptavidin reaction. In the presence of corresponding target DNAs, different Tb-QD-peptide-cDNA probes can be immobilized onto MBs through DNA hybridization of peptide-cDNA, target DNA, and cDNA on MB (**Figure 1.2 left**). After magnetic separation and resuspension, all the background signal from free Tb-QD-FRET probes can be removed, and the TG measurements of Tb-QD probes on MB in distinct time windows after pulsed excitation can realize the autofluorescence-free, sensitive, and selective detection of different DNA targets (**Figure 1.2 right**). The results show that the PL intensities of different FRET probes in different time windows are increasing with the increasing

concentration of target DNA in each single sensing assay. Assay calibration curves were achieved by plotting the TG PL intensity of the FRET-sensitized QD acceptor of each probe as a function of corresponding target concentrations. The linear detection concentration range of target DNA1, 2, and 3 are 0.625 pM to 0.375 nM, 2.5 pM to 0.5 nM, and 6.25 pM to 2 nM, and the detection LODs are 0.56 pM, 0.94 pM, and 10.3 pM, respectively. These sensitivities allow us to distinguish concentration differences of a few pM of target DNAs over the entire dynamic concentration range. The temporal triplexing concept was successfully used in the selective, sensitive, and accurate recovery of the three different DNAs at varying low picomolar to nanomolar concentrations from eleven different samples.

My contribution to this study includes designing and executing experiments, analyzing data, and writing the manuscript. Dr. Kimihiro Susumu prepared QD625 (modified with CL4 ligands). All the other authors contributed to the experiment design and provided guidance. The manuscript is currently in preparation. (**Ruifang Su**, Kimihiro Susumu, Igor L. Medintz, Thomas Just Sørensen, and Niko Hildebrandt, Multiplexed picomolar nucleic acid sensing using time-resolved terbium-to-quantum dot FRET. Paper 2 in the original publications list).

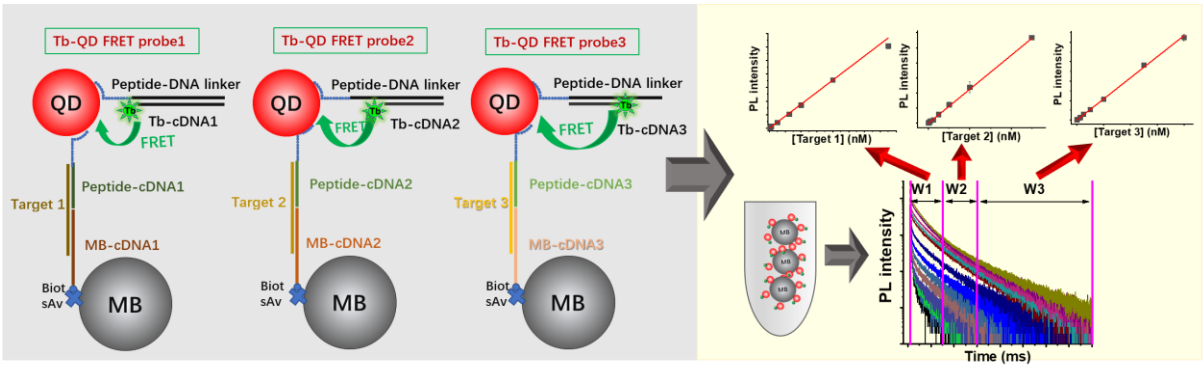

Figure 1.2. Schematic representation for temporal triplexing of DNAs based on Tb-QD FRET. **Left:** In the presence of target DNAs, peptide-cDNA of Tb-to-QD FRET probes and cDNA on MBs will hybridize with target DNA to form the Tb-QD-DNA-MB complexes. **Right:** After magnetic separation and resuspension, TG PL measurement from three time windows (W1, W2, and W3) of Tb-QD probes on MBs can realize the specific quantification of DNA targets.

In the third study, the temperature response of widely used water-soluble QDs (CdSe/ZnS-based core-shell QDs, functionalized with dihydrolipoic acid (DHLA)-based compact ligands) was analyzed by measuring their absorption and PL emission spectra under different

temperatures. By using the QDs as both the nanoplatforms and FRET donors or acceptors, two prototypical FRET-based biosensing assays were developed as shown in **Figure 1.3**. In the two FRET systems, peptide-DNA was attached to the QD surface through metal-polyhistidine coordination. Cyanine 5 (Cy5) or Lumi4-Tb-NHS (Tb) labeled DNAs could specifically hybridize with the DNA sequence in peptide-DNA, such that QD-peptide-dsDNA-Cy5/Tb FRET complexes were formed. The temperature response of QDs and its effect on the biosensing performances of the two assays were investigated by combining steady-state and TR PL measurements of the QD-based FRET signals. Results show that the PL intensity of QDs declines with the emission peak position shifting towards the red as temperature increases from 10 to 80 °C, which shows good reversibility. Continuous heating treatment induces partly irreversible PL quenching of QDs due to the surface oxidation reaction and particle precipitation and aggregation (when the temperature is over 60 °C). The temperature effect on QD-based assays can be eliminated by using a ratiometric FRET format (FRET ratio as the signal), which allows temperature-independent sensing of DNA targets. The PL intensity of QD donors or acceptors in FRET assays remains temperature sensitive, which can be used for simultaneous temperature sensing during DNA quantification. By combining the ratiometric FRET assay format with the temperature sensing capability of QDs, the target/temperature dual sensing can be realized. The results emphasized the importance of temperature control for QD-based PL assays and provided practically important guidance for their applications in the life sciences. The development of a biological target/temperature dual sensing strategy is conducive to expanding the applications of FRET systems in both biomedical and nano-surface environmental sensing.

My contribution to this study includes the design and execution of experiments, data analysis, and writing of the manuscript. Dr. Kimihiro Susumu prepared QD625 (modified with CL4 ligands). All the other authors contributed to the experiment design and provided guidance. The manuscript is currently in preparation. (**Ruifang Su**, Nicolaj Kofod, Kimihiro Susumu, Igor L. Medintz, Niko Hildebrandt, and Thomas Just Sørensen. Quantum dot-based FRET assays for simultaneous temperature-DNA sensing. Paper 1 in the original publications list).

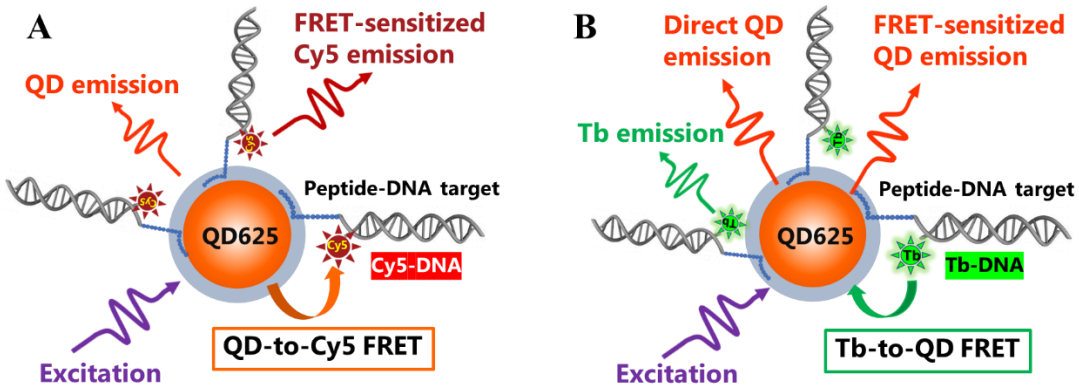

Figure 1.3 Principles of QD-based FRET. (A) Cy5-labeled DNA hybridizes to peptide-DNA attached to the QD625 surface, which leads to QD-to-Cy5 FRET. (B) In a similar design Tb-DNA hybridization to the peptide-DNA results in Tb-to-QD FRET.

CHAPTER 2

Background

2. Background

This chapter introduces Förster resonance energy transfer (FRET), the photophysical properties of luminescent lanthanides and semiconductor quantum dots (QDs), and examinations of their respective applications in FRET-based biosensing and diagnostics. Our research interests are towards the development of bioassays for nano-surface biomolecular interactions and environment sensing based on the time-resolved measurements of lanthanide (Ln)-to-QD FRET pairs, and the investigation of temperature-induced luminescent response of QDs, along with their consequent impact on QD-based FRET processes. Understanding these foundational research domains has inspired us to design higher sensitivity, background-free, and multifunctional biosensing strategies.

This chapter begins with the introduction of the FRET phenomenon and the theory behind it in **Section 2.1**. **Section 2.2** systematically overviews the application of FRET in homogenous immunoassays and the quantification of nucleic acid biomarkers. **Section 2.3** examines the outstanding photophysical properties of Ln and the advantages of using them as FRET donors. Finally, **Section 2.4** is devoted to a brief overview of QDs, including their photophysical properties, surface functionalization, and their applications in FRET as donors or acceptors.

2.1 Förster resonance energy transfer

2.1.1 Introduction

FRET is the non-radiative energy transfer from an excited fluorophore (donor) to a proximal ground state fluorophore (acceptor) via their dipole-dipole interactions. The phenomenon was first theoretically established in 1948 and named after the German scientist Theodor Förster [22], who was the first person to develop a quantitative theory to describe this nonradiative energy transfer. According to Förster theory, the following conditions are needed to observe FRET [23]: **(i)** Donor and acceptor fluorophores should have strong electronic transitions in the ultraviolet (UV), visible (Vis), or infrared (IR) region. **(ii)** The donor should emit at a reasonably high quantum yield. **(iii)** There should be a spectral overlap between donor emission and acceptor absorption. **(iv)** The orientation factor should not be 0. **(v)** Donor and acceptor should be at a reasonable distance (1-20 nm), where orbital overlap-related

mechanisms (for very short distances) and radiative mechanisms (for long distances) play minor roles. Under these conditions, energy can be transferred from the donor to the acceptor, resulting in PL quenching of the donor and PL sensitization of the acceptor (when the acceptor is luminescent).

FRET-based applications have expanded tremendously since the early 1990s, driven by significant advances in new fluorophores, detection methods, and instrumentation [3]. Due to the strong distance dependence of FRET (1-20 nm) in the biological interaction range, FRET has become a popular technique in many biological and biophysical fields, such as the quantification of bio-targets of interest (proteins, nucleic acids, metabolites, cells, and pathogens, etc.) [5], [23] and the detection of molecular dynamics in biophysics and molecular biology (DNA and protein interactions, and their conformational changes) [5]. This chapter will introduce the background theory of FRET (**Section 2.1.2**), which is mainly extracted from reference **[23]**.

2.1.2 FRET Theory

The theory behind FRET was established in the 1940s, which was mainly contributed by Theodor Förster [24], [25]. In FRET, the excited donor non-radiatively transfers (without photon appearing) energy to a ground-state acceptor in a resonance condition, where the luminescent energy from the donor should be equal to the absorption energy of the acceptor. The efficiency of this energy transfer (E_{FRET}) is dependent on the donor-acceptor distance (R), which is typically in a range of 1-20 nm (where the orbital overlap-related mechanisms and radiative mechanisms play minor roles), indicating the donor-acceptor dipole-dipole interactions, which can be presented by Coulombic coupling V_{Coul} (charges coupling). Then the FRET rate (k_{FRET}) follows Fermi's golden rule:

$$k_{FRET} = \frac{2\pi}{\hbar}|V|^2\rho \tag{2.1}$$

where $\hbar$ is the reduced Planck constant, V is the electronic coupling between donor and acceptor, and ρ is the density of the interacting initial and final energetic states, which is related to the spectral overlap integral J (the overlap of donor emission and acceptor absorption, defined in the wavelength or wavenumber scale). In **Equation 2.1**, V can be replaced by the R^{-3} distance dependent V_{Coul} (**Equation 2.2**):

$$V_{\text{Coul}} = \frac{\kappa|\vec{\mu}_{\text{D}}||\vec{\mu}_{\text{A}}|}{4\pi\varepsilon_0 n^2 R^3} \tag{2.2}$$

where $\vec{\mu}_{\text{D}}$ and $\vec{\mu}_{\text{A}}$ are the transition dipole moments of donor and acceptor, κ is the orientation factor between them, ε_0 is the vacuum permittivity, n is the refractive index, and R is the donor-acceptor distance.

By substituting **Equation 2.2** into **Equation 2.1**, the FRET rate can be described as the following **Equation 2.3**:

$$k_{\text{FRET}} = \frac{9(\ln 10)\kappa^2\Phi_{\text{D}}}{128\pi^5 N_{\text{A}} n^4 \tau_{\text{D}} R^6} J \tag{2.3}$$

where Φ_{D} is the luminescence quantum yield of D in the absence of energy transfer, N_{A} is Avogadro's number (6.023×10^{23} mol^{-1}), and τ_{D} is the luminescence lifetime of the donor.

The basic principle of FRET is illustrated in **Figure 2.1 (left)** through the Jablonski diagram. Following *hv* excitation, the ground-state donor (D) is raised to its excited state (D*), subsequently transitioning to the excited electronic ground state via inner relaxation, which involves vibrational and rotational relaxation. Finally, it returns to its ground state (D) through radiative decay (k^{R}), nonradiative decay (k^{NR}), or FRET (k^{FRET}). FRET can only occur when the donor and acceptor share the same electronic transition (red, green, and purple horizontal lines in the left figure), signifying that the difference between their respective energy levels is equal. In this case, FRET takes place from an excited donor (D*) to a ground-state acceptor. In spectroscopic terms, a successful FRET pair requires spectral overlap between the donor emission and the acceptor absorption (as shown in **Figure 2.1, right**).

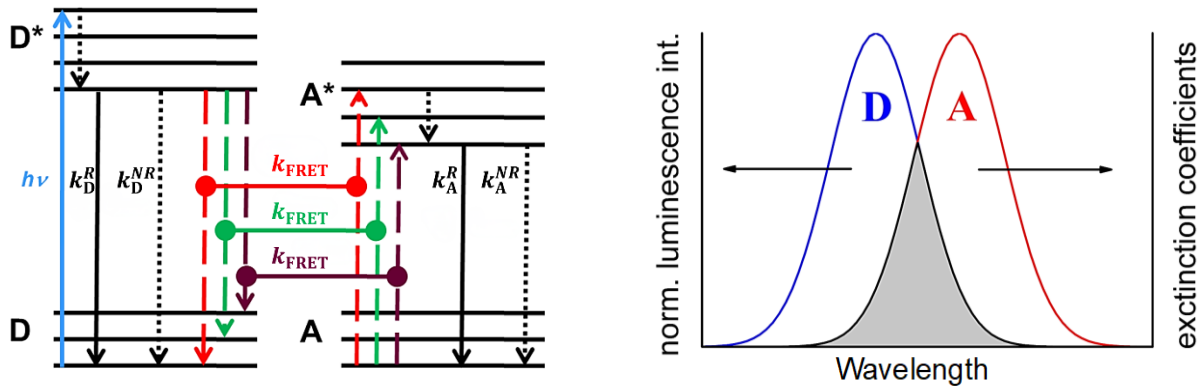

Figure 2.1. (Left) The basic FRET principle is illustrated by the Jablonski diagram (a simplified energy level scheme). Under excitation (hv), the ground state donor (D) transitions to an excited state (D*), followed by a return to the excited electronic ground state via inner relaxation (vibrational and rotational, indicated by the black dotted arrow). Finally, it returns to its original ground state (D) through radiative

decay (k^{R}), nonradiative decay (k^{NR}), or FRET (k^{FRET}). For FRET to occur, the donor and acceptor should share the same electronic transitions (red/green/purple horizontal lines), indicating that their respective energy levels are equal. Following FRET, the acceptor enters an excited state (A*), and subsequently returns to its ground state (A) through radiative or nonradiative decay processes. **(Right)** The spectral overlap (in gray area) between the normalized D emission and A molar absorption (ε_A) defines the overlap integral J (cf. **Equation 2.5**). (Adapted with permission from reference [2]. Copyright 2013 Wiley-VCH Verlag GmbH & Co. KGaA)

For a specific FRET pair, when the FRET rate (k_{FRET}) is in equilibrium with other decay rates of the donor ($k_{FRET} = k_D^R + k_D^{NR} = \tau_D^{-1}$), and the FRET efficiency is 50%, the distance between the donor and acceptor is defined as the Förster distance (R_0). R_0 can be calculated by the following **Equation 2.4** by replacing k_{FRET} in **Equation 2.3** with τ_D^{-1} and R with R_0.

$$R_0 = \left(\frac{9(\ln 10)\kappa^2\Phi_D}{128\pi^5 N_A n^4} J\right)^{1/6} \tag{2.4}$$

The spectral overlap integral J as shown in **Figure 2.1 (right)**, defined in wavelength scale can be calculated by **Equation 2.5**:

$$J = \int \bar{I}_D(\lambda)\varepsilon_A(\lambda)\lambda^4 \, d\lambda \tag{2.5}$$

where $\varepsilon_A(\lambda)$ presents the acceptor molar absorption spectrum, while $\bar{I}_D(\lambda)$ presents the emission spectrum of donor normalized to unity as shown in **Equation 2.6**.

$$\int \bar{I}_D(\lambda) \, d\lambda = 1 \tag{2.6}$$

The last important variable in FRET theory is the orientation factor κ^2, which can be calculated based on the angles between transition dipole moments of donor ($\vec{\mu}_D$), acceptor ($\vec{\mu}_A$), and their connection vector $\vec{R}$ (as shown in **Figure 2.2**) by **Equation 2.7**:

$$\kappa^2 = [\hat{\mu}_D \cdot \hat{\mu}_A - 3(\hat{\mu}_D \cdot \hat{R})(\hat{\mu}_A \cdot \hat{R})]^2 = [cos\theta_{DA} - 3cos\theta_D cos\theta_A]^2 \tag{2.7}$$

where $\hat{\mu}_D$, $\hat{\mu}_A$ and $\hat{R}$ present the unit vectors of $\vec{\mu}_D$, $\vec{\mu}_A$, and $\vec{R}$, respectively. As shown in **Figure 2.2 (left)**, θ_{DA} presents the angle between $\vec{\mu}_D$ and $\vec{\mu}_A$, while θ_D and θ_A present the angles between $\vec{\mu}_D$ with $\vec{R}$, and $\vec{\mu}_A$ with $\vec{R}$, respectively.

From the calculation by **Equation 2.7**, the value of κ^2 is in a range of 0 to 4, resulting from the relative orientation of donor and acceptor transition dipole moments ($\vec{\mu}_D$ and $\vec{\mu}_A$). The examples are as shown in **Figure 2.2 (Right)**, when $\vec{\mu}_D$ and $\vec{\mu}_A$ are collinear, κ^2 is 4, while when they are parallel to each other, κ^2 is 0. If they are perpendicularly oriented, κ^2 will be 0.

Generally, κ^2 can be assumed as 2/3, which is the average value from a situation where both the donor and acceptor are free to rotate to any possible orientation during the FRET time ($1/k_{FRET}$). This means that the system is in a dynamic averaging regime during FRET, and the average rotation rate is much higher than the average FRET rate ($k_{rot} \gg k_{FRET}$). 2/3 is a descent assumption for most of the practical cases. Even for a system where only one participant of the FRET (donor or acceptor) shows average orientation (the other participant has a fixed orientation), the value of κ^2 is between 1/3 and 4/3, for which 2/3 is still an acceptable approximation. Since the sixth root of κ^2 is taken as shown in **Equation 2.4**, variation of κ^2 should not cause major errors in the calculation of FRET distance. Therefore, in many biological experiments, the orientation factor in FRET can be assumed as 2/3, which significantly simplifies the application of FRET.

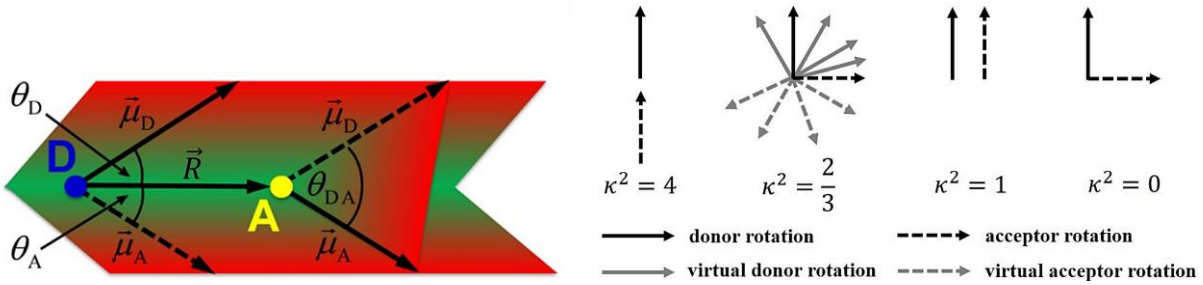

Figure 2.2. (Left) The orientation of transition dipole moments of donor emission ($\vec{\mu}_D$), acceptor absorption ($\vec{\mu}_A$), and the connection vector $\vec{R}$ between them. (Adapted with permission from reference [5]. Copyright 2016 American Chemical Society.). **(Right)** The possible virtual orientations of donor and acceptor transition dipole moments and the corresponding κ^2 values. (Adapted with permission from reference [26]. Copyright 2015 MDPI.)

For the FRET rate, as shown in **Equation 2.8**, the relationship between k_{FRET}, the luminescence decay time of the donor, and the donor-acceptor distance can be derived by combining **Equations 2.3** and **2.4**.

$$k_{FRET} = \tau_D^{-1} \left[\frac{R_0}{R}\right]^6 \tag{2.8}$$

The FRET efficiency (E_{FRET}) can be expressed using **Equation 2.9**, illustrating its dependence on R^{-6} (the sixth power of the distance). As depicted in **Figure 2.3**, E_{FRET} exhibits pronounced sensitivity to the distance (R) between the donor and acceptor, particularly when it falls within the range of 0.5 to 2.0 times R_0 (gray area).

$$E_{FRET} = \frac{k_{FRET}}{k_{FRET}+k_D^R+k_D^{NR}} = \frac{k_{FRET}}{k_{FRET}+\tau_D^{-1}} = \frac{1}{1+(R/R_0)^6} = \frac{R_0^6}{R_0^6+R^6} \tag{2.9}$$

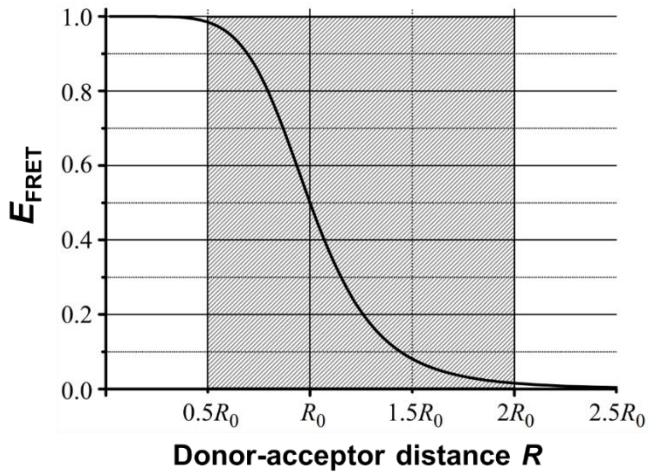

Figure 2.3. FRET efficiency (E_{FRET}) as a function of donor–acceptor distance (R). When R is in the range of 0.5 to 2.0 R_0, there is a strong sensitivity of E_{FRET} to R (gray background area). (Adapted with permission from reference [23]. Copyright 2013 Wiley-VCH Verlag GmbH & Co. KGaA.)

Since FRET is a deactivation process of the excited donor fluorophore, it can result in the photophysical property changes of the donor. By combining with spectroscopy, FRET efficiency can also be determined by the measurements of the luminescent intensity (I), decay time (τ), or quantum yield (Φ) of the donor in the presence (I_{DA}, τ_{DA}, Φ_{DA}) and absence of the acceptor (I_D, τ_D, Φ_D), respectively (as shown in **Equation 2.10**). The spectroscopy analysis of FRET also paved the way for their biosensing applications, which are typically based on the quantification of analytes by calculating the FRET ratio (the luminescent intensity ratio between donor (I_D) and acceptor (I_A)) according to **Equation 2.11**. This ratiometric approach is very advantageous for biosensing as it can suppress the medium interferences and excitation energy fluctuation.

$$E_{FRET} = 1 - \frac{I_{DA}}{I_D} = 1 - \frac{\tau_{DA}}{\tau_D} = 1 - \frac{\Phi_{DA}}{\Phi_D} \quad (2.10)$$

$$FRET\ ratio = \frac{I_A}{I_D} \quad (2.11)$$

For better readability, certain equations and abbreviations are repeated in the different chapters.

2.2 FRET applications

Due to the intrinsic distance dependence at the nanometer scale and the high sensitivity for distance changes, FRET has become an ideal tool for the study of biomacromolecular structure elucidation, intra/inter-molecular interactions, and diagnostics [27]–[29]. Over the last 30 years, FRET under the spatial and temporal resolution has been implemented into the analysis of almost all the interesting biological targets, including nucleic acids, proteins, metabolites, drugs, toxins, pathogens, and cells, etc. [30]. The mechanisms of FRET-based assays mostly depend on the bioconjugations of fluorophores on recognition molecules for targets and the measurable FRET signals generated from the interactions between recognition molecules and targets, such as molecular cleavage, binding, or structural rearrangement [31], [32]. The following **Sections 2.2.1** and **2.2.2** will focus on the progress in the applications of FRET in immunoassays and nucleic acid biosensing, which also provide the important background knowledge for the original works in this thesis.

2.2.1 FRET-based immunoassay

Immunoassays are important bioanalytical methods based on the binding reactions between antibodies and corresponding analytes (antigens). Due to the inherent specificity, high sensitivity, and strong affinity of antibodies when binding to analytes, immunoassay has become one of the most widespread and key tools for fundamental life-science research [33]. In general, immunoassay can be performed in heterogeneous or homogenous conditions. Heterogeneous immunoassays, such as enzyme-linked immunosorbent assay (ELISA), are widely used analytical methods for sensitive detection of analytes, but they require multiple incubation and washing steps to remove free antigens and antibodies for a reduced background signal (as shown in **Figure 2.4A**) [34]. In contrast, homogenous immunoassay (**Figure 2.4B**) allows a single-step and mix-to-measure procedure, which is favorable for on-site sensing and can be performed with simple and widely accessible devices and reader platforms [35].

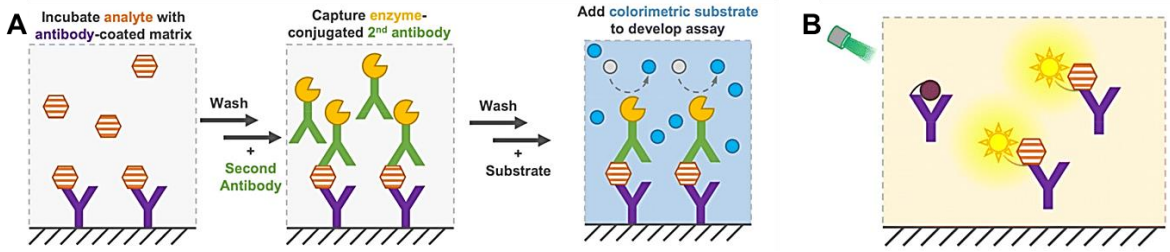

Figure 2.4. Schematic representation of heterogeneous and homogeneous immunoassays. **(A)** Heterogenous immunoassay (ELISA) with multiple incubation and washing steps. **(B)** Example of a homogeneous immunoassay. (Orange hexagon: antigen; green and purple "Y" shapes: two different antibodies that bind to different episodes of an antigen; white and blue circles: the colorimetric substrate and product, respectively; brown-red circles and sun shapes: the quenched and luminescent fluorophores. (Adapted with permission from reference [35]. Copyright 2023 The Royal Society of Chemistry)

In terms of designed formations, both heterogeneous and homogeneous immunoassays can be performed as either non-competitive (sandwich format) or competitive immunosensors. In a non-competitive immunoassay, two different antibodies can bind to different epitopes of one antigen to form a sandwich complex. As the example in **Figure 2.5A** shows, in this sandwich immunoassay, the signal from the fluorophores labeled on the second antibody increases with the analyte concentration increasing. In the competitive immunoassay, (example in **Figure 2.5B**), where only one kind of antibody is used, with the addition of testing sample, the analytes added can compete with the fluorophore-labeled analytes to bind with the limited number of antibodies, leading the decreased signal from the fluorophores on labeled analytes.

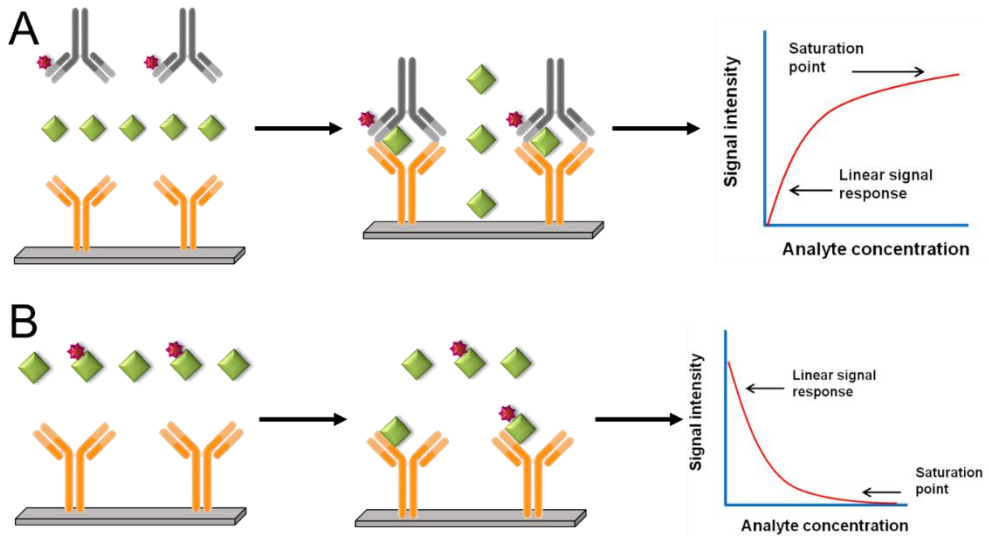

Figure 2.5. Schemes of different immunoassays. **(A)** Example of non-competitive immunoassay (sandwich format). **(B)** Example of competitive immunoassay. (orange "Y" shape: immobilized capture

antibody; gray "Y" shape with red star: labeled detection antibody; green diamond: antigen; green diamond with red star: fluorophore-labeled antigen.).

Compared with the conventional colorimetric and absorbance-based analyses such as ELISA, which quantifies analytes by a color indicator from the enzymatic reaction in a complex mixture [18, 19], fluorescent immunoassays show many advantages, such as fast response, high sensitivity, and multiplexing ability based on spectral resolution. Hence, fluorescent immunoassays have become popular and powerful tools in various applications, from biosensing, and diagnostics to all the fundamental life science.

Due to the distance sensitivity in the biological interaction range (1-20 nm), FRET which involves various fluorophores, becomes an ideal tool for developing luminescent immunoassays to detect the antibody-antigen binding [36]. In general, FRET-based immunoassay can quantify the targets of interest by calculating the FRET ratio which is designed to change when the antibody binds to an antigen. As ratiometric approaches, FRET-based immunoassays are usually free from background signal and favorable for homogenous applications. In 1976, Ullman et al. presented the first homogeneous FRET immunosensors, which were designed into non-competitive and competitive formats, respectively (**Figure 2.6**) [37]. The proposed immunosensors aimed to quantify small molecules by competitive immunoassay (**Figure 2.6A**), as well as to detect large analytes that bind with both FRET donor acceptor-labeled antibodies to improve FRET (**Figure 2.6B**). Following the development of these promising immunosensors, further studies have been widely conducted to address their limitations and improve their detection sensitivity, efficiency, and anti-interference abilities.

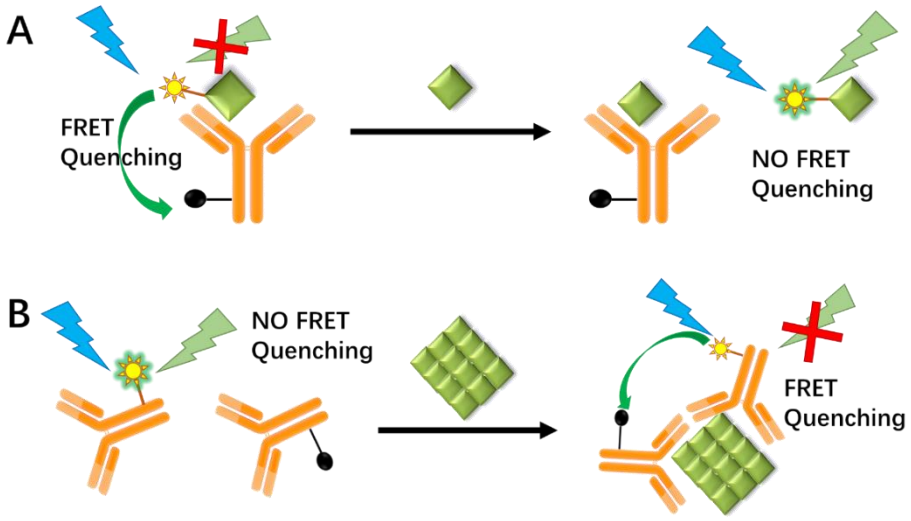

Figure 2.6. Schemes presentation of homogeneous FRET immunosensors. **(A)** Competitive immunoassay. **(B)** Non-competitive immunoassay.

According to the FRET theory, a large donor-acceptor distance can decrease the FRET efficiency. Namely, the relatively large dimensions of antibodies and some antigens will reduce the detection sensitivity or limit the manipulation of FRET-based immunoassays [38]. To overcome this drawback, there are two possible approaches: **(i)** Engineered small antibodies (single chain fragments of antibody or nanobodies) are promising alternatives to conventional antibodies, which have been successfully used for sandwich immunoassays [39]. **(ii)** New luminescent materials with improved photophysical properties such as high-quantum-yield quantum dots (QDs) have been reported to improve FRET efficiency in immunoassays by extending the Förster distance [40]. Lanthanide complex to QDs FRET pairs have been also used to develop sensitive homogenous immunoassays for prostate-specific antigens [41] and alpha-fetoprotein [42]. Thanks to the broad absorption spectra of QDs, there are big overlaps between lanthanide complex donor emission and QDs acceptor absorption, which can extend the Förster distance of these FRET pairs, leading to improved FRET.

For biological systems, the auto-fluorescence background and the leakage of excitation light are non-negligible limitations for luminescent homogenous immunoassay. To overcome this drawback, time-resolved (TR) FRET-based on new materials with long luminescent decay times has been employed. TR-FRET measurements enable the suppression of the auto-fluorescence (short-lifetime fluorescence from sample impurities, serum, and cell lysate), the fluctuation from the excitation source, and the directly excited acceptor emission not mediated by FRET [43]. Therefore, TR-FRET shows increased sensitivity, reliability, and anti-interference ability by being minimally affected by false-positive or negative results. For example, in 2013, Geißler et al. reported a robust multiplexed six-color TR-FRET immunosensor for simultaneous sensing of tumor markers [44]. Qiu et al. also presented a TR-FRET immunosensor based on terbium-complex and QDs FRET pairs for multiplexing detection of EGFR (epidermal growth factor receptor) and HER2 (human epidermal growth factor receptor-2) [18]. Near-infrared (NIR) emitting materials (emitting after 700 nm) such as lanthanides and upconversion nanoparticles (UCNPs) are also interesting labels for FRET-

based immunoassays, because their emissions are well separated from biological auto-fluorescence mostly at the wavelength range of 350-550 nm [45].

2.2.2 FRET for nucleic acid detection

Nucleic acids, including DNA and RNA, are considered important biomarkers and analytes for early-stage diagnosis of diseases, genotyping, and pharmacogenomics [46]–[48]. However, their small quantity and instability in body fluids, bring big challenges for precise detections, especially in biological matrices such as serum with high noise and non-target interfering substances [49], [50]. Therefore, studies aiming for precise and reliable detections of nucleic acids have been conducted to overcome these drawbacks. Among them, fluorescent signal-based, nanometer-scale distance-sensitive FRET assays are promising methods for homogenous, real-time, and high-throughput sensing of nucleic acids. In this context, a substantial array of FRET-based biosensors for nucleic acids has been successfully developed.

In general, the design of FRET-based nucleic acid sensing strategies is mostly dependent on the hybridization reaction. The classic design typically consists of a pair of oligonucleotide probes that bind to adjacent DNA targets [51]. As the example in **Figure 2.7 (Top)** shows, one oligo probe is labeled with a fluorescent donor at its 5'-end, and the other oligo probe is labeled with an acceptor at its 3'-end. The two labeled oligo probes can bind to the same target DNA at adjacent parts, bringing the donor and acceptor into proximity which allows FRET to occur. This proposed assay can quantify the target DNA by measuring the FRET ratio without extra washing procedures. Another example is as shown in **Figure 2.7 (Bottom)**, one oligo probe is labeled with acceptor fluorophore at its 5'-end, while a double-strand DNA (dsDNA) intercalating dye is used as FRET donor. In this format, with the presence of target DNA, a hybridization reaction between target DNA and oligo probes will enable the FRET from inserting dyes to acceptor fluorophores, leading to an increasing FRET ratio. As homogenous bioassays, both proposed sensors enable the real-time monitoring of the target DNA directly in solution or even in live cells. Based on this, various configurations of FRET sensors for DNA sequence sensing have been developed [52].

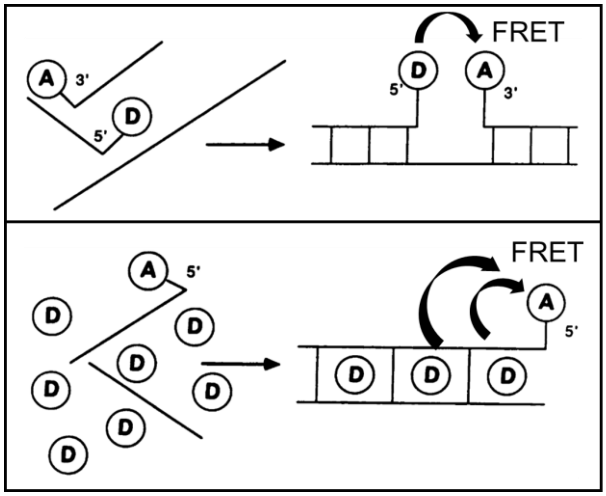

Figure 2.7. Designs of FRET-based biosensors for nucleic acids detection. **(Top)** Two oligo probes are labeled by FRET donor (D) and acceptor (A) fluorophores, respectively. The two labeled probes can hybridize with adjacent fragments of the target DNA, which improves the FRET from donor to acceptor fluorophores. **(Bottom)** A dsDNA intercalating dye is used as the FRET donor, while another fluorophore attached to the oligo probe is used as the FRET acceptor. The hybridization between the target DNA and the oligo probe brings the donor close to acceptor, which results in increased FRET ratio. (Adapted with permission from reference [52]. Copyright 1988 National Academy of Science.)

Molecular beacon is one of the most well-established nucleic acid probes based on DNA hybridization and FRET principles. It was first described by Tyagi and Kramer in 1996 [53], after that, it has been widely used to recognize and report specific nucleic acids targets. Typically, a molecular beacon has a hairpin structure, of which the loop fragment can hybridize to the target nucleic acid sequence, and the two ends of the double-stranded stem are attached with a FRET donor and an acceptor, respectively (**Figure 2.8**). FRET occurs from the donor fluorophore to the acceptor in a closed format of the molecular beacon, resulting in the quenching of the donor. When the target sequences are present, the hybridization of the loop fragment and target sequence will open the hairpin structure and lead to the recovery emission of the donor, which enables the sensitive and specific detection of the nucleic acids target. Molecular beacon probes offer several advantages, including high sensitivity, selectivity, a simple format, easy design, and low cost[54]. These qualities make them powerful tools for the analysis of single or multiple sequences, proving beneficial in applications such as DNA/RNA biomarker quantification, genotyping studies [59], single nucleotide polymorphism detection[55], and allelic discrimination analysis [56].

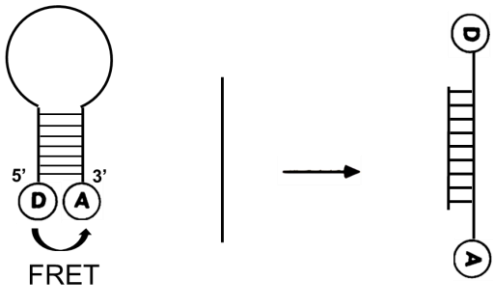

Figure 2.8. Scheme of nucleic acids detection by molecular beacon probe. The molecular beacon contains a double-strand stem which is labeled with a donor (D) and an acceptor (A) at the 5'-end and 3'-end, respectively. The specific target DNA can hybrid with the loop part and open the hairpin shape, reducing the FRET signal.

2.3 Lanthanides

2.3.1 Introduction

Lanthanides (or lanthanoids) comprise 15 metallic elements with atomic numbers from 57 to 71: lanthanum, cerium, praseodymium, neodymium, promethium, samarium, europium, gadolinium, terbium, dysprosium, holmium, erbium, thulium, ytterbium, and lutetium. Lanthanides, along with scandium and yttrium, are often collectively referred to as rare earth elements or rare earth metals [57]. These elements exhibit very similar chemical properties, often coexisting in minerals, which makes it difficult to separate them from each other [58]. Additionally, their distribution in the Earth's crust is quite scattered, further complicating their purification and extraction, which explains why they are called "rare earth" elements.

The general electronic configuration of lanthanides is $[Xe]4f^n5d^{0-1}6s^2$ (n = 0−14), where the 4f orbitals are gradually filled by electrons from La (0) to Lu (14). Therefore, lanthanides are also referred to as f-elements. The characteristic oxidation state of lanthanide elements in the solid state, aqueous solutions is a trivalent state (Ln^{3+}) with the electron configuration of $[Xe]4f^n$, where they have relatively low ionization energies for the loss of either two 6s electrons and one 5d electron or two 6s electrons and one 4f electron [59]. In addition to the common trivalent oxidation state, some lanthanide elements also exhibit other oxidation states such as Ce^{+4} or Eu^{+2}, for which the f orbitals are empty or half-occupied, respectively [60]. The 4f-orbitals are important factors that distinguish lanthanides from other transition elements and provide outstanding properties to lanthanides.

The f-f electronic transition involving redistribution of electrons within 4f orbitals results in a rich variety of energy levels of Ln^{3+} and vests them specific luminescent properties [61]. Along with the spatial shield from $5s^2$ and $5p^6$ orbitals, 4f orbitals are minimally affected by the external environment, which enables well-defined energy levels as well as distinct, sharp, and narrow emission bands for lanthanides [59]. As shown in **Figure 2.9 A**, the Ln^{3+} ions on the periphery (Ce^{3+}, Pr^{3+}, Nd^{3+}, Pm^{3+}, Ho^{3+}, Er^{3+}, Tm^{3+}, and Yb^{3+}) have relatively small energy gaps between adjacent levels, while the central ions (Sm^{3+}, Eu^{3+}, Gd^{3+}, Tb^{3+}, Dy^{3+}) possess larger band gaps. Therefore, the emission of lanthanides can cover the entire spectrum range, including UV (Gd^{3+}), Vis (e.g., Pr^{3+}, Sm^{3+}, Eu^{3+}, Tb^{3+}), and NIR (e.g., Pr^{3+}, Nd^{3+}, Er^{3+}, Yb^{3+}). Particularly, Tb^{3+} and Eu^{3+} exhibit relatively large energy gap ($^5D_4$-^7F_J for Tb^{3+}, $^5D_0$-^7F_J for Eu^{3+}), and well-distinct emission bands in green and red regions (**Figure 2.9 B**), which makes them favorable luminescent probes in many applications [62], [63].

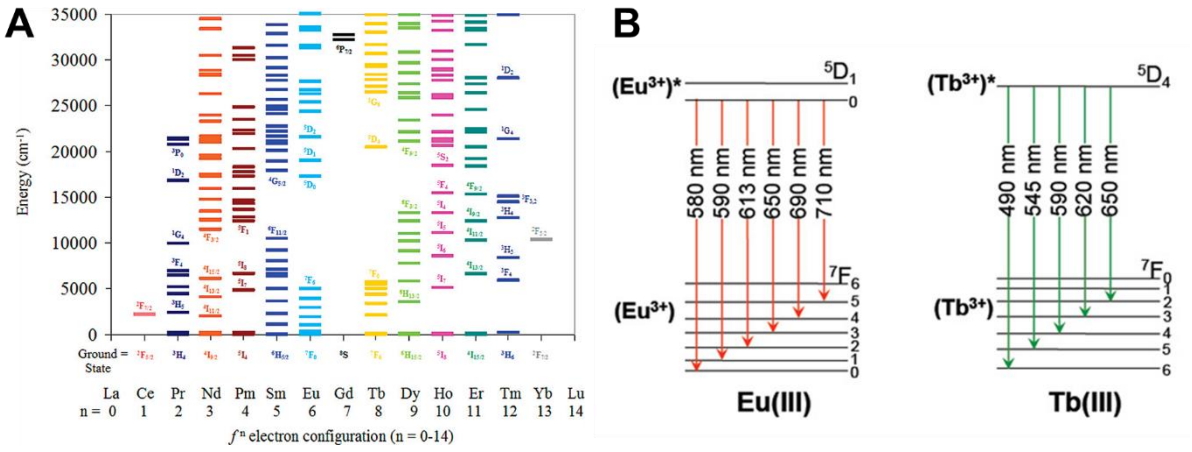

Figure 2.9. (A) Partial energy level diagram for Ln^{3+} ions. (Reprinted with permission from reference [59]. Copyright 2009 American Chemical Society.) **(B)** Commonly observed emission wavelengths from 4f-4f electronic transitions of Tb^{3+} and Eu^{3+}, respectively. (Reprinted with permission from reference [62]. Copyright 2014 American Chemical Society.)

2.3.2 Luminescent lanthanide complexes

As mentioned above, the intrinsic luminescence of lanthanides originates from 4f-4f electronic transitions, which offer unique spectroscopic properties to lanthanides [64]. As a consequence of the Laporte selection rule and parity rule (or the change in spin multiplicity), the f-f transitions of Ln^{3+} have quite low probabilities, resulting in very long photoluminescence

(PL) lifetimes and quite low molar absorptivity ($\varepsilon < 1\ M^{-1}\ cm^{-1}$), which can be around 10^4-10^5 times lower than their organic dye counterparts [65]. Therefore, lanthanides face limitations of weak luminescence from direct excitation and depend on strong light sources such as high-power lasers. To circumvent this drawback, the "antenna effect" has been applied, where the lanthanide ions are indirectly excited through the energy transfer from a sensitizing antenna. As presented in **Figure 2.10 A**, strong absorbing organic chromophore or chromophore-appended ligands are coordinated with Ln^{3+} to form luminescent lanthanide complexes (LLCs), then the chromophores can excite centered Ln^{3+} by intramolecular energy transfer [66]. In addition, this coordination chelate can protect central Ln^{3+} from environmental PL quenching, such as the vibrational energy dissipation by oscillators (e.g., O-H bonds of water molecules). For an antenna effect model, the energy migration pathways can be explained by the Jablonski diagram in **Figure 2.10 B**: the strong absorbing antenna ligand is excited to its singlet excitation state and goes to its lowest triplet state through intersystem crossing, which then excites the coordinated Ln^{3+} through intramolecular energy transfer [62].

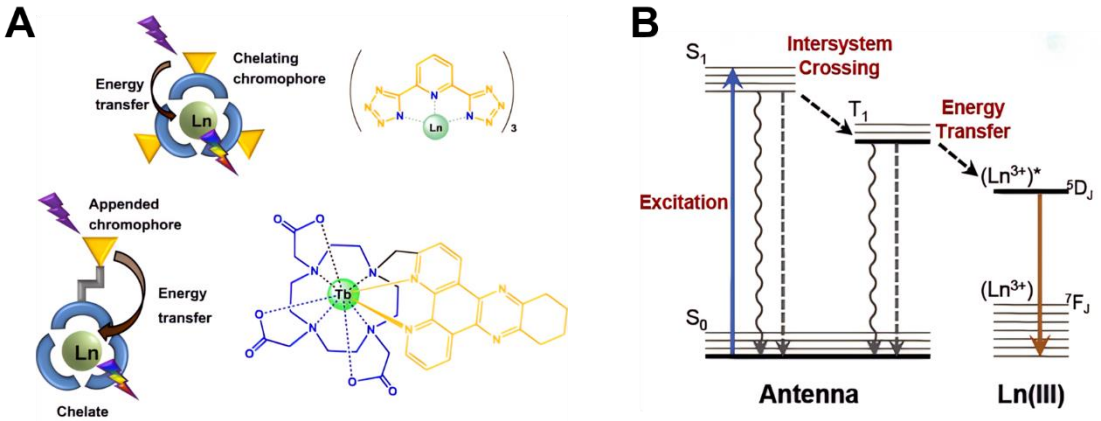

Figure 2.10. (A) Two designs of LLCs based on the antenna effect. (Reprinted with permission from reference [66]. 2015 Elsevier B.V.) **(B)** Simplified Jablonski diagram for the energy migration pathways of antenna effect in LLCs. (Reprinted with permission from reference [62]. Copyright 2014 American Chemical Society.)

The overall quantum yield of a lanthanide complex can be calculated by the following **Equation 2.12**:

$$\Phi_{LLC}^{overall} = \frac{photons\ emitted\ by\ Ln}{photons\ absorbed\ by\ attenna\ ligand} = E_{ET} \times \Phi_{LLC}^{Ln} \qquad (2.12)$$

where $\Phi_{LLC}^{overall}$ presents the overall quantum yield of LLC from the indirect excitation of Ln^{3+} by the antenna ligand, Φ_{LLC}^{Ln} is the intrinsic quantum yield from direct excitation of the Ln^{3+}, and E_{ET} is the intramolecular energy transfer efficiency from ligand to Ln^{3+} ion.

Thanks to the efficient antenna effect, LLCs exhibit unique advantages as luminescent probes compared with other fluorophores [67]: **(i)** The overall quantum yield of LLC can be improved by selecting the antenna ligands with high absorptivity and E_{ET}, or increasing the Φ_{LLC}^{Ln} by using Ln^{3+} carrier chelate to protect Ln^{3+} from the aqueous matrix quenching. **(ii)** The indirect excitation of Ln^{3+} results in very large effective Stokes shifts of LLCs (take luminescent Tb complex as an example, **Figure 2.11 A**), which allows a facile block of excitation light during the LLC PL measurement. **(iii)** The PL lifetimes of LLCs can be increased up to milliseconds by the coordination of Ln^{3+} with chelate/cryptate ligands. It allows delayed or time-gated PL measurement by using pulsed excitation, which can suppress the short-lived autofluorescence background from the biological matrix and other fluorophores (**Figure 2.11 B**). These outstanding properties make LLCs important materials in biological applications, including biosensing, diagnostics, imaging, and photodynamic therapies [68], [69].

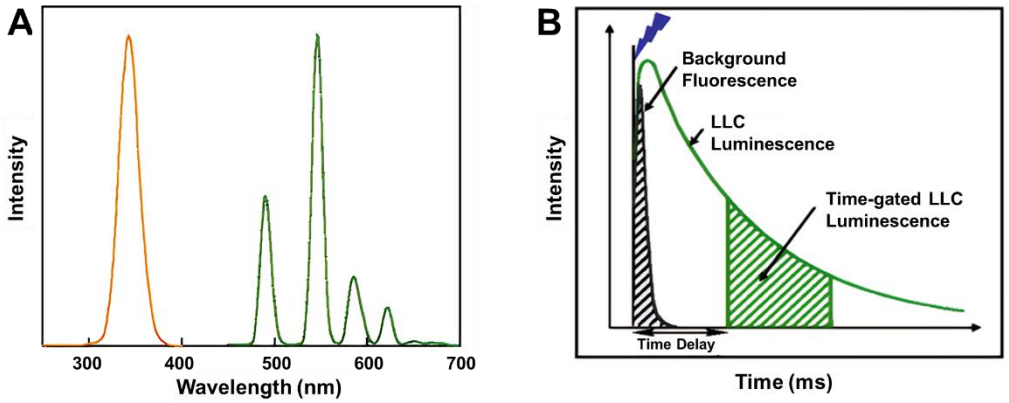

Figure 2.11. Spectroscopic properties of LLCs. **(A)** Representative effective Stokes shift of LLCs: The orange spectrum presents the absorption of an antenna; the green spectrum presents the emission of Ln^{3+}. **(B)** Principle of time-gated spectroscopy. (Adapted with permission from reference [70]. Copyright 1995 Elsevier B.V.)

2.3.3 Luminescent lanthanide complexes as FRET donors

As described in **Section 2.1**, FRET is a powerful tool for biological analysis, and it can provide more advantages and new opportunities by using unique LLCs as FRET donors. Thanks

to the remarkable PL properties of LLCs, LLC-based FRET can be enhanced in several ways, encompassing increased FRET efficiency, extended responsive distance, less uncertainty of orientation factors, as well as the potential for spectral or temporal multiplexing.

The increased quantum yield of Ln^{3+} in LLCs (Φ_{LLC}^{Ln}) is a key factor in improving FRET efficiency and Förster distance. It is important to notice that the quantum yield of donor is presented by Φ_{LLC}^{Ln} instead of overall quantum yield $\Phi_{LLC}^{overall}$, because Φ_{LLC}^{Ln} determines the donor's electric field [16]. Additionally, the multiple emission bands of LLCs provide a higher possibility for them to overlap with various acceptors' absorptions. For instance, luminescent Tb complex (LTC) exhibits several emission bands at the wavelength range of 450-700 nm, which overlaps with many excellent absorbers such as fluorophores and quantum dots. The large spectral overlap integrals allow Förster distances of 4-6 nm for LTC-to-dye FRET and up to 11 nm for LTC-to-QD FRET [16], making them suitable for a broader range of applications in sensing biological interactions.

Another advantage of LLC donors (e.g., Tb and Eu complexes) is that they can exhibit unpolarized emission, which provides reduced uncertainty to the orientation factor κ^2 for the FRET calculation. More important, their extremely long excited state lifetimes usually allow for random dynamic orientation between the donor and acceptor transition dipole moments and a dynamic averaging assumption (κ^2 = 2/3) can be applied [16]. Even when the acceptor fluorophore is completely rigid, κ^2 can still be limited to a value between 1/3 and 4/3 (as discussed in **Section 2.1.1**), for which the error in R_0 resulted from the assumed 2/3 is not too large (less than 12% due to the sixth root dependence). Thus, the distance determination by LLCs-based FRET is more accurate than that for classical FRET pairs, for which the orientation factor is often poorly known [23].

The multiplexing capability of LLCs-based FRET comes from two remarkable properties of LLCs:

(i) The narrow and well-distinct emission bands of LLCs make it possible to achieve spectral multiplexing, where the simultaneous identification and quantification of multiple targets are realized by PL measurements of acceptor emission of different colors. As the FRET donor, the various well-separated emission bands of LLCs can overlap with the absorptions of different acceptors, (e.g., organic dyes and QDs) (**Figure 2.12 top**), and allow the signal

collection of acceptors with low LLC background through bandpass transmission filters (**Figure 2.12 bottom**). However, compared with QDs, which exhibit narrow and well-located emissions, organic dyes usually have very broad emission bands, and their PL measurements often suffer from spectral crosstalk. Therefore, for a LLCs-to-multi dyes FRET system, a deconvolution of contribution from individual acceptors is a practical solution to achieve efficient multiplexing.

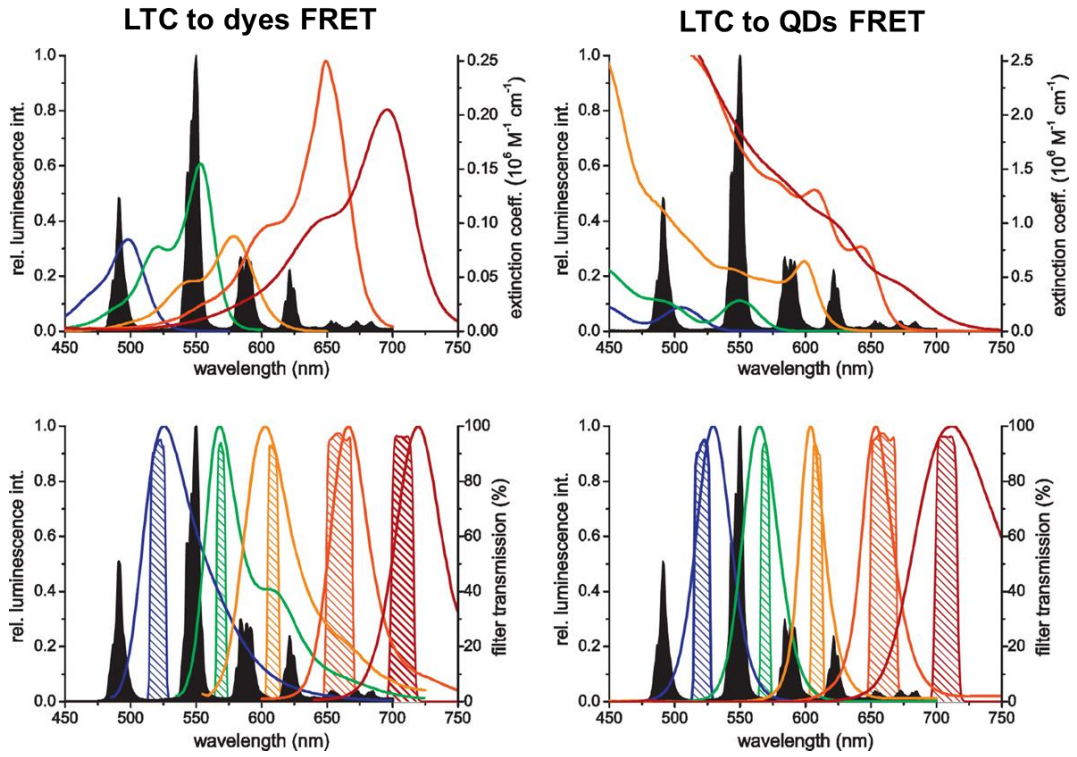

Figure 2.12. FRET pairs based on LTC donors and multiple acceptors. **(Top)** Spectral overlap between LTC emission and different acceptors absorption. **(Bottom)** Well-separated emission bands of LTC allow the measurements of different acceptors with very low LTC backgrounds (represented by the shaded bandpass filter transmission spectra). LTC PL spectra are filled with black. The left figures present LTC-to-dyes FRET: Oregon Green (blue), AlexaFluor555 (green), AlexaFluor568 (orange), Cy5 (red), and AlexaFluor700 (wine). The right figures present LTC-to-QDs FRET: QD525 (blue), QD565 (green), QD605 (orange), QD655 (red), and QD705 (wine). (Adapted with permission from reference [16]. Copyright 2014 Elsevier B.V.)

(ii) The long PL decay times of LLCs are advantages to time-resolved measurements and temporal multiplexing. As mentioned above, LLCs can show PL decay times up to milliseconds (ms), which is 10^4-10^5 times longer than the lifetimes of common organic dyes or QDs (nanoseconds scale). The large difference of donor and acceptor PL decay times ($\tau_D \gg \tau_A$)

results in approximately equal PL decay times ($\tau_{DA} = \tau_{AD}$) of FRET-quenched donor and FRET-sensitized acceptor (the decay time of direct excited acceptor is negligible). In this way, even for a single FRET pair, various FRET-induced decay times (τ_{DA} or τ_{AD}) can be achieved by tuning the FRET efficiency (typically by tuning the donor-acceptor distance), which provides the possibility of temporal multiplexing by collecting signals from distinct PL decay curves. Moreover, by introducing temporal multiplexing design to spectrally distinct FRET pairs, combined spectral and temporal multiplexing can be realized for a third multiplexing dimension [16]. Our group has reported a proof of concept for the simultaneous homogeneous detection of four different DNAs by combined spectral and temporal multiplexing method (**Figure 2.13**) [71].

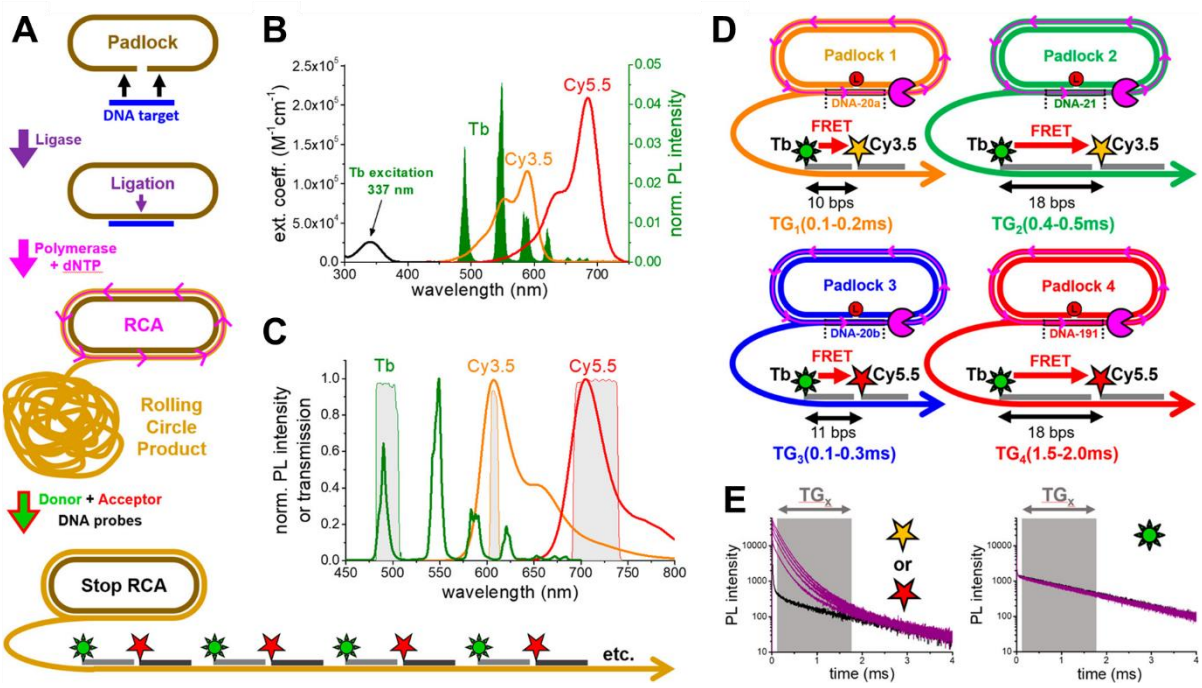

Figure 2.13. Quadruplexing of DNAs based on target-induced nucleic acid rolling circle amplification (RCA) and Tb-to-dyes FRET. **(A)** The scheme of target-induced RCA and FRET. **(B)** Spectra of Tb absorption (black) and emission (green) that partly overlap with the absorption of Cy3.5 (orange) and Cy5.5 (red). **(C)** Emission spectra of Tb (green), Cy3.5 (orange), and Cy5.5 (red). Optical bandpass filter transmission spectra, which represent the detection channels for Tb, Cy3.5, and Cy5.5, are shown in gray. **(D)** The combination of spectral (Tb-to-Cy3.5 and Tb-to-Cy5.5) and temporal multiplexing (distance tuning between Tb and dyes). **(E)** Time-gated PL measurements of FRET-sensitized acceptor and FRET-quenched Tb. (Reprinted with permission from reference [71]. Copyright 2018 American Chemical Society.)

2.4 Quantum Dots

2.4.1 Introduction

Quantum dots (QDs) are luminescent semiconductor nanoparticles with sizes smaller or close to their exciton Bohr radius (typically ranging from 1 to 10 nm), which are mainly single-core or core-shell structures composed of elements from group II-VI (e.g. CdS, CdSe, CdTe, ZnS, etc.), group III-V (e.g. GaAs, GaN, InAs, etc.), or their alloys (e.g. CdSeS, InGaN, InGaAs, etc.) [72]. The discovery of quantum dots can be traced back to the 1980s when the quantum confinement effect in semiconductor nanocrystals was observed, and studies proved that the electronic structure and optical properties of QDs can be decisively affected by their size and composition [73]–[76]. Since then, QDs garnered substantial interest in many research domains, but most studies have focused on QDs synthesis technologies [72], [77] and QDs-based photovoltaic equipment [78]. Until the late 1990s, after water-soluble and biocompatible QDs were prepared, QDs were first introduced as fluorescent probes for life science applications [79], [80]. From that on, QDs have been widely used as bright, photostable fluorescent probes for cellular and molecular imaging, offering advantages over traditional organic dyes. The 2023 Nobel Prize in Chemistry was awarded for the discovery and development of QDs. The following sections will introduce the photophysical properties (**Section 2.4.2**), and surface functionalization (**Section 2.4.3**) of QDs and examine how QDs serve as FRET donors or acceptors (**Section 2.4.4**).

2.4.2 Photophysical properties

Due to the quantum confinement effect in semiconductors, QDs exhibit unique photophysical properties, which can be explained by their electronic properties in the intermediate regime between bulk semiconductors and molecules [81]. Firstly, bulk semiconductor materials' electronic structures are composed of a lower energy valence band (VB) occupied by electrons and a higher energy conduction band (CB), which is unoccupied. Upon excitation, an electron can be promoted into the quasi-continuum CB and leave a positively charged hole in the quasi-continuum VB, then the interaction between the electron and the hole creates an exciton, and the distance between the electron-hole pair is defined as the exciton Bohr radius. However, in terms of QDs with sizes smaller or close to the exciton

Bohr radius (a few nm), they contain a limited number of atoms (for QDs with 2-10 nm diameters, there are as few as 100-100,000 atoms per QD) as well as a low electronic states density, which is not sufficient to form complete band structures, and thus the quantization of energy levels can be observed at the band edges. With the QD's size decreasing, energy levels become more separated, and the inter-bandgap energy increases (**Figure 2.14 A**), resulting in a hypsochromic shift of QD PL emission. Therefore, the PL wavelength of QDs can be tuned by controlling their size [72] (**Figure 2.14 B**).

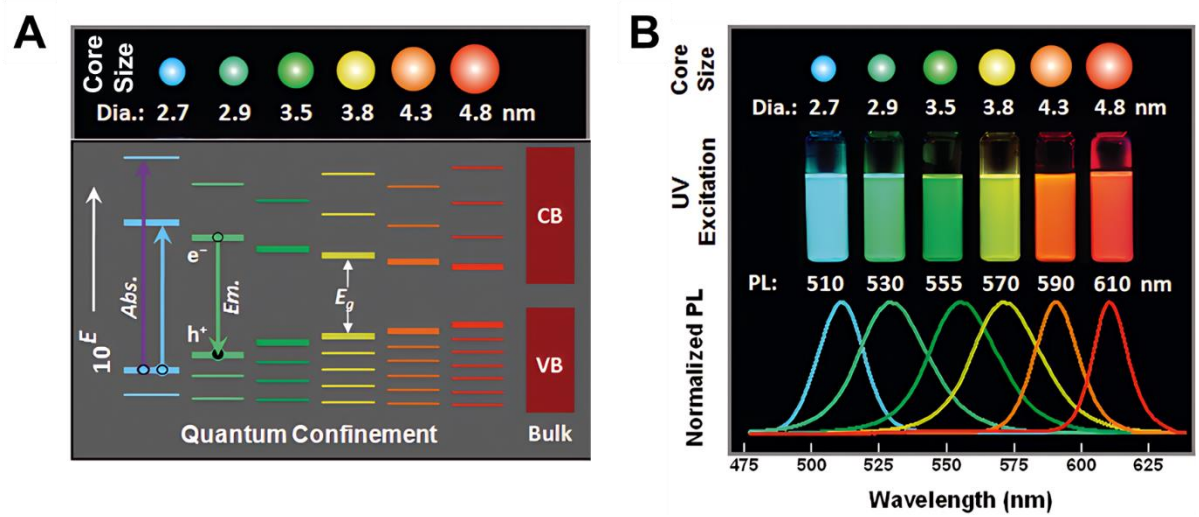

Figure 2.14. (A) Cartoon, discrete energy levels of CdSe/ZnS QDs with increasing size. White arrow and 10^E present the energy scale. E_g presents band gap energies. CB and VB present the conduction and valence bands of bulk CdSe. **(B)** Cartoon, photograph, and size-dependent emission spectra of CdSe/ZnS QDs with increasing size. (Adapted with permission from reference [81]. Copyright 2011 American Chemical Society.)

The tunable PL wavelength range of QDs is decisively affected by the semiconductor material, which can be tuned from the UV to the NIR region [81]. Typically, CdSe and CdTe QDs are most popular in biological applications due to their preferable tunable emissions spanning the visible region of the spectrum [2]. What's more, the size distribution of QDs can affect the shape of their PL emission spectra. In principle, a narrow and symmetric emission spectrum can be obtained from high-quality, monodisperse QDs, which usually yield an emission profile with a full-width at half-maximum (FWHM) of 25-35 nm [82].

In contrast to their narrow PL spectra, QDs have very broad, featureless absorption spectra, which means they can absorb at a wide range of wavelengths. This broad absorption allows

QDs to absorb photons over a broad range of energies, among which the excess energy above the energy gap can be efficiently transferred to the electron and hole via nonradiative intra-band transitions, leading to identical band-edge PL emission regardless of the initial excitation wavelength. Thus, QDs have high extinction coefficients (ca. 10-50 times higher than organic dyes) [83] and large Stokes shift from the effective separation between excitation and emission wavelengths.

Another advantage of QDs is their high quantum yield and photostability, which have been significantly enhanced through core-shell structure designs. Encapsulating the core QD with a shell material effectively passivates or 'caps' surface defects. With fewer surface defects available, excitons are less likely to be trapped or quenched by surface states, which results in more efficient radiative recombination and emission [84]. On the other hand, the shell materials acts as protective barriers, shielding the core QDs from the external environment to prevent oxidation and degradation, thus enhancing their photostability [85].

In conclusion, QDs possess outstanding photophysical properties that make them ideal biosensing probes [25], including: **(i)** narrow, size-dependent, and symmetric PL spectra spanning from UV to NIR regions (favorable to spectral-multiplexed sensing and imaging), **(ii)** broad absorption profiles (excitation flexibility), **(iii)** large Stokes shifts (allowing an efficient block of excitation light), **(iv)** high brightness due to both high extinction coefficients (10^5–10^6 M^{-1} cm^{-1} at first absorption band, increasing toward UV region) and quantum yields (sufficient for single particle visualization and tracking), **(v)** high photostability (strong resistance to photobleaching and chemical degradation), **(vi)** relatively large nano surface for flexible functionalization and bioconjugation. **(vii)** High multiphoton action cross sections of some QDs allowing excitation with NIR light (favorable for deeper tissue penetration and reducing light adsorption and scattering of biological matrix) [86].

2.4.3 Surface functionalization and bioconjugation

Thanks to the advantageous photophysical properties of QDs, they have become important luminescent materials for biological applications, which also greatly promotes the need for QDs with good water-solubility and biocompatibility. Since most high-quality QDs are synthesized with hydrophobic surface ligands, as-prepared QDs possess poor water-solubility. To render

QDs soluble in aqueous solutions, several strategies have been developed, mainly including cap ligand exchange, encapsulation, and silica coating (**Figure 2.15**).

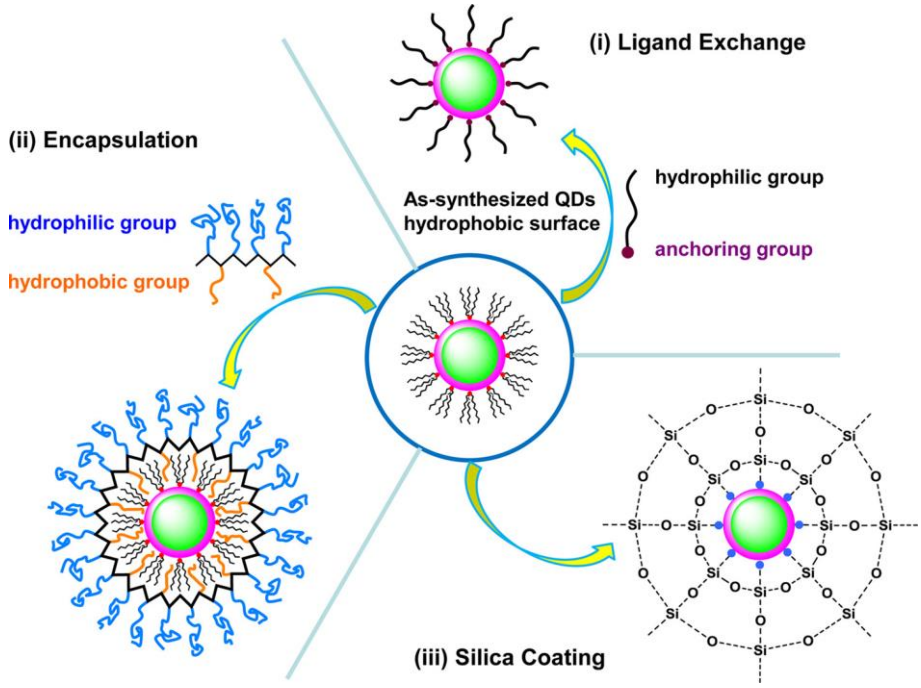

Figure 2.15. Schematic overview of different strategies for QDs surface functionalization. **(i)** ligand exchange, **(ii)** encapsulation, and **(iii)** silica coating chemistries. The center represents an as-synthesized QD in an organic solvent with its hydrophobic surface of organic ligands. (Reprinted with permission from reference [5]. Copyright 2017 American Chemical Society.)

Ligand exchange is the strategy to replace the native hydrophobic ligands on the QD surface with bi-functional ligands which contain a surface anchoring group to bind to the inorganic QD surface and a hydrophilic group to achieve water solubility. Thiol-based molecules (e.g. mercaptoacetic acid [87]–[89], mercaptopropionic acid [90], [91], mercaptoundecanoic acid [92], [93], and dihydrolipoic acid (DHLA) [94] are most widely used ligands due to the strong affinity between thiol with QD surface metal atoms (Cd and Zn). However, since the colloidal stability of QDs is determined by the deprotonation of the carboxyl groups, the usable pH range of QDs is limited. Then, the strategies to solve this problem by modifying the thiol ligands with poly (ethylene glycol) (PEG) were presented [95], [96]. It has been reported that PEG-appended DHLA derivatives enable the colloidal stability of QDs at a pH range from weakly acidic to strongly basic aqueous solutions [97]–[99]. On the other hand, minimizing the hydrodynamic size of QDs is crucial for their cellular uptake and distance-sensitive FRET-based applications. Therefore, zwitterionic ligands are explored as alternatives

to larger PEG ligands. Susumu et al. reported a series of DHLA-based zwitterionic ligands, which can attach to QDs surface with high affinity and allow rapid and efficient cellular uptake [100]. These zwitterionic ligand-coated QDs have compact sizes, satisfying colloidal stability across a wide pH range even in high-salt concentrations, low toxicity in cells, and the capability for direct conjugation with His-tagged biomolecules or other reactive groups for biomolecule attachment.

Encapsulation is a process in which amphiphilic ligands, such as phospholipids and amphiphilic polymers, are applied to coat the QDs. This is achieved through hydrophobic interactions, with the hydrophobic portions of the ligands aligning toward the QD surface. This arrangement leaves the hydrophilic segments exposed around the QD periphery, ensuring colloidal stability [101]. Since the encapsulation method does not modify the original ligands on QDs, and protects the QDs surface from environmental interaction, QDs can preserve their intrinsic quantum yield. However, the large hydrodynamic diameters generated from thick coating often limit their application in FRET-based systems.

Silica coating is a strategy to cover the QD surface with a siloxane network. The coating process usually starts with QDs surface ligand exchange with (3-mercaptopropyl) trimethoxysilane to form nucleation sites, then followed by shell growing with silane molecules such as tetraethoxysilane via hydrolysis and condensation, [102], [103] or a water-in-oil reverse microemulsion method [104]–[106]. The robust cross-linked silica network can efficiently improve the photochemical stability and colloidal stability of QDs against pH change. In addition, the silica shell is non-toxicity and can be further biofunctionalized. However, compared to the ligand exchange method, the relatively complicated preparation procedure and large hydrodynamic diameter from the thick silica layer still limit their application, especially in FRET-based studies [5]. However, this deficiency is expected to be remedied by the introduction of lanthanide complexes as FRET donors, which usually provide large Förster distances for FRET pairs [15].

With water-soluble and biocompatible QDs in hand, the next important issue is the bioconjugation of biomolecules onto QDs, which is a fundamental technique in many QD-based biological applications, including recognition of biomarkers, targeting of cells and tissues, delivery of drugs, and in vivo diagnostics [107]. Various biomolecules have been successfully

immobilized onto QDs surface by covalent or non-covalent approaches, such as nucleic acids, antibodies, proteins, and peptides, etc. (**Table 2.1**) [107], [108]. The most common covalent conjugation strategies are using bifunctional groups, e.g., EDC (1-ethyl-3(3-dimethylaminopropyl) carbodiimide hydrochloride) [109], DCC (dicyclohexylcarbodiimide) [110], NHS (N-hydroxy-succinimide) [111], and SMCC (succinimidyl 4-N-maleimidomethyl cyclohexane-1-carboxylate) [112], to catalyze a reaction between carboxylic acid and amino group, generating a stable amide linkage. Non-covalent bioconjugations are mainly based on hydrophobic interactions, electrostatic interaction, direct attachment, and high-affinity secondary interactions. For instance, poly-histidine labeled biomolecules can be immobilized onto QDs surface due to the high affinity of poly-histidine for metal ions of QDs [113]. Another important non-covalent conjugation strategy is based on the biotin-streptavidin interaction, which leverages the high affinity of streptavidin for biotins [114], [115]. These high-affinity non-covalent interactions provide a simple, versatile, and robust method for bioconjugation of QDs, offering high specificity, stability, and the potential for multiplexed assays in various biotechnology and life science research domains.

Table 2.1. Strategies for QDs bioconjugations

quantum dot	biomolecules	coupling strategy	catalyst	coupling structures
	SH	ligand exchange	free	
COOH	NH_2	carbodiimide chemistry	EDC/DDC, NHS, etc.	
SH		sulfhydryl-reactive chemistry	free	
NH_2	SH	bifunctional cross-linker	SMCC	
	SH	sulfhydryl-reactive chemistry	free	
		reaction of phenylboronic and diols	free	
	NH_2	hydrazone reaction	aniline	
		electrostatic interactions	free	
		ligand-receptor interactions	free	
		click chemistry	free	
N_3		click chemistry	free	
	N_3	click chemistry	free	
		metal-affinity coordination	free	
		metal-affinity coordination	Ni^{2+}	
		encapsulation and bio-binding	free	
		encapsulation	free	

QD; surface ligand; biomolecule (e.g., proteins, peptides, nucleic acids, and viruses); viral capsid; ligand (e.g., biotin and antibody); acceptor (e.g., streptavidin and antigen); surface metal ion (e.g., Zn^{2+}); water-soluble shell (e.g., silica, liposome, and polymer)

* (Adapted with permission from reference [116]. Copyright 2015 American Chemical Society.)

2.4.4 QDs as FRET donors/acceptors

QDs are valuable luminescent materials for participating in FRET due to their unique photophysical properties and nanoparticle characteristics. In general, QDs can serve as ideal FRET donors, but with the development of new luminescent materials, detection techniques, and instrumentation, their applications as FRET acceptors have also opened new chapters. This section will discuss their capacity as FRET donors and FRET acceptors, respectively.

QDs as FRET donors

Compared with organic dyes, QDs show extraordinary advantages as FRET donors (**Figure 2.16**). **(i)** QDs possess broad absorption spectra at the UV/blue region, enabling efficient excitation at selectable wavelengths, where the direct excitation of the acceptor can be avoided, leading to enhanced FRET sensitivity. **(ii)** The high extinction coefficient (> 10^6 M^{-1} cm^{-1}) and high brightness of QDs make them strong nanoantenna to transfer energy to acceptors. **(iii)** The continuous size-tunable emission spectra of QDs allow the overlap with the absorption of different acceptors, which makes QDs suitable donors for many acceptors and ideal components for multiple FRET pairs. **(iv)** The narrow and symmetric emission spectra of QDs can reduce spectral overlap with acceptor emission, enhancing the precision and accuracy of FRET measurements. **(v)** QDs typically exhibit longer PL lifetimes (tens to hundreds of ns) compared to organic dyes (few ns), which can be advantageous in time-resolved FRET experiments, aiding in the discrimination of FRET signals from background fluorescence from biological matrix and the directly excited acceptors. **(vi)** The large surface of QDs allows multiple attachment of acceptors, which can improve the FRET efficiency ($E_{\mathrm{FRET}} = \frac{nR_0^6}{nR_0^6+R^6}$), and create new opportunities for biosensing designs.

QDs as FRET acceptors

Some of the above-mentioned advantages of QDs as FRET donors, including broad absorption spectra, narrow emission spectra, and high extinction coefficient, etc., are also beneficial for FRET using QDs as acceptors. However, it is more challenging to find proper donors for QDs. Firstly, it has been proven that organic dye-to-QD FRET is very unfavorable, which can be explained by the difference between their PL lifetimes [117]. Due to the broad

and strong absorption of QD, upon excitation, both QD "acceptor" and dye "donor" will go to excited states. Since the PL lifetime of QD is ten times higher than that of a typical organic dye, the dye will go back to its ground state before QD, which makes the dye impossible or very unfavorable to serve as an energy donor to QD [9]. To overcome these drawbacks, longer-lifetime donor and pulsed excitation are requested, which allows the excited donor to transfer energy to ground state QD after a proper delay following the pulsed excitation. The first trial was reported in 2005, where a long-lifetime (hundreds of ns) Ru complex was found to be quenched by a QD acceptor, but the sensitization of QD was not observed [117]. In the same year, a Tb chelate with an even longer lifetime (ms) was successfully used as a FRET donor to excite a QD acceptor [118]. Since then, many studies focusing on lanthanide complex-to-QD FRET have been conducted, which pave the way to new possibilities.

The combination of luminescent lanthanides complex (LLC) donor with QD acceptor offers several intriguing advantages to the field of FRET due to their unique PL properties as described in **Section 2.3 and 2.4.2**: **(i)** A large Förster distances (6-11 nm) between LLC donor and QD acceptor is provided by the large spectral overlap between donor emission (especially Tb complexes, LTC) and QDs absorption, high quantum yield of LTCs, and high extinction coefficient of QDs. **(ii)** The long excited lifetime of LTC enables the time-gated detection, which can cut off the fluorescent background from the biological system and directly excited QDs. **(iii)** The narrow, symmetric, and size-dependent emission bands of QDs enable the spectral multiplexing based on the same LTC donor to differently emitting QDs acceptors FRET.

Notes

However, it should be noted that there are also certain challenges when quantum dots are employed in FRET applications. **(i)** QDs emit from their core instead of the surface, which means the large size, thick coating, or long conjugation linkers with their donors/acceptors can decrease the FRET efficiency unfavorably. **(ii)** Some QDs are in non-spherical shapes, which leads to different donor-acceptor distances even in the same type of conjugation. **(iii)** The photophysical properties of QDs can be significantly affected by the environment, such as water, biomolecules, pH, and temperature, which can quench the QDs, as well as decrease their colloidal stability, leading to aggregation and precipitation.

CHAPTER 3

FRET-based immunoassay for the detection of EGFR

3. FRET-based immunoassay for the detection of EGFR

3.1 Introduction

Ultrasensitive bioassays are essential for the quantification of different biomarkers in clinical diagnostics. Assays based on Förster resonance energy transfer (FRET) are of particular interest because they are highly sensitive and very easy to perform as they do not require any separation or washing steps [27], [34]. However, FRET is only functional for donor-acceptor distances below circa 10 nm [2], which makes it a challenging endeavor for the development of immunochemical biosensors based on nanoparticles (NPs) [119].

Nanobodies (NBs, or variable domains of the heavy chain of heavy-chain-only antibodies - VHH) are genetically engineered small (~15 kDa with a cylindrical shape of ~2.5 nm diameter and ~4 nm height) antibodies that have found frequent application in molecular imaging, clinical diagnostics, and disease therapy [120]–[126]. Their much smaller size compared to intact IgG antibodies (~150 kDa) combined with a simple expression, high stability, high solubility, and many chemical functionalization strategies provide NBs with several advantages for biosensing and bioimaging [121], [124], [125]. To design functional nanobiosensors, NBs have been bioconjugated to various nanomaterials [121], [127], including gold NPs [128], graphene oxide [129], lanthanide NPs [130], gold-platinum core-shell NPs [131], quantum dots (QDs) [132], [133], and porphyrin-based metal organic framework NPs [134]. QDs are arguably the most applied nanomaterials for FRET biosensing [5], [6], [135], [136], and NBs have been used to develop QD-to-dye [137], QD-to-QD [138], fluorescent protein-to-QD [139], and lanthanide-to-QD [18], [140]–[144] FRET immunosensors.

Specific attachment and orientation of small antibodies on QDs for improved immunotargeting have been demonstrated with cysteine (Cys) tagged NBs [18], hexahistidine (His_6) and Cys tagged albumin-binding domain-derived affinity proteins (ADAPTs) [17], His_6 tagged artificial repeat proteins (αReps) [145], and split protein (SpyCatcher/SpyTag) tagged short-chain variable fragments (scFv) [146]. Beyond these proofs-of-concept, the translation of NB-QD conjugates into standard probes that can be adapted to a broad range of biosensing approaches requires experimental comparison of different straightforward NB-QD bioconjugation methods using the same type of NB and commercially available QDs. Such one-

to-one evaluation of bioassay performance can provide important knowledge of how NB-QD bioconjugates can be efficiently implemented into diverse applications. Another important challenge to demonstrate the benefits of NB-QD-based immunosensors for daily use in biological, biochemical, or chemical laboratories is to make use of that knowledge and exploit NB-tags and QDs for the development of novel, simple, and efficient biosensing formats.

With these two major goals in mind, we implemented three widely used bioconjugation tags, namely His_6, Cys, and biotin, into the C-termini of two different NBs (EgB4 and EgA1) against the epidermal growth factor receptor (EGFR) as representative protein biomarker. The functionalized NBs were then used to prepare NB-QD bioconjugates with commercially available and widely used QDs of two different colors (QDot 625 and QDot 705, Thermo Fisher) and with three common surface coatings, namely compact zwitterionic ligands (CL4) [100], amino-polyethylene-glycol (PEG), and streptavidin (sAv). To demonstrate the biosensing functionality of this versatile bioconjugation toolkit, we compared the various NB-QD bioconjugates in wash-free and rapid FRET immunoassays for the quantification of EGFR. We then developed a new biosensing concept, in which His_6-tagged NBs were displaced from the QD surface by non-competitive binding of NB to EGFR. This new assay format, which required only a single type of NB and no QD bioconjugation, was applied for the quantification of soluble EGFR (sEGFR, a prognostic and predictive biomarker for metastatic breast cancer) [147] and soluble EGFR variant III (sEGFRvIII, a prognostic biomarker for glioblastoma) [148]. The NB-displacement assay significantly decreases cost and labor (for antibody screening and production and bioconjugation), strongly facilitates assay-kit assembly and storage (only one type of Tb-NB conjugate and one type of unlabeled QD), provides rapid (mix-and-measure) analysis, and can quantify relevant biomarkers at clinically relevant concentrations.

3.2 Materials and methods

3.2.1 Materials

Recombinant human EGFR Fc chimera (#344-ER-050) and HER2 Fc chimera (#1129-ER-050) dimers (MW: ~190 kDa for EGFR dimer and ~195 kDa for HER2 dimer) were purchased from R&D system. Human EGFRvIII, Fc Tag (EGI-H5255, ACRObiosystems) was

purchased at Fisher Scientific. 705nm emitting Qdots ITK Streptavidin (for size estimation: sAv has a size of 5.4 nm x 5.8 nm x 4.8 nm in the solid state) [149] Conjugate Kit (sAvQD705-core-shell ellipsoid size of around 6 nm × 12 nm minimum/maximum axes, as measured with TEM by the manufacturer; hydrodynamic diameter including sAv of ~18.5 nm as measured by size exclusion chromatography on HPLC by the manufacturer and size determined via retention time relative to a standard curve of proteins; circa 6 to 10 sAv per QD as given by the provider and estimated in biotin binding experiments), 705nm emitting ITK Qdots with amino-PEG (QD705-core-shell ellipsoid size of around 6 nm × 12 nm minimum/maximum axes, as measured with TEM by the manufacturer; hydrodynamic diameter including amino-PEG of ~20.5 nm as measured by size exclusion chromatography on HPLC by the manufacturer and size determined via retention time relative to a standard curve of proteins) and 625nm emitting organic Qdots (QD625, core-shell diameter of ~9.2 nm) [150] were purchased from Thermo Fisher. Lumi4-Tb complexes functionalized with NHS were provided by Lumiphore Inc.

Trizma hydrochloride (TRIS HCl), phosphate buffered saline (1×PBS), hydrochloric acid (HCl), sodium hydroxide (NaOH), tris(2-carboxyethyl)phospine hydrochloride (TCEP), N,N-dimethylformamide (DMF), sodium tetraborate decahydrate ($Na_2B_4O_7 \cdot 10H_2O$), sodium bicarbonate ($NaHCO_3$), bovine serum albumin (BSA), fetal bovine serum (FBS), and sulfo-EMCS crosslinker ((N-ε-maleimidocaproyl-oxysulfosuccinimide ester)) were purchased from Sigma-Aldrich. Sodium chloride (NaCl) was purchased from Duchefa. All chemicals were used as received. High-quality Milli-Q water with a resistivity of 18.2 MΩ cm was used for preparing solutions.

Selection of NBs was previously described and included EgB4 (NB2), a NB binding to both domain **I** and **II** of sEGFR [151], [152], and EgA1 (NB1), a NB binding to both domain **II** and **III** [151], [153]. Conjugation of the NBs to the different tags did not affect their affinity for EGFR, as measured by binding to A431 cells.

3.2.2 QD-NB conjugation

Conjugation of EgB4-Cys (NB2-C) to amino-PEG coated QD705 was performed using sulfo-EMCS crosslinkers. To receive maleimide-reactive QD705, a >50,000-fold molar excess of sulfo-EMCS was mixed with QD705 for 1h at 30 rpm at room temperature. Maleimide-

activated QDs were purified using a 100 kDa MWCO spin column from Millipore (Billerica, MA, USA) by washing three times with 1×PBS buffer (pH 7.4) to remove excess crosslinker. Disulfide bonds of EgB4 were reduced to sulfhydryls with 5 mM TCEP by mixing for 30 min with 30 rpm at room temperature without further purification. For final conjugation, both solutions (43 µL of 130.9 µM EgB4 + 100 µL of 0.64 µM QD705) were mixed and incubated for 6 h at 30 rpm at room temperature in the dark. Unbound EgB4 were separated by 100 kDa MWCO spin column by washing four times with 100 mM sodium tetraborate buffer (pH 8.4). Purified conjugates were centrifuged at 4000g and supernatants were stored at 4°C. QD concentrations were determined by absorbance measurements using a molar extinction coefficient of 8.3×10^6 M^{-1} cm^{-1} (at 405 nm) for QD705 as provided by the manufacturer. EgB4 were quantified by absorbance measurement at 280 nm using an extinction coefficient of 35,540 M^{-1} cm^{-1}. The labeling ratio (~28 NB/QD) was determined by a linear combination of the respective absorbance values of QD705 and EgB4 within the EgB4-Cys-QD705 conjugates. Considering the more than 200-fold difference in extinction coefficients between QD705 and NB2 at 280 nm, quantification of the labeling ratio by absorption measurements is very inaccurate and can only provide a rough estimation. Therefore, the actual labeling ratio is somewhere between zero NB2 per QD and 90 NB per QD (which was the molar ratio in the labeling procedure).

QD625s were functionalized with CL4 compact ligands as described previously [100]. Conjugation of EgB4-His_6 (NB2-H) to QD625 was performed in a molar ratio of 20:1 (EgB4-His_6 per QD) and mixed for 30 min. For best reproducibility, the conjugates were freshly prepared before FRET immunoassays. However, we also performed functional assays with NB-QD conjugates that had been stored for several months with no significant differences (not shown). QD concentrations were determined by absorbance measurements using a molar extinction coefficient of 9.9×10^6 M^{-1} cm^{-1} (at 405 nm) for QD625 as provided by the manufacturer. EgB4 was quantified by absorbance measurement at 280 nm using an extinction coefficient of 37,520 M^{-1} cm^{-1}. Considering the very efficient self-assembly of His_6-tagged biomolecules to QDs, the molar ratio can be considered as the actual labeling ratio (~20 NB/QD).

Conjugation of EgB4-biotin (NB2-B) to sAv-QD705 was performed in a molar ratio of 20:1 (EgB4-biotin per QD) and mixed for 30 min. For best reproducibility, the conjugates were freshly prepared before FRET immunoassays. However, we also performed functional assays with NB-QD conjugates that had been stored for several months. EgB4 was quantified by absorbance measurement at 280 nm using an extinction coefficient of 38,060 M^{-1} cm^{-1}. Considering the very efficient biotin-sAv binding, the molar ratio can be considered as the actual labeling ratio (~20 NB/QD).

3.2.3 Tb-NB conjugation

8 mM Lumi4-Tb-NHS was dissolved in anhydrous DMF and mixed (reaction ratio of Tb/AB = 3) with EgA1 or EgA1-His_6 (NB1 or NB1-H) in 100 mM carbonate buffer (pH 9.0). The mixture was incubated for 2 h at 25 rpm at room temperature. For Tb-conjugate purification, the samples were washed four to six times with 100 mM TRIS-HCl (pH 7.4) using a 3 kDa MWCO Amicon spin column at 4000g. Tb concentration was determined by absorbance measurements at 340 nm using a molar absorptivity of 26,000 M^{-1} cm^{-1} as provided by the manufacturer. NBs were quantified by absorbance measurements at 280 nm using an extinction coefficient of 34,510 M^{-1} cm^{-1} (EgA1) and 38,880 M^{-1} cm^{-1} (EgA1-His_6). The conjugation ratios were determined by a linear combination of the respective absorbance values of Tb and NBs within the Tb-NB conjugate absorbance. For both Tb-EgA1 and Tb-EgA1-His_6, the labeling ratios were 1.4±0.7 Tb/NB.

3.2.4 Optical characterization of FRET pairs

Absorption spectra (Lambda 35 UV/Vis System, PerkinElmer) and emission spectra for Tb (FluoTime 300, PicoQuant) and QD (SAFAS) samples were recorded in TRIS-HCl (100 mM, pH 7.4) respectively.

3.2.5 FRET immunoassays against sEGFR

Time-gated PL intensity measurements were acquired on a KRYPTOR compact PLUS clinical fluorescence plate reader (Thermo Fisher Scientific) in a time window from 0.1 ms to 0.9 ms after pulsed excitation at 337.1 nm using an integrated nitrogen laser operating at 20 Hz, 100 pulses. The PL decay curves were acquired directly from the FRET immunoassay samples on a time-resolved fluorescence plate reader (Edinburgh Instruments) using 4000 detection bins

of 2 µs integration time and nitrogen laser (VSL 337 ND, SPECTRA Physics) excitation at 337.1 nm, 20 Hz. Optical bandpass filters (Delta and Semrock) for Tb donor and QD acceptor channel were 494±10 nm for Tb, 640±7 nm for QD625, and 716±20 nm for QD705.

Tb-EgA1 and EgB4-QD conjugates were each dissolved in 50 µL of 10 mM TRIS-HCl buffer (pH 7.4) containing 0.5% (*w/v*) BSA. For FRET sandwich immunoassay calibration curves against sEGFR, the overall measuring volume of 150 µL contained 100 µL of a constant assay solution (50 µL of 6 nM Tb-EgA1 and 50 µL of 1.5 nM or 3.0 nM EgB4-QD conjugate) and 50 µL of sEGFR sample solution (with different concentrations of EGFR in TRIS/BSA buffer). For NB displacement FRET immunoassay calibration curves against sEGFR and sEGFRvIII, the overall measuring volume of 150 µL contained 100 µL of a constant assay solution (50 µL of 6 nM or 3 nM Tb-EgA1 and 50 µL of 1.5 nM EgB4-QD625 or 1.5 nM or 0.15 nM unconjugated QD625) and 50 µL of sEGFR or sEGFRvIII sample solution (with different concentrations of sEGFR or sEGFRvIII in TRIS/BSA buffer or in TRIS/BSA buffer containing between 5 and 30% (*v/v*) FBS). Optical bandpass filters (Delta and Semrock) were 494±20 nm for Tb, 640±14 nm for QD625, and 716±40 nm for QD705. All FRET assays were measured in black 96-well microtiter plates with an optimal working volume of 150 µL. Each sample containing sEGFR was prepared three times and the samples without sEGFR were prepared 10 times. Each of the samples was measured independently, such that the data points consisted of three or ten independent measurements and standard deviations were used as errors. After sample preparation the microtiter plates were incubated for 180 min (for sandwich assays) or 120 min (for NB displacement assays) at 37° C before measurements on KRYPTOR compact PLUS and Edinburgh Instruments time-resolved fluorescence plate readers. NB displacement assays were also performed after different incubation times (15, 30, 45, 60, 120, and 180 min) and with sHER2 (soluble human epidermal growth factor receptor 2) instead of sEGFR.

3.3 Results and discussion

3.3.1 Antibody bioconjugations

For an easier understanding of the different materials and material combinations, we introduced specific abbreviations (**Table 3.1**). The two different NBs do not compete for binding to EGFR (**Figure 3.1**) and can thus be used to detect the soluble EGFR ectodomain in immunological sandwich assays. NB1 binds sEGFR and sEGFRvIII in the cleft formed between domains **II** and **III** [151], [153], whereas NB2 only binds to domains **I** and **II** of sEGFR [151], [152]. Conjugation to the different tags did not affect their affinity for EGFR, as measured by binding to A431 cells (**Figure 3.2 and Table 3.2**). The spectral properties of the Lumi4-Tb (Tb) FRET donor and QD acceptors used for the FRET immunoassays are shown in **Figure 3.3**. Tb FRET donor conjugates were prepared using amino-reactive chemistry between Lumi4-Tb-*n*-hydroxysuccinimide (NHS) and NB1 (Tb-NB1) or NB1-H (Tb-NB1-H) [18]. QD FRET acceptor conjugates were prepared depending on the different tags on NB2: *i) NB2-H-QD625-CL4:* QD625-CL4 were mixed in a 1:20 molar ratio with NB2-H, which resulted in efficient metal-affinity mediated self-assembly to the Zn-rich QD surface after ~30 min [154]. Considering the 2.5 nm diameter of NBs [124], 20 NB2 should take approximately 50 nm^2 of space on the ~265 nm^2 surface of the QD ($A = 4\pi r^2$ with $r = 4.6$ nm), which can be considered low enough to avoid steric hindrance and allow for efficient self-assembly. *ii) NB2-B-QD705-sAv:* NB2-B was attached to QD705-sAv via the strong biotin-sAv interaction [107], also by simple mixing for ~30 min in a 20:1 molar ratio. Considering the four biotin binding sites of sAv and the number of circa 6 to 10 sAv per QD, there should be sufficient binding sites for the 20 NB2-B per QD705-sAv. *iii) NB2-C-QD705-PEG:* Bioconjugation of QD705-PEG was more complex and was performed via N-ε-maleimidocaproyl-oxysulfosuccinimide ester (sulfo-EMCS) crosslinkers that were first attached to the QDs and then reacted with a ~90-fold molar excess of NB2-C for 6 h followed by separation of unbound compounds [17].

Table 3.1. Materials (and their short names) used for FRET assay development

FRET donor	**Short name**
Lumi4-Tb	Tb
FRET acceptors	**Short name**
QDot625-CL4	QD625-CL4
QDot705 streptavidin	QD705-sAv
QDot705 amino-PEG	QD705-PEG
Nanobodies	**Short name**
EgA1 (no tag)	NB1
EgA1-His_6	NB1-H
EgB4-Cysteine	NB2-C
EgB4-Biotin	NB2-B
EgB4-His_6	NB2-H

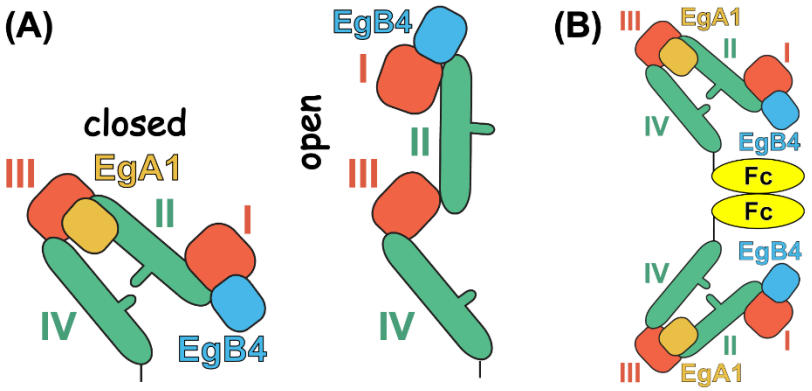

Figure 3.1. Schematic presentation of EGFR conformations and binding of EgA1 (NB1) and EgB4 (NB2). **(A)** The four ectodomains of EGFR with bound EgA1 and EgB4. In the open form (right), only EgB4 can bind. EgA1 binds in the cleft formed between domains **II** and **III** and keeps EGFR in that closed form (left) [153]. In the presence of both EgA1 and EgB4, the equilibrium between the two conformations is most probably shifted to the closed form. **(B)** Possible EGFR Fc-homodimer conformation when both EgA1 and EgB4 bind to EGFR. The two EgA1 and two EgB4 per Fc-homodimer, the different possible conformations, and the flexibility in the Fc fusion sites result in many possible donor-acceptor distances and thus, a donor-acceptor distance distribution.

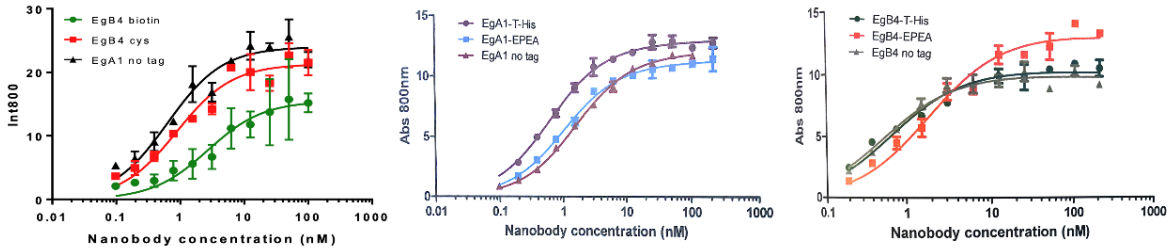

Figure 3.2. Results of NB binding assays (absorbance at 800 nm over NB concentration measured with IRDye 800CW EGF binding assay using A431 cells). Compared with the EgA1 (NB1) and EgB4 (NB2) without tags, NBs labeled with biotin, cysteine, histidine, and EPEA amino acids tags show similar affinity for EGFR. Detailed results are shown in **Table 3.2**.

Table 3.2. Results from the different binding assays are shown in **Figure 3.2**.

	EgB4 biotin	EgB4 Cys	EgB4-T-His	EgB4-EPEA	EgB4 no tag	EgA1-T-His	EgA1-EPEA	EgA1 no tag	EgA1 no tag
B_{max}	15.5	21.3	10.2	13.1	9.9	12.4	10.8	11.5	24
k_D	2.7 nM	0.9 nM	0.7 nM	1.9 nM	0.6 nM	0.6 nM	1.0 nM	1.5 nM	0.6 nM

*B_{max} presents the total density of available binding targets (A431 cells), and K_D presents the NB concentration that binds to a half amount of the cells.

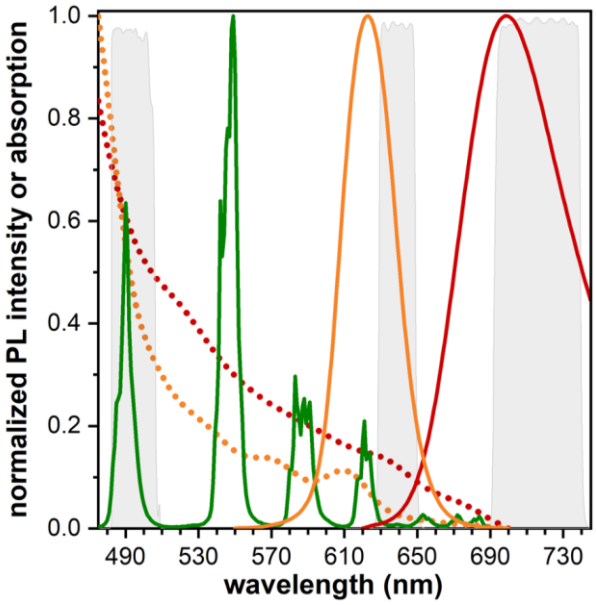

Figure 3.3. PL emission spectra of Tb (green), QD625 (orange), and QD705 (red) and spectral bandwidths of the filters (gray areas in the background) that were used for Tb and QD detection in the immunoassays. QD absorption spectra (dotted lines) showed good spectral overlap with the Tb PL (Förster distances: R_0(Tb-QD625) = 9.7±0.5 nm; R_0(Tb-QD705) = 10.4±0.5 nm). Excitation at 337 nm was close to the maximum absorption (~339 nm) of Tb (not shown).

Bioconjugation strategies *(i)* and *(ii)* have significant advantages. Preparation is rapid and simple and does not require separation because both metal-affinity mediated self-assembly and biotin-sAv binding are very efficient (quantitative labeling). Thus, the molar ratio of NB and QD can be considered as the labeling ratio (20 NB per QD). Moreover, NB-QD conjugates can be prepared directly before the immunoassays, which avoids storage problems and guarantees reproducible NB-QD bioconjugates for each assay. The longer and more complex bioconjugation procedure *(iii)* prevents preparation directly before the biosensing experiments. The actual labeling ratio is also more difficult to estimate because absorption measurements at 280 nm (more than 200-fold higher absorption of QDs compared to NBs) are inaccurate. However, more important than the actual number of NBs is the accessibility of the NBs on the QDs, which we directly evaluated by binding saturation in the FRET assays (vide infra).

3.3.2 sEGFR detection based on sandwich immunoassays

The analytical performance of the different NB-QD bioconjugates was compared in time-gated (TG) FRET sandwich assays for sEGFR quantification (**Figure 3.4A**) using the clinical diagnostic TG-FRET plate reader *KRYPTOR compact PLUS* (Thermo Fisher Scientific). Both Tb-donor and QD-acceptor PL intensities (in a time gate from 0.1 to 0.9 ms after pulsed excitation at 337 nm) were measured and the QD/Tb intensity ratios (*FRET-ratio*) were used to record sEGFR concentration-dependent immunoassay calibration curves. Increasing concentrations of sEGFR resulted in the formation of increasing amounts of Tb-NB1-EGFR-NB2-QD FRET sandwich complexes and a concomitant increase of the *FRET-ratio*, which leveled off into saturation at higher sEGFR concentrations (**Figure 3.4B**).

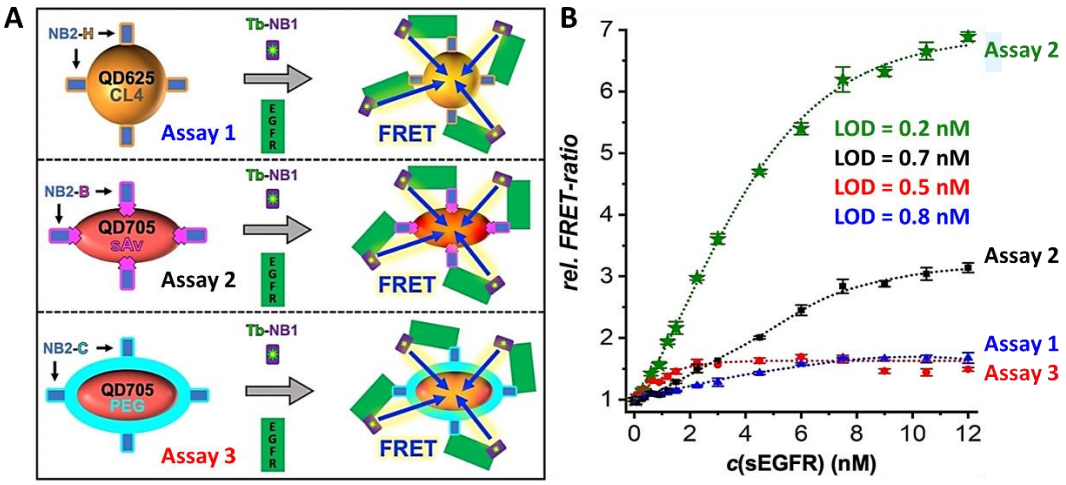

Figure 3.4. (A) Principle of the NB-based Tb-to-QD FRET sandwich immunoassays (see **Table 1** for explanation of abbreviations). Mixing of NB-QD acceptor conjugates (left side from **top** to **bottom**: NB2-H-QD625-CL4 (assay 1), NB2-B-QD705-sAv (assay 2), and NB2-C-QD705-PEG (assay 3)) with Tb-NB1 donor conjugates and sEGFR (gray arrows in the center) resulted in the formation of immunological sandwich complexes with close Tb-QD proximity for FRET (right side). Because the sEGFR is a Fc-chimera homodimer and NB1 and NB2 bind to different epitopes of each monomer, different donor-acceptor distances are possible, resulting in a mixture of high, low, and no FRET. The different sEGFR conformations and NB binding sites are shown in **Figure 3.4**. **(B)** EGFR sandwich FRET immunoassay calibration curves (*rel. FRET-ratio* is the *FRET-ratio* normalized to the blank sample) using Tb-NB1 as donor conjugates and NB2-H-QD625-CL4 (1.5 nM—blue, assay 1), NB2-B-QD705-sAv (1.5 nM—black, assay 2; 3.0 nM—green, assay 2), and NB2-C-QD705-PEG (1.5 nM—red, assay 3) as acceptor conjugates. Data points represent three (10 for the blank samples without sEGFR) independent measurements. Error bars represent standard deviations. The sEGFR concentrations (0, 0.075, 0.15, 0.30, 0.60, 0.90, 1.20, 1.50, 2.25, 3.0, 4.5, 6.0, 7.5, 9.0, 10.5, and 12.0 nM) are those in the 50 µL sample (they are 3 times lower in the total 150 µL assay volume).

The typical shape of sandwich assay calibration curves (increase followed by saturation) was caused by saturated binding of Tb-NB1 to sEGFR. The assays contained 50 µL of sample solution with different concentrations of sEGFR, 50 µL of NB2-QD solution (1.5 nM or 3.0 nM QD), and 50 µL of Tb-NB1 solution (6 nM NB1). The expected Tb-NB1 saturation at ≈6 nM EGFR (when each sEGFR binds one Tb-NB1) was confirmed for the assays containing NB2-H-QD625-CL4 and NB2-B-QD705-sAv. Considering that the same Tb-NB1 conjugates were used for all experiments, saturation at ≈2 nM sEGFR for the assays containing NB2-C-QD705-PEG must have been caused by limited binding of sEGFR to NB2-QD. Thus, only ≈1.3 NBs (2 nM sEGFR / 1.5 nM QD) were accessible on the QDs, which could have been caused by a low labeling ratio or by steric hindrance due to too dense labeling of NBs on the QD. This result confirmed the disadvantages of Cys-tag bioconjugation (vide supra), which requires bioconjugation at many different molar ratios to obtain optimized bioconjugates. Despite the differences in saturation, which resulted in a narrower dynamic concentration range for the NB2-C-QD705-PEG (≈0.5 nM to ≈2 nM) compared to the NB2-H-QD625 (≈0.8 nM to ≈8 nM) and NB2-B-QD705-sAv (≈0.7 nM to ≈12 nM) conjugates, the assays were functional for all three QD-NB conjugation strategies with similar limits of detection (LODs, 3 standard deviations above the zero concentration value) of 0.5±0.2 nM (NB2-C-QD705-PEG), 0.7±0.2

nM (NB2-B-QD705-sAv), and 0.8±0.2 nM (NB2-H-QD625) sEGFR (**Figure 3.5**). The sensitivity (slope of the linear part of the assay calibration curve) was approximately tripled from 0.33±0.01 nM^{-1} to 1.00±0.03 nM^{-1} by increasing the NB2-B-QD705-sAv concentration from 1.5 nM to 3 nM (green curve in **Figure 3.4B**), which also resulted in a lower LOD (0.20 ± 0.05 nM, **Figure 3.5**) that was similar to NB-based Tb-QD FRET assays using different QDs and functionalization strategies [142], [144].

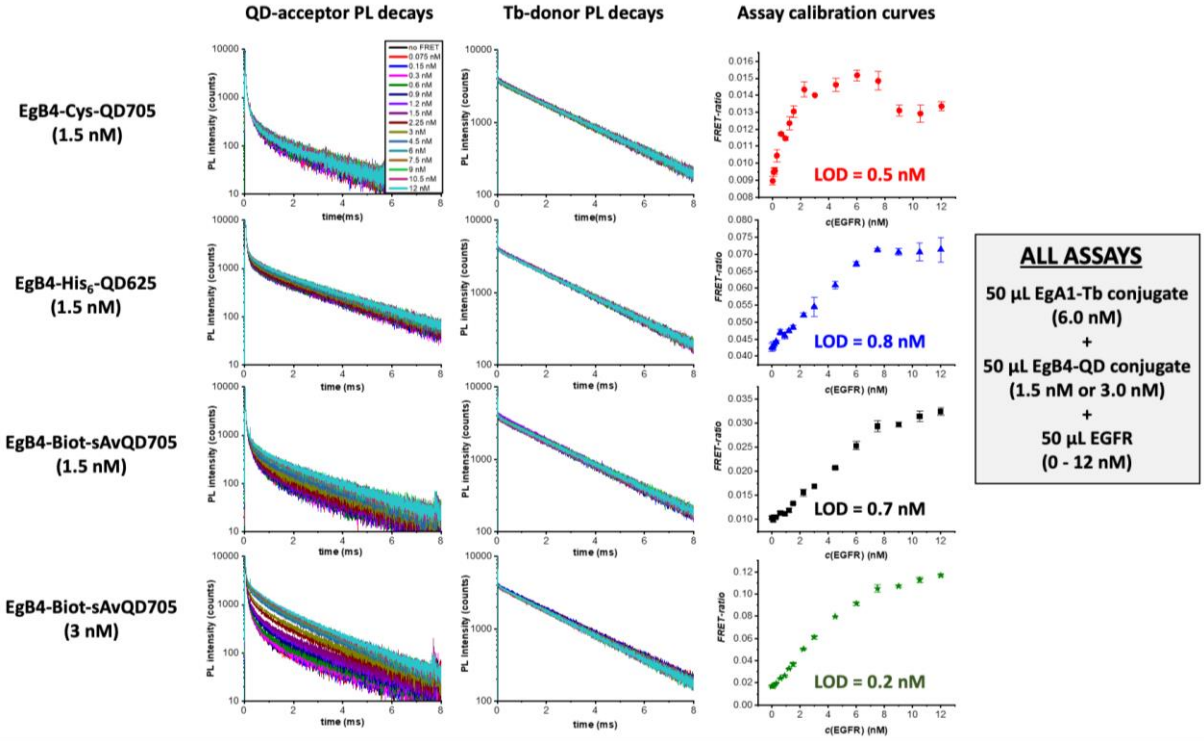

Figure 3.5. QD-acceptor (**left**) and Tb-donor (**center**) PL decay curves for sandwich immunoassays at different EGFR concentrations. QD-FRET-sensitization (increasing PL intensities with increasing EGFR concentrations) was strongest for EgB4-Biot-sAv-QD705 (and stronger for 3.0 nM compared to 1.5 nM QD concentration), followed by EgB4-His_6-QD625, and EgB4-Cys-QD705. Tb-FRET-quenching is much less intense (PL intensity differences are very weak and not well visible in the PL decay curves) because many Tb on the EgA1 will be too far away from the QD to engage in efficient FRET. Therefore, only the closest Tb will efficiently sensitize the QDs. PL decay curves were measured on a time-resolved fluorescence plate reader (Edinburgh Instruments), whereas the assay calibration curves (right) were measured on a KRYPTOR compact PLUS clinical diagnostic reader system (Thermo Fisher Scientific), which measures the PL intensities of QD and Tb in a time-gated detection window from 0.1 to 0.9 ms after pulsed excitation with a nitrogen laser at 337.1 nm and calculates the QD/Tb PL intensity ratio (FRET ratio) to perform ratiometric detection. LODs are the concentrations corresponding to the FRET ratio 3 times above standard deviation of the zero-concentration sample on the calibration curves.

3.3.3 sEGFR detection based on nanobody-on-QD surface displacement immunoassay

The benefits of versatile and rapid NB-QD bioconjugation and rapid and simple bioassays come with the drawback of relatively high LODs for quantifying sEGFR compared to other rapid FRET assays (using antibodies) [144] or to the clinical cut-off levels (threshold between normal and abnormal concentrations) of sEGFR (≈45 ng/mL or ≈0.22 nM) [155]. Therefore, we sought to exploit the distinct properties of His_6-tagged NBs to develop a new FRET assay concept that can combine both simplification and higher sensitivity. In this assay design, Tb-NB1-H was noncovalently, and as such reversibly, attached to the surface of QD625-CL4 via His_6 selfassembly, which led to Tb-to-QD FRET. Considering that both QD and sEGFR are significantly larger than NB, we hypothesized that this FRET signal can be disrupted by the release of Tb-NB1-H from QD625-CL4 when NB1 specifically binds to sEGFR (**Figure 3.6A**). Despite the fact that the NB1-sEGFR binding site is at the opposite end of the His_6 tag (non-competitive binding), the small size of the NB could be sufficient, such that steric hindrance would lead to a successful displacement. Both His_6 self-assembly to QDs (K_D ≈1 nM) [156] and binding of NB1 to EGFR (K_D≈0.6 nM, **Table 3.2**) are relatively strong, such that the NB displacement assay would provide the possibility to detect FRET signal changes at low target concentrations, while at the same time requiring only a single NB (labeled with Tb) and unconjugated QDs within an assay test kit (which could be very beneficial for long-term storage).

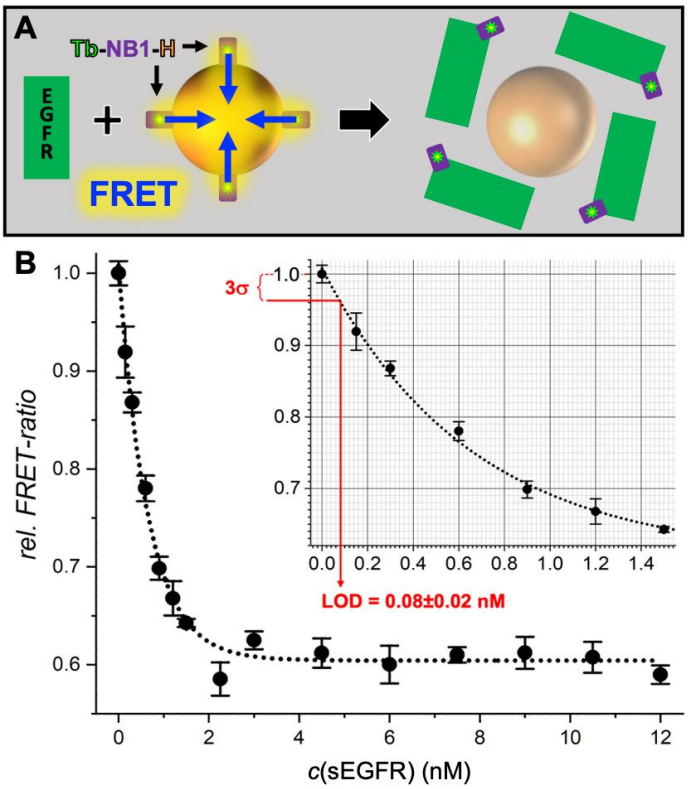

Figure 3.6. (A) Principle of Tb-to-QD FRET NB displacement immunoassays. Mixing of Tb-NB1-H donor conjugate and QD625-CL4 acceptor results in Tb-to-QD FRET. The presence of sEGFR leads to a displacement of Tb-NB1-H from the QD surface to sEGFR and disruption of FRET. **(B)** NB displacement FRET immunoassay calibration curves with a LOD (3 standard deviations below the zero concentration value – see inset) of 0.08±0.02 nM (16±4 ng/mL) sEGFR. Data points represent three (10 for the blank samples without sEGFR) independent measurements. Error bars represent standard deviations (σ). The EGFR concentrations are those in the 50 µL sample.

To experimentally demonstrate our hypothesis and for a direct comparison of the NB displacement FRET assay to the sandwich FRET assay, we started by simply replacing Tb-NB1 with Tb-NB1-H in the sEGFR assay that used NB2-H-QD625-CL4 as acceptor conjugates. Whereas the FRET-ratio in the sandwich assay curve increased with increasing sEGFR concentration, it decreased for the NB displacement assay, clearly showing the inverse principle, i.e., high *FRET-ratio* for Tb-NB1-H without sEGFR and low *FRET-ratio* for the bound Tb-NB1-H-EGFR complex. When NB2-H-QD625-CL4 was replaced by unconjugated QD625-CL4 (at otherwise identical assay conditions), the *FRET-ratio* decrease was even stronger (**Figures 3.7**).

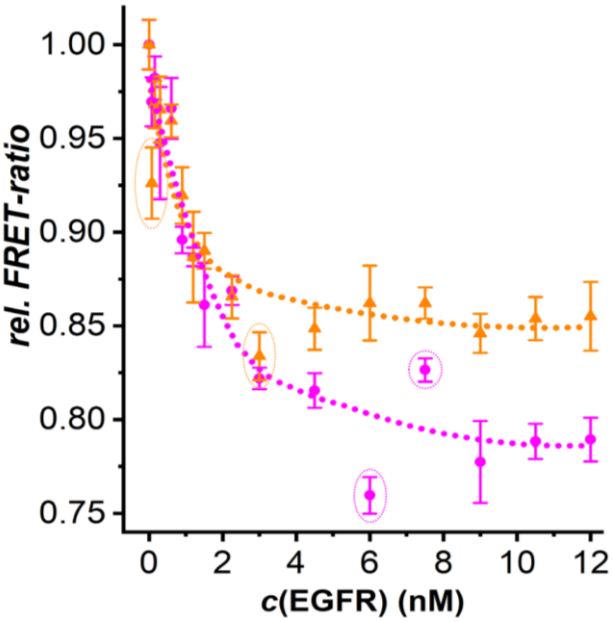

Figure 3.7. NB displacement FRET immunoassay calibration curves using Tb-EgA1-His_6 as donor NB conjugates and EgB4-His_6-QD625 (orange) or unconjugated QD625 (magenta) as acceptors. Note: The EGFR concentrations are those in the 50 µL sample (they are 3 times lower in the total 150 µL assay volume). Circled data points were considered outliers. Whereas the FRET-ratio in the sandwich assay curve (blue assay curve in **Figure 3.4B**) increased linearly up to ≈1.7 fold at ≈8 nM sEGFR, it decreased very steeply to ≈0.87-fold at ≈4 nM sEGFR for the NB displacement assay (orange assay curve). When NB2-H-QD625-CL4 was replaced by unconjugated QD625-CL4, the FRET-ratio decrease was even stronger (magenta assay curve).

To better understand the differences shown in **Figure 3.7**, we took a closer look at the PL decay curves of Tb donors and QD acceptors (**Figures 3.8 and 3.9**). When both NBs (Tb-NB1-H and NB2-H) were attached to the QD, the addition of sEGFR resulted in decreased intensity of the short QD PL decay (short distance), increased intensity of the medium QD PL decay (medium distance), and unchanged intensity of the long PL decay, which was caused by spectroscopic crosstalk of Tb PL into the QD detection channel (long distance without FRET). When only Tb-NB1-H was present, the short-distance component decreased very similarly with increasing EGFR concentration (displacement of Tb-NB1-H from QD625-CL4) but the medium-distance component increased almost two times less (Tb-NB1-H-EGFR-NB2-H-QD625-CL4 formation was not possible because NB2-H was not present in the assay). These different intensity changes of FRET at distinct distances showed that after displacement of Tb-NB1-H from QD625-CL4 by sEGFR binding, the formation of sandwich complexes (with

NB2-H still present on the QD) was still possible and that NB displacement was more efficient when only Tb-NB1-H was used in the assay.

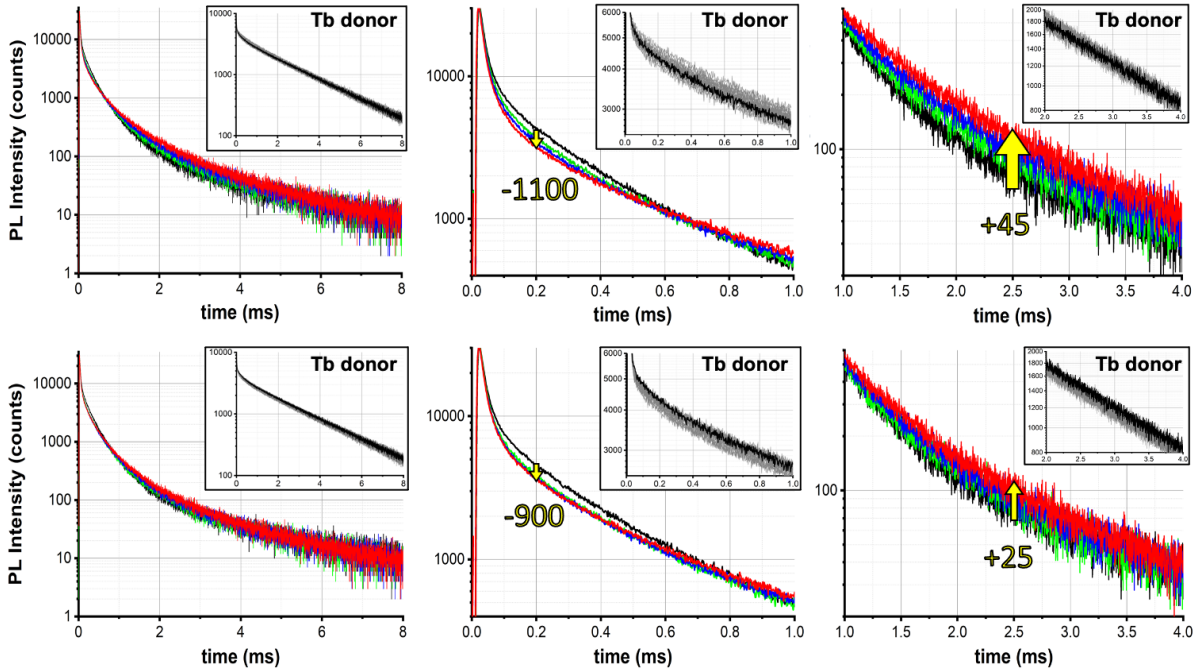

Figure 3.8. QD-acceptor and Tb-donor (insets) PL decay curves of the NB displacement EGFR immunoassays with Tb-EgA1-His_6 and EgB4-His_6-QD625 (**Top**) and Tb-EgA1-His_6 and unconjugated QD625 (**Bottom**) with no EGFR (black curves) and 1.2 nM (green), 2.25 nM (blue), and 7.5 nM (red) EGFR (curves for all measured concentrations are shown in **Figure 3.9**). For the Tb PL curves, all non-zero EGFR concentrations are shown in gray because there EGFR concentration dependent trend was much less pronounced. The graphs from left to right contain the same PL decay curves but on different time scales. **(Top)** The short QD PL decay component (zoom in the center) decreases by ~1100 counts at 0.2 ms (lower fraction of Tb-EgA1-His_6-QD at short Tb-QD distance) and the medium QD PL decay component (zoom on the right) increases by ~45 counts at 2.5 ms (higher fraction of Tb-EgA1-His_6-EGFR-EgB4-His_6-QD at slightly longer Tb-QD distance). At the same time, the short (and also slightly the medium) Tb PL decay component increases because overall there are more Tb-EgA1-His_6 attached to the QD because there are 5 times less Tb-EgA1-His_6 (6 nM) than EgB4-His_6 (30 nM because there are 20 EgB4-His_6 per 1.5 nM QD) in the assay. **(Bottom)** The short QD PL decay components decrease very similarly by ~900 counts at 0.2 ms (lower fraction of Tb-EgA1-His_6-QD at short Tb-QD distance) but the medium QD PL component increases much less by only ~25 counts at 2.5 ms (note that the overall counts in this time region are in the 50 to 150 counts region). At the same time, the short (and also slightly the medium) Tb PL decay component decreases because there is no second binding possibility (only on or off).

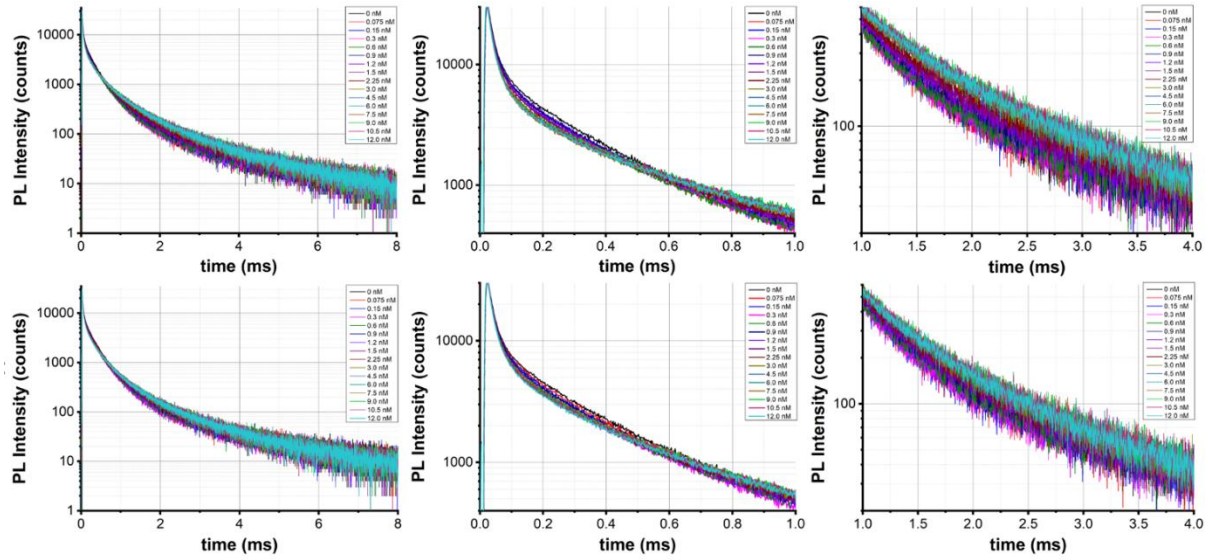

Figure 3.9. Same experiments as shown in **Figure 3.8** but with all measured concentrations.

Knowing that the NB displacement sensing principle was functional with Tb-NB1-H and QD625-CL4 as only assay components, we evaluated the assay performance at different Tb-NB1-H and QD625-CL4 concentrations and with a focus on the subnanomolar concentration range to determine the LOD (**Figure 3.6B**). In contrast to the sandwich immunoassays, for which an increase in NB2-QD concentration resulted in a better assay performance, the NB displacement assay performed significantly better at lower QD concentrations, most probably because of lower background signals that also resulted in lower standard deviations of the *FRET-ratio*. The QD625-CL concentration could be decreased 10-fold from 1.5 nM to 0.15 nM, which presented another advantage concerning costs and efficient use of materials. In addition, by reducing the Tb-NB1-H concentration by 50% from 6 nM to 3 nM, we could approximately triple the sensitivity from -0.133±0.017 nM^{-1} to -0.375±0.075 nM^{-1}, as measured by the slope of the assay curve for low concentrations of sEGFR (**Figure 3.10**). Importantly, the LOD could be decreased to 80±20 pM (16±4 ng/mL) sEGFR. This presented a 10-fold improvement compared to the sandwich immunoassay using NB2-H-QD625-CL4. The LOD is in the same range as antibody-based sandwich assays, and 3-fold lower than the clinical cut-off level of 45 ng/mL [144]. Notably, all these benefits were accomplished by a significant simplification of assay production and assay format.

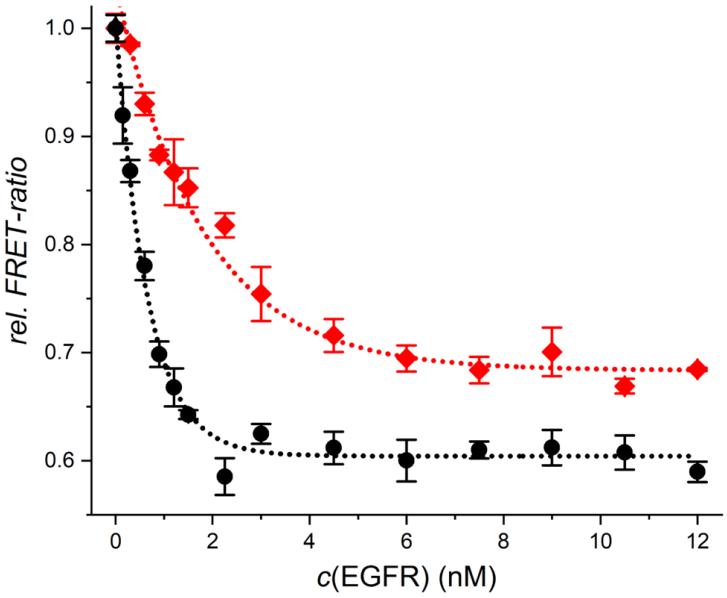

Figure 3.10. NB displacement FRET immunoassay calibration curves of assay mixtures containing 50 µL of different sEGFR concentrations (as given on the x-axis), 50 µL of 0.15 nM QD625-CL4, and 50 µL of 6 nM (red diamonds) or 3 nM (black dots) of Tb-NB1-H.

While the proof-of-concept of the novel NB displacement assay was clearly demonstrated, actual application in immunoassays for different targets requires the investigation of non-specific binding, implementation for different relevant biomarkers and different NBs, and target specificity. We first evaluated the NB displacement assay for the two biomarkers sEGFR and sEGFRvIII in serum containing samples, for which the many serum components can potentially cause significant non-specific binding and thus reduce the assay performance. Considering that commercial ELISA kits for human sEGFR use at least 10-fold dilution of serum samples [157], we investigated samples containing 5 to 30 vol% of fetal bovine serum (FBS). Although the assay performance decreased with increasing serum fractions, all FRET-ratios showed a clear target concentration dependence for both sEGFR and sEGFRvIII (**Figure 3.11A** and **B**). We selected 5-fold dilution of serum samples (i.e., 20 vol%) for a direct comparison of the assay performance in buffer and serum for both sEGFR and sEGFRvIII (**Figure 3.11C** and **D**). While the assay calibration curves for serum samples showed slightly lower sensitivity and overall reduction of the FRET-ratio, both sEGFR and sEGFRvIII could be quantified in the same concentration range as for the buffer samples.

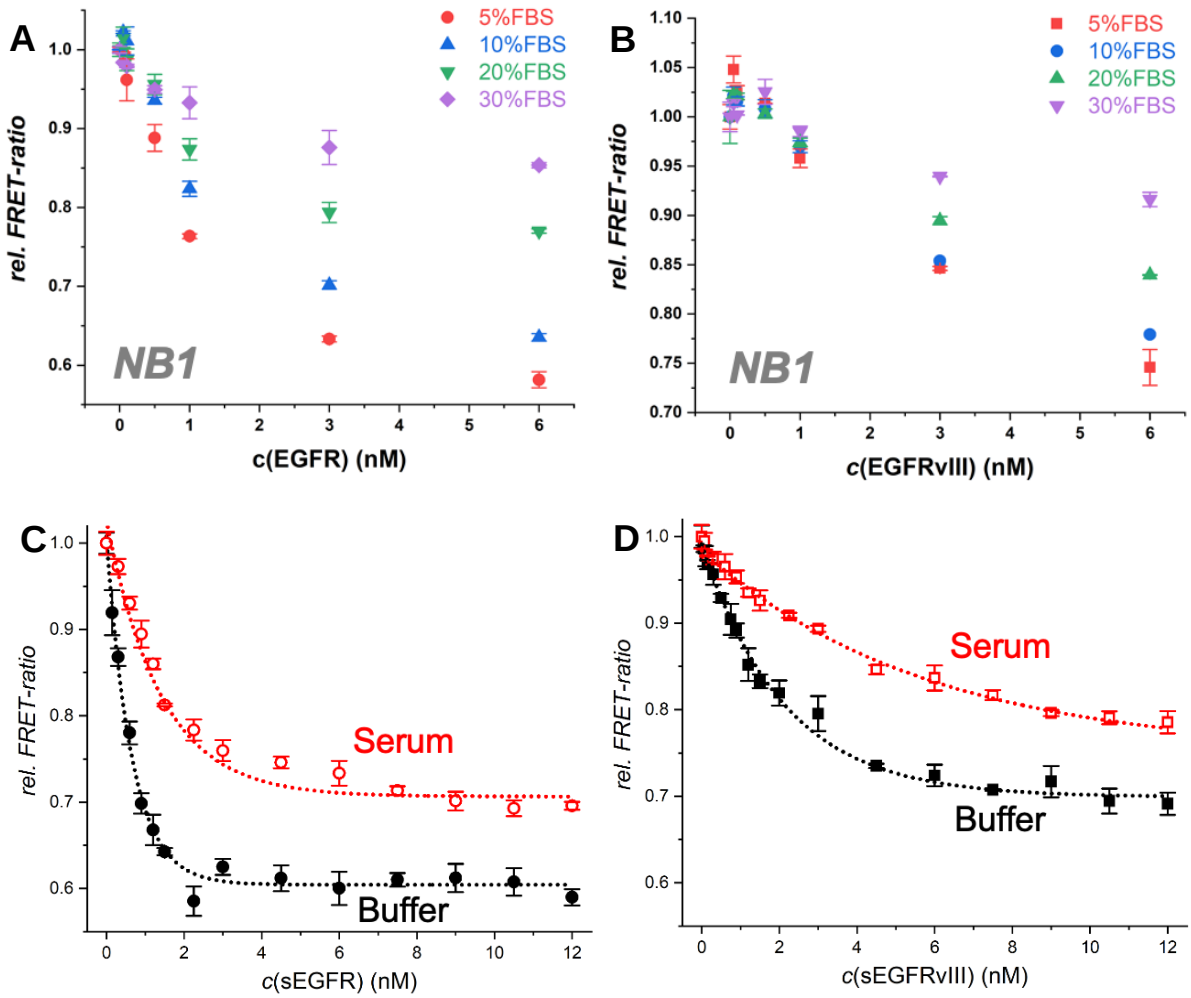

Figure 3.11. Influence of non-specific binding serum components. Relative FRET-ratios of the NB1+QD system against different sEGFR (**A**) or sEGFRvIII (**B**) concentrations in 50 mL buffer containing different amount of FBS (5%, 10%, 20%, 30%). Comparison of NB displacement immunoassays for sEGFR (**C**) and sEGFRvIII (**D**) in serum (20 vol%) and buffer. Data points represent three (10 for the blank samples without sEGFR) independent measurements. Error bars represent standard deviations (σ). The EGFR concentrations are those in the 50 µL sample.

Interestingly, sEGFRvIII quantification (**Figure 3.11D**) is less sensitive than sEGFR quantification (**Figure 3.11C**), which can be explained by the reduced domain **II** of sEGFRvIII (only residues 273-311 are retained compared to sEGFR) [153] and the binding of NB1 in the cleft formed between domains **II** and **III**. Thus, despite the independent binding of NB1 to the target and QD (EGFR binding site at the opposite end of the His_6 tag), the NB displacement assay performance is dependent on the NB-target binding position and affinity. To further investigate the influence of NB-target binding, we used NB2 instead of NB1. Although the

NB2-based displacement assay was functional, the assay curves showed significantly less sensitivity for sEGFR detection and serum fractions of more than 10 vol% resulted in only very weak sEGFR concentration dependence (**Figure 3.12**). Because the affinities of NB1 (~0.6 nM, **Table 3.2**) and NB2 (~0.7 nM, **Table 3.2**) for sEGFR are very similar, the different displacement behaviour can only be explained by the different binding sites (NB2 binds to domains **I** and **II**). The weak displacement of NB2 from the QDs also provides an explanation for the lowest sensitivity (smallest slope of calibration curve) of the NB2-H-QD625-CL4 (compared to NB2-B-QD705-sAv and NB2-C-QD705-PEG) sandwich immunoassays (**Figure 3.4**), even though the Tb-QD distance was shortest for the CL4 coated QDs. The NB2-H-QD625-CL4 sandwich assay is most probably driven by a combination of displacement and sandwich formation, with a slight advantage of sandwich formation and thus, an increasing *FRET-ratio* with increasing sEGFR concentration. Tuning the displacement efficiency by the NB-target binding sites presents an important lever for optimizing NB-displacement assays and an extensive investigation with a large library of NBs and targets would be highly interesting to fully understand the potential of this novel type of assay.

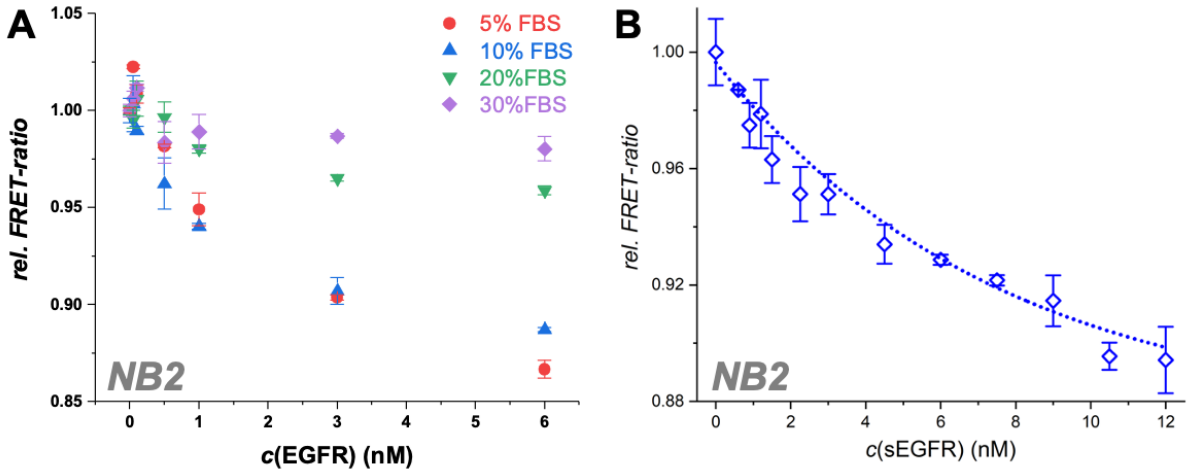

Figure 3.12. Influence of different NBs. **(A)** Relative FRET-ratios of the NB2+QD system against different sEGFR concentrations (0.05, 0.1, 0.5, 1, 3, 6 nM respectively) in 50 µL buffer containing different amount of FBS (5%, 10%, 20%, 30%). **(B)** NB displacement FRET immunoassay calibration curves of assay mixtures containing 50 µL of different sEGFR concentrations (in 50 µL buffer containing 10 % FBS), 50 µL of 0.15 nM QD625-CL4, and 50 µL of 3 nM Tb-NB2-H. For all measurements, incubation time was 90 min. Data points represent the measurement of three independent samples. Error bars represent standard deviations.

Finally, we evaluated the specificity of the NB-displacement assays for sEGFR and the possibility of shortening the assay incubation time. Both NB1 and NB2 based assays did not show any significant *FRET-ratio* changes when the sHER2 was used instead of sEGFR (**Figure 3.13A**). In addition, we showed the potential for further assay simplification by reducing the incubation time to only 15 to 30 minutes, which was found to be sufficient for sEGFR quantification (**Figure 3.13B** and **C**). Again, a more detailed study with many different targets and NBs would be necessary to fully assess specificity and simplicity optimization possibilities.

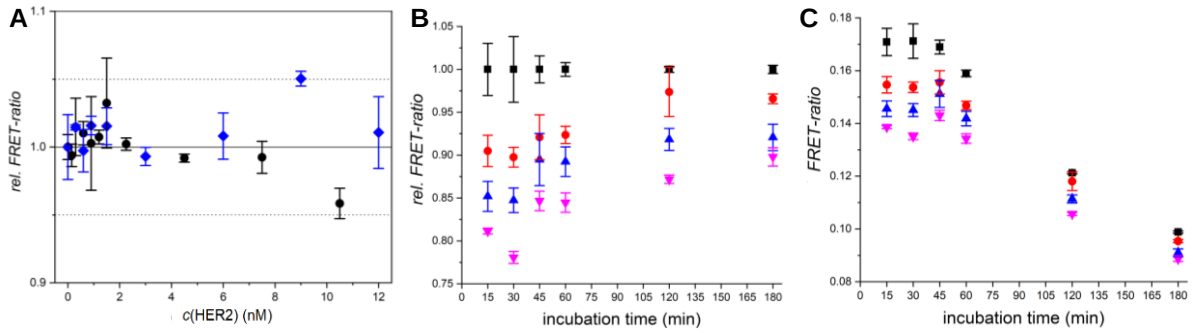

Figure 3.13. (A) sEGFR-specificity evaluation of NB1 (black) and NB2 (blue) based displacement FRET assay against HER2. FRET-ratio signal changes for HER2 are negligible. Incubation time dependence of the NB displacement FRET assay with four different sEGFR concentrations (balck, red, blue, and pink are for 0, 0.05, 0.5, and 1 nM of sEGFR, respectively). Although the relative **(B)** and absolute **(C)** FRET ratios slightly change over time (which is not problematic because of the ratiometric analysis), incubation for 15 or 30 min is sufficient for quantifying EGFR concentration differences.

3.4 Conclusions

In conclusion, we developed a nanobody-tag toolkit for simple, versatile, and efficient bioconjugation to QDs with different surface coatings, sizes, and PL colors. The immunotargeting functionality of the NB-QD conjugates was demonstrated on homogeneous TG-FRET immunoassays against sEGFR, using two different, non-competing EGFR-specific NBs (NB1 functionalized with Tb and NB2-tag attached to QDs). Despite the differences of QD sizes and coatings and NB orientations on the QD surfaces, NB1-EGFR-NB2 sandwich complexes were formed for all NB-QD conjugates, which resulted in an sEGFR concentration-dependent increase of Tb-to-QD FRET with subnanomolar LODs in low-volume (50 µL) samples and the best assay performance when using biotin-tagged NBs and sAv-coated QDs. QD-bioconjugation with His_6 and biotin tagged NBs was significantly faster, simpler, and easier

to quantify compared to Cys tagged NBs. A significantly simplified immunoassays format combined with improved analytical performance was realized by exploiting the displacement of His_6-tagged Tb-NB1 from the QD surface. Despite the independent (non-competitive) binding of His_6 to the QD surface and Tb-NB1 to sEGFR, NB-displacement was sEGFR concentration dependent. The displacement mechanism was further studied using a different target (sEGFRvIII) and a different NB (NB2), which showed that modification of the NB-target binding site can be used for tuning the displacement efficiency. The rapid, wash-free, and simple assay format (only on Tb-NB conjugate + unconjugated QDs) required 30-fold less QDs and afforded an LOD of 80±20 pM (16±4 ng/mL), which was 3-fold below the clinical cut-off level of sEGFR. The relevance of the NB-displacement assay for clinical diagnostics was further demonstrated by quantifying both sEGFR and sEGFRvIII in serum samples. Mix-and-measure NB-on-QD displacement FRET assays can significantly reduce assay development, production, and material costs, improve QD storage conditions in assay kits, and provide clinically relevant analytical performance for biomarker quantification, all of which are highly important benefits for translating QD-based biosensors into daily use in bioanalytical research and clinical diagnostics.

CHAPTER 4

Tb-to-QD FRET-based temporal multiplexing of ssDNA

4. Tb-to-QD FRET-based temporal multiplexing of ssDNA

4.1 Introduction

With the rapid discovery of new biomolecules, biochemical interactions, and biological systems and pathways, multiplexed biosensing becomes increasingly important because it can provide a more comprehensive view to monitor, understand, and manipulate complicated biosystems, leading to advancements in disease diagnosis and treatment, environmental monitoring, and fundamental biological research. Arguably, photoluminescent (PL) detection is ideal for multiplexing due to its rapid response, high sensitivity, quantitative capabilities, and the wide range of available fluorophores with versatile photochemical and photophysical properties [12], [23], such as organic dyes [44], [140], [158]–[160], fluorescent proteins [161], quantum dots [162], [163], and lanthanides complexes or nanoparticles [163], [164]. Typically, PL multiplexing can be realized by quantifying multiple targets via the detection of distinct emission spectra of fluorophores in different spectral (or color) channels. However, this so-called spectral multiplexing is facing the challenge of spectral overlap from the emission spectra of two or more PL probes that share common wavelengths, leading to reduced specificity and a limited number of available detection channels.

For the purpose of improving PL multiplexing capabilities, PL lifetime-dependent measurements are a powerful tool to extend simultaneously multiplexing in the temporal dimension [165]–[170]. PL decay times could be tuned from tens of microseconds to a few milliseconds by varying the doping concentrations of different lanthanide ions in upconversion nanoparticles (UCNPs) [170] or tuning the distance between a luminescent lanthanide (Ln) complex donor and an organic dye acceptor in a Förster resonance energy transfer (FRET) pair [171]. Although the proofs-of-concept of multiplexing assays based on these UCNPs or the proposed FRET pair were successfully implemented in immunoassays and DNA analysis, several drawbacks need to be solved. Firstly, UCNPs usually possess very low PL quantum yields and multiexponential PL decays, which makes the assay require long acquisition times, and high materials' concentration and limits the lifetime distinction efficiency, leading to a low sensitivity and selectivity. The Ln-to-dye FRET-based temporal multiplexing assays show improved capability for decay time distinction but its nanomolar target concentrations could

not meet the requirement of many biochemical and biomolecular studies, where extremely low concentrations (fM–pM) of various similar targets need to be specifically quantified [171]. It has been reported that rolling circle amplification (RCA) [71], hybridization chain reaction (HCR) [172], and catalytic hairpin assembly (CHA) [173] techniques are successfully used in FRET-based temporal multiplexing for ultra-sensitive detection of nucleic acids, but they usually require long incubation time, complex design, and specific thermal cycling, which is not favorable for rapid diagnostic applications. These limitations underscore the continued importance of developing sensitive, selective, simple, and rapid PL temporal multiplexing technologies.

In this chapter, a temporal multiplexing strategy is presented for single-strand DNA (ssDNA) triplexing based on the time-gated (TG) PL measurement of a Lumi4-Tb complex (Tb)-to-QD FRET pair with temporally distinct PL decays tuned by the Tb-QD distance. As shown in **Figure 4.1A**, the Tb-to-QD FRET-based PL probes were prepared by conjugating QDs with peptide-cDNAs (cDNA is part of the complementary DNA of a specific target DNA), and another type of peptide-DNA linkers hybridized with different Tb-DNA to form Tb-QD FRET probes 1, 2, and 3 complexes with different Tb-QD distances (0 nucleotides (nt), 10 nt, and 14 nt distance between Tb and QD, respectively). The various Tb-QD distances result in different FRET efficiencies, which can be transduced to PL signals with different decay times. Another component of this multiplexing sensor are magnetic beads (MBs), which were conjugated with biotin-cDNAs (here, the biotin-cDNA contains another part of the complementary DNA of a specific target DNA). As shown in **Figure 4.1B**, with the presence of corresponding DNA targets, the FRET-based PL probes can be immobilized onto the MB surface through simple DNA hybridization (all the DNA sequences are displayed in **Table 4.1** in **Section 4.2.1**). After magnetic separation and resuspension, the background signal from free Tb-QD FRET probes can be suppressed, and the TG measurements of FRET-sensitized long-decay-time QDs in distinct time windows after pulsed excitation can realize the autofluorescence-free and selective detection of multiple DNA targets.

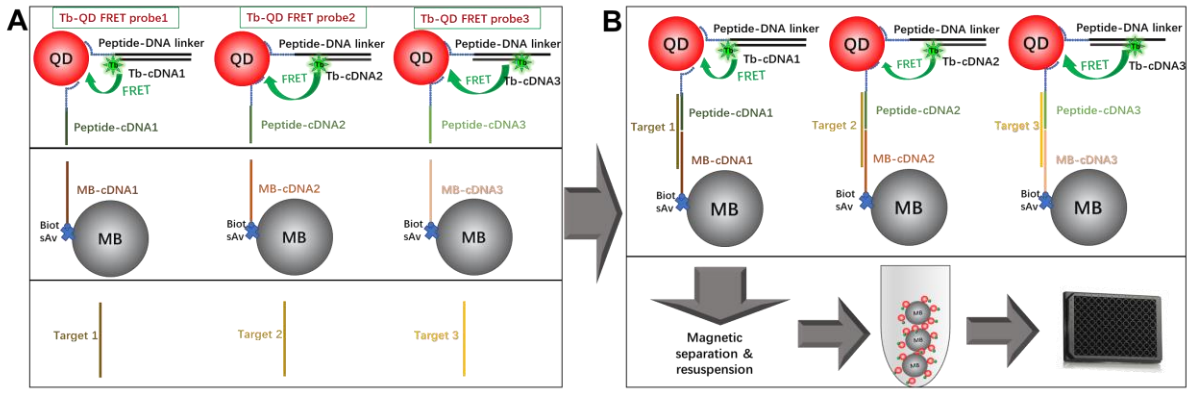

Figure 4.1. Simultaneous quantification of multiple DNA targets based on Tb-QD FRET. **(A)** The designs of Tb-QD FRET-based PL probes, bioconjugates of molecular beacons (MBs) with complementary DNA (cDNA), and the three DNA targets. **(B)** The assay procedure of the simultaneous quantification of three DNA targets.

4.2 Materials and methods

4.2.1 Materials

The luminescent terbium complex, Lumi4-Tb-NHS (Tb) was provided by Lumiphore Inc. 625nm emitting organic Qdots (QD625, core-shell diameter of ~9.2 nm) [150] and Dynabeads MyOne Streptavidin T1 magnetic beads (MB, diameter of 1 μm) covalently coupled to streptavidin were purchased from Thermo Fisher Scientific. Peptide−oligonucleotides were synthesized by Biosynthesis. All other oligonucleotides were synthesized and purified by Eurogentec. All sequences and modifications of nucleic acids used in this work are summarized in **Table 4.1**. Tris(hydroxymethyl)-aminomethane, ethylenediaminetetraacetic acid (EDTA), hydrochloric acid (HCl), sodium hydroxide (NaOH), sodium tetraborate decahydrate ($Na_2B_4O_7{\cdot}10H_2O$), sodium bicarbonate ($NaHCO_3$), bovine serum albumin (BSA), and HEPES were purchased from Sigma-Aldrich. NaCl was purchased from Duchefa. Zeba Spin Desalting Columns (7 kDa MWCO) were purchased from Thermo Fisher Scientific. All chemicals were used as received. High-quality Milli-Q water with a resistivity of 18.2 MΩ cm was used for preparing solutions.

Table 4.1. Sequences and modifications of DNA probes and targets.

Name	Sequence (5'-3')	Modification
peptide-DNA	TAGCTCGACAAAGTGCTCATAGTGCAGGTAG	5'-H6SLGAAAGSGC-SMCC-amino
Tb-DNA1 (for 0 nt distance)	CTACCTGCACTATGAGCACTTTGTCGAGCTA	3'-C3-NH_2
Tb-DNA2 (for 10 nt distance)	CTACCTGCACTATGAGCACTT	3'-C3-NH_2
Tb-DNA3 (for 14 nt distance)	CTACCTGCACTATGAGCACTTTGTCGA	5'-C3-NH_2
peptide-cDNA1	CCACAACTTCAACATCAGTCTGATAAGCTA	5'-Acetyl-H6SGK (maleimide-thiol); 3'-OH
Target 1	CTGACCCATGCCCACCATCATAGCTTATCAGACTG ATGTTGAAGTTGTGG	
Biotin-cDNA1	TGATGGTGGGCATGGGTCAGAAAAAAAAAA	3'-biotin
peptide-cDNA2	AGTCTAGTGCGACACGACA	5'-N-H6SLGAAAGSGC-SMCC-amine
Target 2	ACCAGAGTTAAAAGCAGCCCTTGTCGTGTCGCAC TAGACT	
Biotin-cDNA2	AGGGCTGCTTTTAACTCTGGTAAAAAAAAAA	3'-biotin
peptide-cDNA3	AGAACGGACTGAGCAGGAGAAAGATTTTCTATG GA	5'-N-H6SLGAAAGSGC-SMCC-Amine
Target 3	GTTTCAGCTTTGCAACCATACTCTCCATAGAAAAT CTTTCTCCTGCTCAGTCCGTTCT	
Biotin-cDNA3	GAGTATGGTTGCAAAGCTGAAACAAAAAAAAAA	3'-biotin

4.2.2 Tb-DNA conjugation

Three different Tb-DNA conjugates were prepared by mixing Lumi4-Tb-NHS in concentration excess to three different amino-functionalized oligonucleotides (Tb-DNA1, 2 or 3 as shown in **Table 4.1**) in 100 mM carbonate buffer at pH 9.0, respectively. The mixtures were incubated overnight at 4 ℃ and purified 3 times with HEPES buffer (100 mM, pH 7.4) by Zeba Spin Desalting Columns (7 kDa MWCO). Tb concentration of the conjugate was determined by measuring the absorbance at ca. 340 nm using a molar absorptivity of ca. 26,000 M^{-1} cm^{-1} as provided by the manufacturer. DNA was quantified by absorbance measurements at ca. 260 nm. The conjugation ratio was determined to be higher than 0.9 Tb/DNA by a linear combination of the respective absorbance values of LTC and DNA within the conjugate.

4.2.3 The preparation of Tb-to-QD FRET-based PL probes

The prepared Tb-DNA conjugates were then used to form Tb-QD FRET configurations where the distance between Tb and QD differs due to the different lengths of the Tb-DNAs. Specific Tb-DNA conjugates were mixed with peptide-DNA linkers, QD625 and the

corresponding peptide-cDNAs (at a concentration ratio of 20:20:1:10) in Hybridization Buffer (20 mM Tris-Cl, 500 mM NaCl, 0.1 % BSA, pH 8.0), and incubated at room temperature for 3h, followed by storage at 4℃ for long term use. During the incubation, histidine tags of peptide-DNA and peptide-cDNA were attached to the Zinc-rich QD625 surface via metal affinity self-assembly, which allows the Tb-DNA sequence to hybridize with peptide-DNA linker to form Tb-QD-peptide-cDNA probes. The functionalized Tb-QD FRET-based probes can not only generate PL signal but also recognize and bind with specific DNA targets.

4.2.4 MB-cDNA conjugation

The conjugates of biotin-cDNA with streptavidin magnetic beads (MB) were prepared according to the protocol from Thermo Fisher Scientific [174]. Firstly, MBs were washed according to the following steps: **(i)** Resuspend the beads in the vial (i.e., vortex for >30 sec, or tilt and rotate for 5 min). **(ii)** Transfer the desired volume of beads to a new tube. **(iii)** Add an equal volume (or at least 1 mL) of Washing Buffer (5 mM Tris-HCl, 0.5 mM EDTA, and 1M NaCl, pH 7.5) and resuspend. **(iv)** Place the tube on a magnet for 1 min and discard the supernatant. **(v)** Remove the tube from the magnet and resuspend the washed beads in 1mL Washing Buffer. **(vi)** Repeat steps **iv**–**v** twice, for a total of 3 washes.

Then three different biotin-cDNAs (Biotin-cDNA1, 2, and3) were immobilized onto MBs respectively through biotin-streptavidin non-covalent binding according to the following steps: **(i)** Resuspend washed MBs in 2× Washing Buffer (10 mM Tris-HCl, 1 mM EDTA, and 2M NaCl, pH 7.5) to a final concentration of 5 μg/μL (half of the original concentration (10 mg/mL)). **(ii)** Add an equal volume of biotinylated DNA (the binding ratio between DNA and MBs is 400 pmol cDNA per mg of MB). Optimal binding occurs when the NaCl concentration is reduced from 2 M to 1 M. **(iii)** Incubate for 15 min at room temperature using gentle rotation. **(iv)** Separate the biotinylated DNA or RNA-coated beads with a magnet for 2–3 min. **(v)** Wash the coated beads 2–3 times with 1X Washing Buffer. **(vi)** Resuspend the beads with the immobilized cDNAs in Hybridization Buffer for downstream applications.

4.2.5 Spectroscopic characterization

Absorption spectra (Cary 60 UV-Vis Spectrophotometer, Agilent) and emission spectra (Fluorolog-3, HORIBA) for Tb, and QD samples were recorded in HEPES (100 mM, pH 7.4)

and Na-tetraborate buffer (100 mM Na-tetraborate, 0.1 M NaCl, pH 8.5), respectively.

4.2.6 Single and triple DNA targets sensing assays

Single sensing assay

All FRET assays were prepared in Hybridization Buffer (20 mM Tris-Cl, 500 mM NaCl, 0.1% BSA, pH 8.0). For single target sensing, 50 μL of the corresponding Tb-QD-peptide-cDNA probes and 50 μL of the corresponding MB-cDNAs at constant concentrations were mixed with 50 μL specific DNA target (at different concentrations). The mixtures was incubated at 37℃ for 30 min, then followed by cooling down to room temperature (20℃) for 30 min. After incubation, the mixtures were washed three times through magnetic separation according to the procedure in **Section 4.2.4**, and then resuspended with Hybridization Buffer. In the end, 140 μL mixture was taken from the total reaction volume (150 μL) and measured in black 96-well microtiter plates on a fluorescence lifetime plate reader (Edinburgh Instruments) using 4000 detection bins of 2 μs integration time and pulsed nitrogen laser (MNL 100, LTB Berlin) excitation (337.1 nm, 20 Hz). The PL intensities of Tb donor and QD625 acceptor were measured by using optical bandpass filters with 494±12 nm (Semrock) for the donor channel (CHD) and 640±14 nm (Semrock) for the acceptor channel (CHA).

The single target sensor assays contained 0.1 nM Tb-QD-cDNA probes (Concentration is determined by QDs, and the corresponding cDNA on QD is at 2 Nm.), 40 nM cDNA-MBs (concentration determined by cDNAs on MB), and increasing concentrations of DNA target (target1: 625 fM-8nM; target2: 2.5 pM-16nM; target3:6.25 pM-40nM). All samples were prepared three times except for the blank samples (target concentration is 0), which were prepared 10 times.

Triplexing assay

For triplexing, 50 μL mixed three types of Tb-QD-peptide-cDNA probes (Tb-QD-peptide-cDNA1, Tb-QD-peptide-cDNA2, and Tb-QD-peptide-cDNA3) and 50 μL mixed three types of MB-cDNAs (MB-cDNA1, MB-cDNA2 and MB-cDNA3) at constant concentrations were mixed with 50 μL mixed three types of DNA targets at different concentrations. The mixtures were incubated at 37℃ for 30 min, then followed by cooling down to room temperature (20℃) for 30 min. After incubation, the mixtures were washed three times through magnetic separation

according to the procedure in **Section 4.2.4**, and resuspended with Hybridization Buffer. In the end, 140 µL mixture was taken from the total reaction volume (150 µL) and measured in black 96-well microtiter plates on a fluorescence lifetime plate reader (Edinburgh Instruments) using 4000 detection bins of 2 µs integration time and pulsed nitrogen laser (MNL 100, LTB Berlin) excitation (337.1 nm, 20 Hz). Temporal multiplexing assays used three TG PL detection windows (W1: 0.1 to 1.5 ms, W2: 1.5 to 3.0 ms, and W3: 3.0 to 8.0 ms) and PL intensity detection used optical bandpass filters with 494±12 nm (Semrock) for the Tb detection channel and 640±14 nm (Semrock) for the QD625 detection channel.

For the triplexing and recovery rate experiments, the assays contained 0.1 nM Tb-QD-cDNA1 probe, 0.1 nM Tb-QD-cDNA2 probe, 0.1 nM Tb-QD-cDNA3 probe, 40 nM MB-cDNA1, 40 nM MB-cDNA2, 40 nM MB-cDNA3, and different concentrations of three DNA target (target1: 625 fM-8nM; target2: 2.5 pM-16nM; target3:6.25 pM-40nM). All samples were prepared three times except for the blank samples (target concentration is 0), which were prepared 10 times.

4.3 Results and discussion

4.3.1 Photophysical properties of Tb-QD625 FRET pair

All the spectra of the Tb-QD625 FRET pair are shown in **Figure 4.2**. According to the FRET theory [22], energy transfer occurs when there is an energetic resonance between donor emission and acceptor absorption, as expressed by the spectral overlap integral:

$$J = \int \bar{I}_D(\lambda)\varepsilon_A(\lambda)\lambda^4 \, d\lambda \tag{4.1}$$

where $\bar{I}_D$ is the area-normalized (to unity) PL spectrum of donor, and $\varepsilon_A(\lambda)$ is the molar absorption of acceptor (**Figure 4.2**).

The Förster distance R_0 (the donor-acceptor distance for which FRET is 50 % efficient) between Tb-QD625 FRET pair was calculated as R_0 = 10.3±0.5 nm by using **Equation 4.2**.

$$R_0 = 0.02108(\kappa^2 \Phi_D n^{-4} J(\lambda))^{\frac{1}{6}} \tag{4.2}$$

The orientation factor (κ^2) was taken as 2/3, due to dynamic averaging as found for other Tb-QD or Tb-Cy dye donor-acceptor systems [23]. The refractive index *n* of the aqueous

solution was taken as 1.35. Φ_D represents the quantum yield of FRET donors which was measured as 0.80 ± 0.05 for Tb in Lumi4-Tb complex.

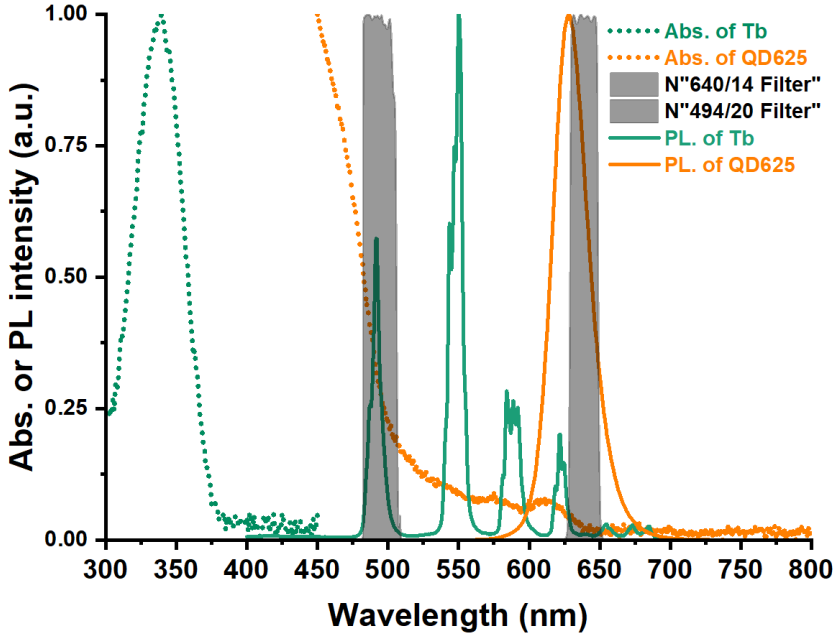

Figure 4.2. Emission (green solid line) and absorption (green dotted line) spectra of Tb (green), emission (orange solid line) and absorption (orange dotted line) spectra of QD625 (QD absorption is only shown until 450 nm) that partly overlaps with Tb emission, and filter transmission spectra (gray) used for Tb donor and QD acceptor time-resolved PL detection.

4.3.2 The design of Tb-QD FRET probes

In this work, three Tb-QD FRET configurations were designed as shown in **Figure 4.3 (top)**, where the distance between Tb and QD is determined by the peptide linker plus 0 nt, 10 nt, and 14 nt, respectively. Notably, the 10 nt distance configurations have single-stranded (ss)DNA between Tb and peptide, whereas the 14 nt configuration has double-stranded (ds)DNA. In a previous study, we found that the extension of ssDNA on QDs corresponds to a distance of ~0.15 nm per nt, whereas dsDNA extended with ~0.31 nm per nt on QDs [150]. For all three configurations, the concentration ratio between Tb and QD625 is fixed as 20:1. Corresponding PL decay curves of FRET-quenched Tb donor and FRET-sensitized QD625 acceptor of different configuration are also shown in **Figure 4.3 (bottom)**. According to FRET theory, FRET efficiency (E_{FRET}) is proportional to the inverse sixth power of the donor-acceptor distance, and the higher E_{FRET}, the stronger the quenching of the donor PL decay time (τ_D) [175],

[23]. Thus, three different Tb-to-QD625 FRET probes designed in our work exhibit different FRET-quenched donor PL decay times (τ_{DA}). Owing to the big difference between the PL lifetimes of Tb (~ms) and QD625 (~ns), the FRET-sensitized lifetime of the QD625 acceptor (τ_{AD}) can be taken the same as the FRET-quenched lifetime of the Tb donor ($\tau_{AD} = \tau_{DA}$ when $\tau_D \gg \tau_A$) [16]. These relations between FRET efficiency, distance, and PL decay times are summarized in **Equation 4.3** [16], [23], [175].

$$E_{\mathrm{FRET}} = \frac{R_0^6}{R_0^6+R^6} = 1 - \frac{\tau_{\mathrm{DA}}}{\tau_{\mathrm{D}}} = 1 - \frac{\tau_{\mathrm{AD}}}{\tau_{\mathrm{D}}} \tag{4.3}$$

Therefore, the different distances between Tb and QD625 (0 nt, 10 nt, and 14 nt) result in different PL lifetimes and the PL decay curves of both donors and acceptors, with significantly distinguishable time-dependent PL intensities over the entire PL decay. The designed FRET configurations were then used as PL probes for the following temporal multiplexing assays.

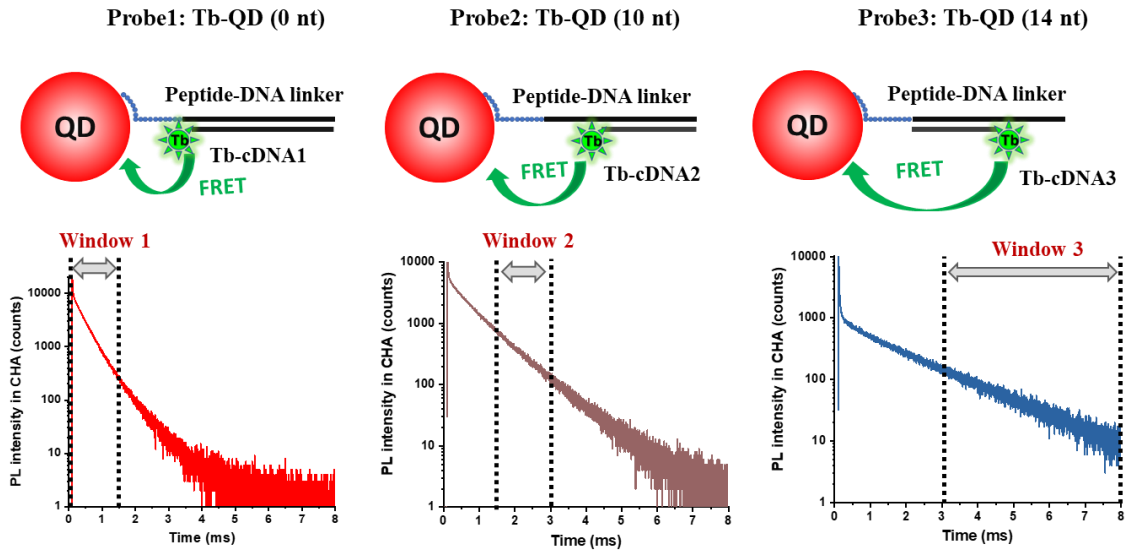

Figure 4.3. Distance-tuned FRET configurations with distinguishable PL decays for temporal multiplexing. **(Top)** Tb conjugated cDNAs with variable lengths or directions hybrid with peptide-DNA linkers on QD625, resulting in distinguishable PL decay curves of FRET-sensitized QD625 acceptors. **(Bottom)**, and three separate detection windows were selected for the following temporal multiplexing (W1: 0.1 – 1.5 ms; W2: 1.5 – 3.0 ms; W3: 3.0 – 8.0 ms).

4.3.3 PL decay fitting and distance calculations

According to **Equation 4.3**, the FRET efficiencies and actual distance between Tb and QD625 in each PL probe can be determined based on the original PL decay time of Tb (τ_D) and FRET-quenched PL decay time (τ_{DA}) of Tb, or FRET-sensitized QD625 PL decay time τ_{AD},

which can be achieved from multiexponential fitting of PL decay curves.

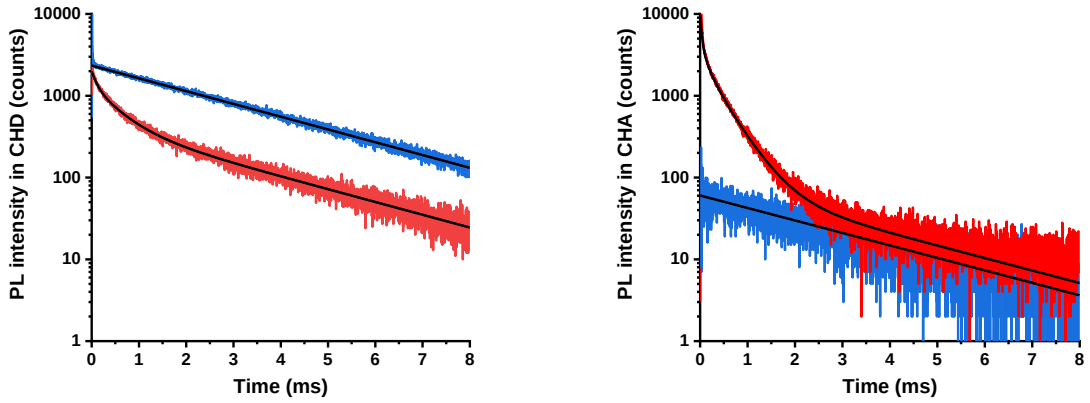

Figure 4.4. PL decay curves of Tb donor (**left**) and QD625 acceptor (**right**) used for PL decay time fitting and distance calculation in the Tb-QD FRET probe1, where there is 0 nt (plus peptide) between Tb and QD. Concentrations of Tb and QD are 10 nM and 0.5 nM, respectively. Blue and red curves are for Tb alone, and FRET probe1 respectively, and central black curves represent the fitting results from below.

Fitting results (all decay times in µs) of decay curve of Tb-QD probe1 in donor channel (CHD) (3-exponential fit with a contribution of Tb at a constant PL decay time of 2870 µs, which was fixed, whereas all other fit parameters were variable):

τ_D	A_D	τ_{DA1}	A_{DA1}	τ_{DA2}	A_{DA2}	$<\tau_{DA}>$	E_{FRET}
2780	2339	–	–	–	–	–	–
2780	435	113	648	535	904	360	0.87
R_0 = 10.3 nm				distance R (nm)		7.4	7.4

Fitting results (all decay times in µs) of decay curve of Tb-QD probe1 in acceptor channel (CHA) (4-exponential fit with a contribution of Tb at a constant PL decay time of 2848 µs, which was fixed, whereas all other fit parameters were variable):

τ_D	A_D	τ_{AD1}	A_{AD1}	τ_{AD2}	A_{AD2}	τ_{AD3}	A_{AD3}	$<\tau_{AD}>$	E_{FRET}
2848	60	QD background		D in the absence of A (mono-exponiential)					
2848	85	35	5636	150	1503	442	2516	397	0.86
R_0 = 10.3 nm						distance R (nm)		7.5	7.5

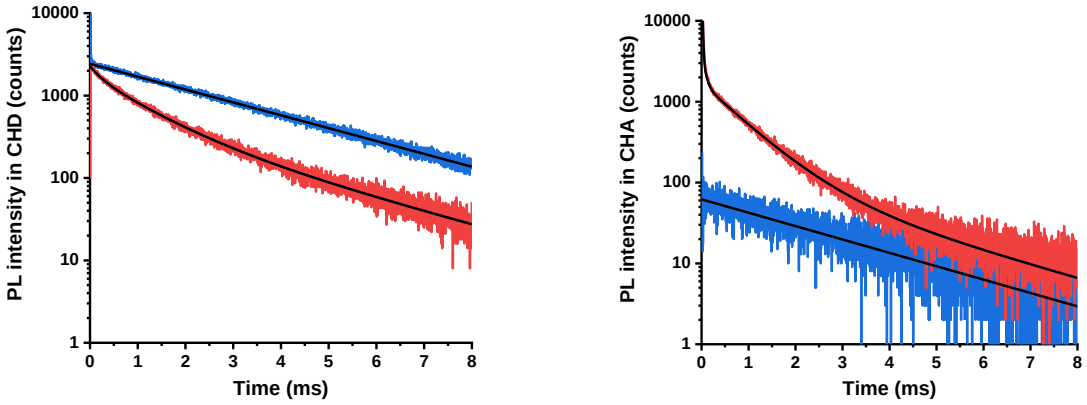

Figure 4.5. PL decay curves of Tb donor (**left**) and QD625 acceptor (**right**) used for PL decay time fitting and distance calculation in the Tb-QD FRET probe2, where there is 10 nt (plus peptide) between Tb and QD. Concentrations of Tb and QD are 10 nM and 0.5 nM, respectively. Blue and red curves are for Tb alone, and FRET probe2 respectively, and black lines represent the fit results from below.

Fitting results (all decay times in μs) of decay curve of Tb-QD probe2 in CHD (3-exponential fit with a contribution of Tb at a constant PL decay time of 2781 μs, which was fixed, whereas all other fit parameters were variable):

τ_D	A_D	τ_{DA1}	A_{DA1}	τ_{DA2}	A_{DA2}	$<\tau_{DA}>$	E_{FRET}
2781	1905	–	–	–	–	–	–
2781	813	161	489	995	877	700	0.75
R_0 = 10.3 nm				distance R (nm)		8.5	8.5

Fitting results (all decay times in μs) of decay curve of Tb-QD probe2 in CHA (4-exponential fit with a contribution of Tb at a constant PL decay time of 2698 μs, which was fixed, whereas all other fit parameters were variable):

τ_D	A_D	τ_{AD1}	A_{AD1}	τ_{AD2}	A_{AD2}	τ_{AD3}	A_{AD3}	$<\tau_{AD}>$	E_{FRET}
2698	48	QD background		D in the absence of A (mono-exponential)					
2698	123	30	6044	115	638	765	977	720	0.73
R_0 = 10.3 nm						distance R (nm)		8.6	8.6

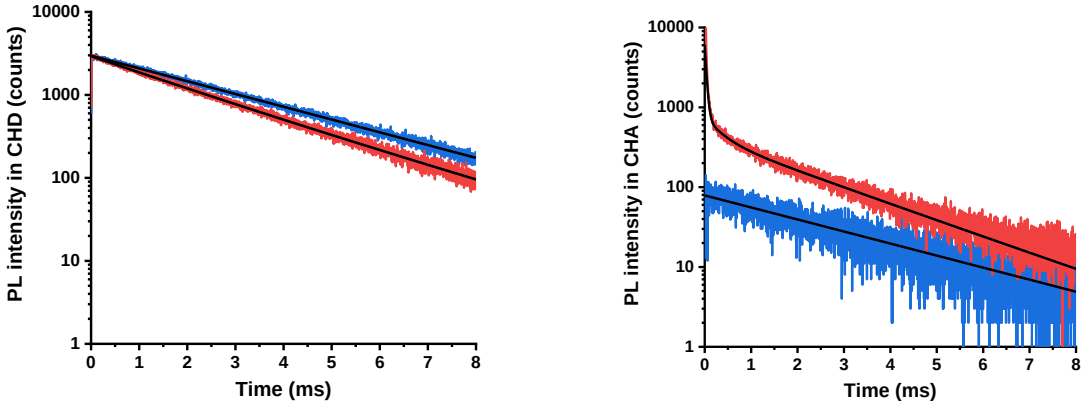

Figure 4.6. PL decay curves of Tb donor (**left**) and QD625 acceptor (**right**) used for PL decay time fitting and distance calculation in the Tb-QD FRET probe3, where there are 14 nt (plus peptide) between Tb and QD. Concentrations of Tb and QD are 10 nM and 0.5 nM, respectively. Blue and red curves are for Tb alone, and FRET probe3 respectively, and black lines represent the fit results from below.

Fitting results (all decay times in μs) of decay curve of Tb-QD probe3 in CHD (2-exponential fit with a contribution of Tb at a constant PL decay time of 2769 μs, which was fixed, whereas all other fit parameters were variable):

τ_D	A_D	τ_{DA1}	A_{DA1}	τ_{DA2}	A_{DA2}	$<\tau_{DA}>$	E_{FRET}
2769	2423	–	–	–	–	–	–
2769	752	–	–	1882	827	1880	0.32
R_0 = 10.3 nm				distance R (nm)		11.6	11.6

Fitting results (all decay times in μs) of decay curve of Tb-QD probe1 in CHA (4-exponential fit with a contribution of Tb at a constant PL decay time of 2781 μs, which was fixed, whereas all other fit parameters were variable):

τ_D	A_D	τ_{AD1}	A_{AD1}	τ_{AD2}	A_{AD2}	τ_{AD3}	A_{AD3}	$<\tau_{AD}>$	E_{FRET}
2781	514	QD background		D in the absence of A (mono-exponential)					
2781	160	20	17525	–	–	1879	2262	1856	0.33
R_0 = 10.3 nm						distance R (nm)		11.5	11.5

Time-resolved PL curves of Tb-QD625 FRET probes clearly showed different decay times caused by the different Tb-QD625 distances (**Figure 4.3**). Owing to the shorter distance (7.4 nm), probe1 (0 nt) shows significantly faster decays of FRET-quenched donor (τ_{DA1}≈110 μs, τ_{DA2}≈540 μs, average τ_{DA2}≈360 μs) and higher E_{FRET} (E_{FRET}≈0.86). Comparably, due to the longer distance (8.5 nm), probe2 (10 nt) shows slower decays of quenched donor (τ_{DA1}≈160 μs,

τ_{DA2}≈1000 µs, average τ_{DA2}≈700 µs) and lower E_{FRET} (E_{FRET}≈0.75). Probe3 (14 nt) provides the longest distance (11.6 nm), and exhibits the slowest decay of quenched donor (τ_{DA}≈1900 µs) and lowest E_{FRET} (E_{FRET}≈0.32). Concerning that the QD625 has a radius of ~4.6 nm, (core-shell diameter of ~9.2 nm) [150], so the distance of the 7.4 nm for Tb-QD (0 nt) is also contributed by the amino acid sequence in the peptide-DNA linker, which is composed of a His_6 tag appended to 10 additional amino acids (SLGAAAGSGC) and a succinimidyl 4-(N-maleimidomethyl)cyclohexane-1-carbonate (SMCC) heterobifunctional cross-linker (see **Figure 4.7A** for chemical structure). The peptide fragment and SMCC linker also ensure that the DNA part is beyond the thin QD625 surface ligands coating (compact zwitterionic ligands CL4 as shown in **Figure 4.7B**) [100], such that the conformational change of the DNA strands remains free and flexible [108], [176]. Comparing the calculated *R* between 0 nt, 10 nt, and 14 nt leads to a distance increase of ~0.11 nm ssDNA nt and ~0.3 nm per ds nt, which is in good agreement with our previous study [150]. More important than the exact distances are the distinguishable PL decay curves (PL lifetimes) because they determine the multiplexing capability.

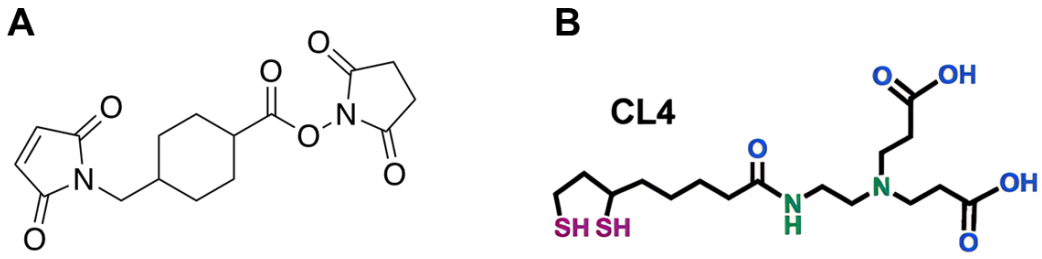

Figure 4.7. (A) Chemical structure of the SMCC heterobifunctional cross linker (MW: 334.42. Spacer Arm: 0.83 nm) that was used to connect the peptide with the DNA. **(B)** Chemical structures of the DHLA-based ligands on QD625.

4.3.4 The principle of temporal triplexing of ssDNA

The principle of the temporal triplexing of ssDNA based on TG measurement of tunable Tb-QD FRET probes is shown in **Figure 4.8**. Three Tb-QD FRET probes with distinct PL decay curves are labeled with three specific peptide-cDNAs which contain part of complementary sequences of corresponding DNA targets. The left part of the complementary sequences was modified with biotin and conjugated with streptavidin-MBs to form three MB-cDNA capture probes through biotin-streptavidin binding reactions. In the presence of target DNA,

corresponding Tb-QD FRET probe and MB probe can both partially hybridize to the target DNA, leading to the formation of Tb-QD-DNA-MB complexes (**Figure 4.8 left**). After magnetic separation and resuspension, free Tb-QD probes are removed and the TG PL measurement of target-induced Tb-QD-DNA-MB complexes from three time windows (W1, W2, and W3) can be used for the quantification of DNA targets (**Figure 4.8 right**).

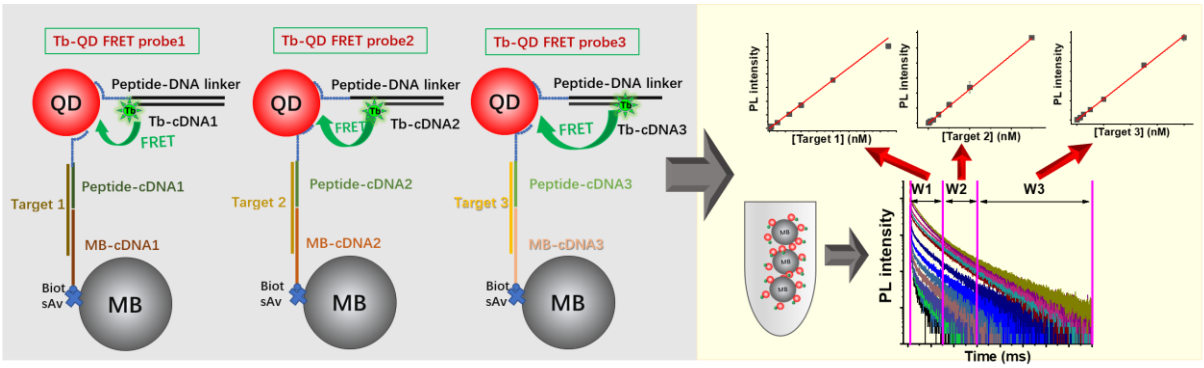

Figure 4.8. Schematic representation for temporal triplexing of DNAs based on Tb-QD FRET. **(Left)** In the presence of target DNAs, peptide-cDNA of Tb-to-QD FRET probes and cDNA on MBs will hybridize with target DNA to form the Tb-QD-DNA-MB complexes. **(Right)** After magnetic separation and resuspension, TG PL measurement from three time windows (W1, W2, and W3) of Tb-QD probes on MBs can realize the specific quantification of DNA targets.

4.3.5 Calibration of single DNA sensing assays

According to **Section 4.2.6**, three different Tb-QD probes were used to quantify three different DNA targets, respectively. As shown in **Figure 4.9 (top)**, PL intensities of FRET-sensitized QD625 are increasing with the concentration of target DNA increasing in each single sensing assay. **Figure 4.9 (bottom)** shows the PL intensity of each probe in CHA (integral intensity from 0.1 to 8 ms) as a function of target DNA concentrations. The linear dynamic range for target 1, 2, and 3 sensing are 0.625 pM to 0.375 nM, 2.5 pM to 0.5 nM, and 6.25 pM to 2nM, and the limits of detection (LOD) are 0.56 pM, 0.94 pM, and 10.3 pM, respectively (LOD = 3.3σ/slope; slope value is from the linear fitting of the calibration curve and σ is the standard deviation calculated from 10 blank samples). These sensitivities allow us to distinguish concentration differences of a few pM over the entire dynamic concentration range.

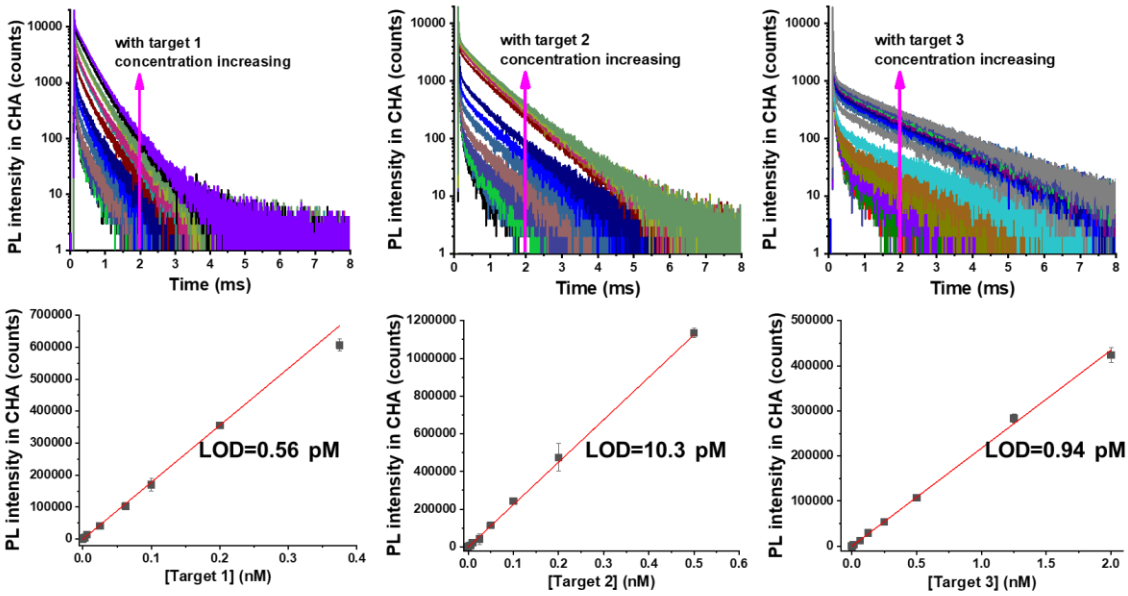

Figure 4.9. (top) PL decay curves of QD625 acceptor used in the single DNA target sensing (graphs from left to right present the sensing of targets 1, 2, and 3, respectively). With the increasing target concentrations, the PL intensity is increasing in each single assay. **(Bottom)** Calibration curves (graphs from left to right present the sensing of targets 1, 2, and 3, respectively) showed a linearly increasing PL intensities (intensity integrated from 0.1-8ms from the PL decay curves at top) over target concentration with LODs of 0.56 pM target 1, 0.94 pM target 2, and 10.3 pM target 3, respectively. Error bars present standard deviations from 10 measurements for blank samples ([target] = 0) and 3 measurements for all other concentrations.

4.3.6 Calibration of DNA triplexing assay

To realize the triplexing, three distinct time-gated detection windows (W1: 0.1-1.5 ms; W2: 1.5-3.0 ms; W3: 3.0-8.0 ms) were selected to measure different FRET-sensitized QD625 PL intensities. As shown in **Figure 4.10**, the increasing concentration of targets 1, 2, and 3 in single sensing assays induce increasing PL intensities of QD probes. Due to the different decay times, the three probes show different intensity levels in distinct time windows. Since probe1 (0 nt) has fast decay (resulting from the shortest donor-acceptor distance and most efficient FRET), it exhibits the highest contribution in window 1. Due to the slower and slowest decay of probe2 (10 nt) and probe3 (14 nt), they contribute more to window 2 and window 3, respectively.

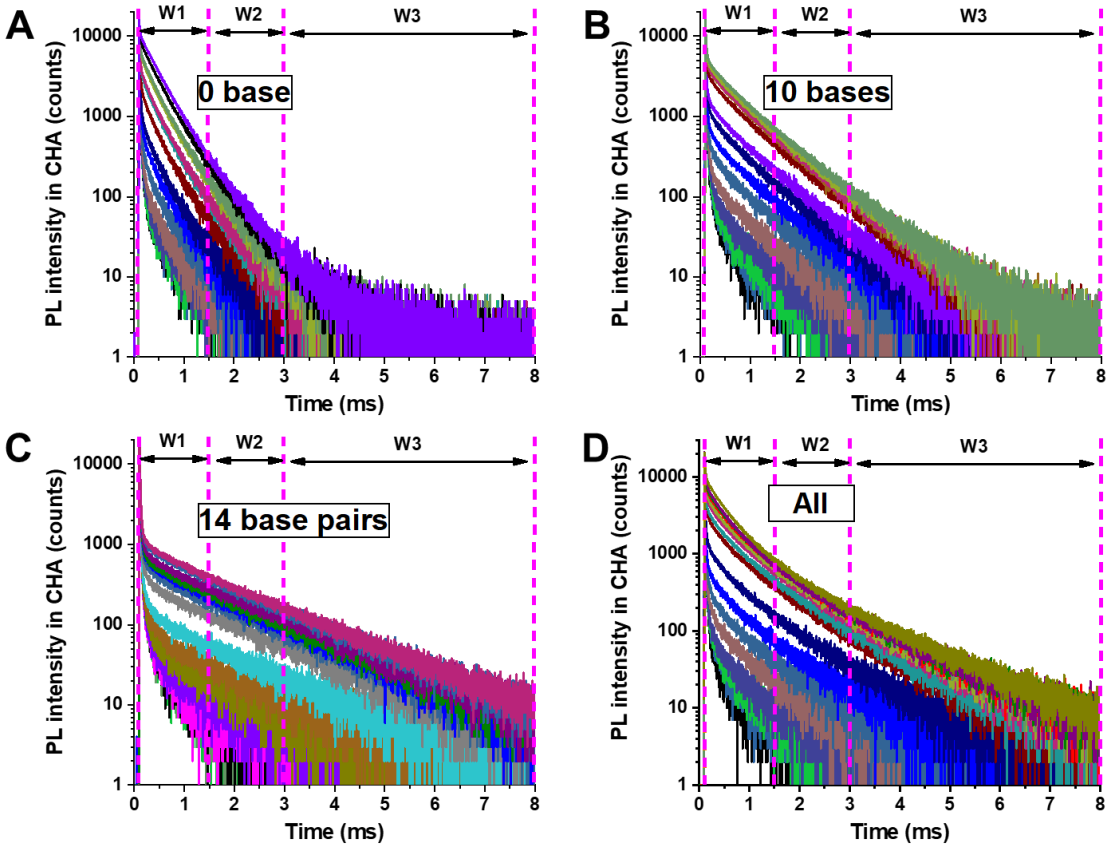

Figure 4.10. FRET-sensitized PL decay curves of QD625 from Tb-QD625 probes used for single and triplexed DNA sensing with increasing concentrations of targets and constant concentrations of Tb-QD625 probes (probes 1, 2, and 3 are all at 0.1 nM). **(A)** single sensing of target1: 625 fM to 8nM; **(B)** single sensing of target2: 2.5 pM to 16nM; **(C)** single sensing of target3: 6.25 pM to 40nM; **(D)** Target 1, 2, 3 triplexing (concentrations of each target are the same as used in single sensing).

For a triplexed detection, it is important that PL intensities increase linearly with increasing target concentration in all detection windows because that makes the calculation of temporal crosstalk (the contributions of each of the three decay curves to the three different detection windows) most simple. In addition, when the sum of the TG PL intensities from single target assays is equal to the TG PL intensities of the assay in which all three targets are present, the calibration curves of triplexing can be easily solved by linear fits. As shown in **Figure 4.11**, our system fulfills these requirements quite well. The three time windows show excellent agreement between the mathematical sum of the intensities from each single target and the intensity from all targets until target concentrations of circa 600 pM. At higher concentrations, the triplexed signal is slightly lower than the sum of the signals. This “earlier” signal saturation can most

probably be corrected by selecting higher probe concentrations. However, that would also lead to higher LODs because of increasing background signals. Because our aim was the quantification of low target concentrations, we were very satisfied with the current performance and did not apply any optimization toward higher target concentrations in the current study. The slopes of the 9 different liner calibration curves from three single sensing assays in the three windows were used as the S-values in the 3x3 matrix in **Equation 4.4**.

$$\begin{bmatrix} I^{W1} \\ I^{W2} \\ I^{W3} \end{bmatrix} = \begin{bmatrix} c_1 \\ c_2 \\ c_3 \end{bmatrix} \begin{bmatrix} S_{W1}^{T1} & S_{W1}^{T2} & S_{W1}^{T3} \\ S_{W2}^{T1} & S_{W2}^{T2} & S_{W2}^{T3} \\ S_{W3}^{T1} & S_{W3}^{T2} & S_{W3}^{T3} \end{bmatrix} \tag{4.4}$$

In this simple linear equation, I^{W1}, I^{W1}, and I^{W1} are the PL intensities measured in the three TG detection windows for the multiplexed assay, and S_{W1}^{T1}, S_{W1}^{T2}, S_{W1}^{T3}, S_{W2}^{T1}, S_{W2}^{T2}, S_{W2}^{T3}, S_{W3}^{T1}, S_{W3}^{T2}, S_{W3}^{T3} are the slopes of the calibration curves (I over concentration) of each single targets (T1, 2, and 3 represent target 1, 2 and 3) sensing in the three detection windows (W1, 2, and 3). Therefore, I^{W1}, I^{W2}, and I^{W3} are available from PL measurement and S_{W1}^{T1}, S_{W1}^{T2}, S_{W1}^{T3}, S_{W2}^{T1}, S_{W2}^{T2}, S_{W2}^{T3}, S_{W3}^{T1}, S_{W3}^{T2}, S_{W3}^{T3} are known values (from the calibration curves). Then, **Equation 4.4** can be solved for the unknown target concentrations (c_1, c_2, and c_3 represent the concentrations of target 1, 2 and 3) by numerical inversion of the 3 × 3 matrix. **Figure 4.12** shows the successful application of this temporal multiplexing concept for selective, sensitive, and accurate recovery of the three different DNAs at varying low picomolar to nanomolar concentrations from eleven different samples. This proof-of-concept demonstration should be transferable to real-life nucleic acid biomarkers, which was out of the scope of the current study.

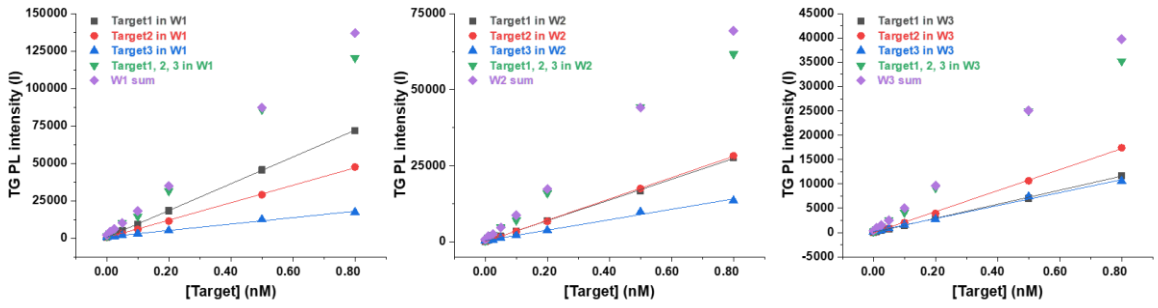

Figure 4.11. TG PL intensities in the three detection windows (left: window 1; middle: window 2; right: window 3) as a function of target DNA concentrations. Black curves are for target 1. The red curves are for target 2, and the blue curves are for target 3. The green and purple points are the intensity from triplexing (three targets all present) and the simple sum of single sensing. The slopes of the linear fits of

each target DNA in each window provide the *S*-values for **Equation 4.4**.

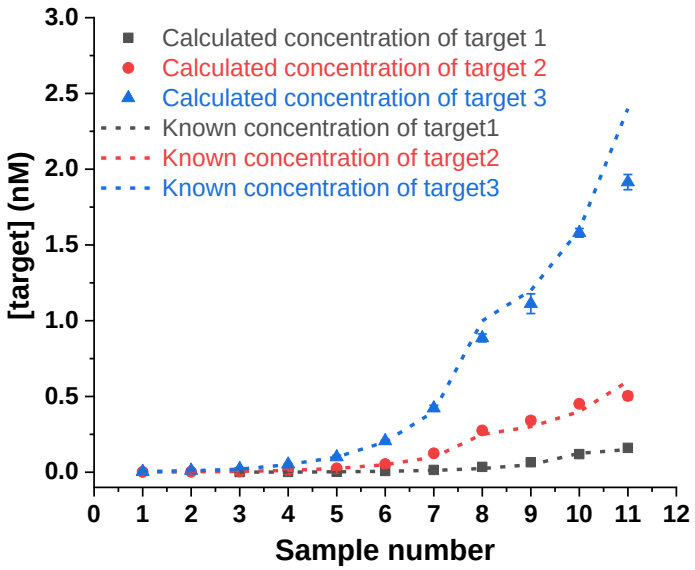

Figure 4.12. Recovery of varying low concentrations of targets 1, 2, and 3 from 11 different samples using temporal triplexing assay. Dotted lines represent known concentrations; data points represent the calculated concentrations from the triplexing assay. Error bars are from three repeats of each sample.

4.4 Conclusions

In this chapter, a single Tb-QD FRET pair-based multiplexing strategy was developed by designing Tb-to-QD FRET PL probes with temporally distinguishable PL decays tuned by the length of Tb-DNA on QD surface. The proposed method was successfully used for the quantification of different DNA targets at low picomolar concentrations from mixed samples with a single measurement. The temporal multiplexing does not need lifetime analysis but can be realized by a simple time-gated measurement of PL intensity from different time windows. The introduction of magnetic beads-based separation and TG measurements removed all the luminescent background from free probes and auto-fluorescence background from the sample matrix, resulting in very high sensitivity and accuracy. This work revealed the versatile and powerful diagnostic performance of TG-FRET and the high distance sensitivity of FRET shows the new possibility to design distinct PL probes without introducing more materials. Furthermore, temporal TG-FRET multiplexing can be combined with spectral, spatial, and intensity resolutions, paving the way for unprecedented multiplexing capabilities.

CHAPTER 5

QD-based FRET assays for temperature/DNA dual sensing

5. QD-based FRET assays for temperature/DNA dual sensing

5.1 Introduction

The development of analytical techniques for probing biomolecular interactions and detecting specific analytes in biological environments has shown increasing importance for life science, which emphasizes the request for more powerful and sensitive analytical devices and methods exhibiting high specificity and affinity for important biomolecules and components such as proteins, peptides, or nucleic acids. Optical biosensors are highly advantageous tools due to their ease of operation, rapid response, high sensitivity, and capability of multiplexing [177], [178]. Förster Resonance Energy Transfer (FRET), as a non-radiative energy transfer process between two fluorophores, is highly dependent on the proximity of the two entities (ca. 1-10 nm), which makes it an ideal choice for probing nanoscale biomolecular interactions [179], [180].

Quantum dots (QDs) are one of the most favorable luminescent materials to be applied to FRET as both donors or acceptors due to their superior photophysical properties to conventional fluorophores, including strong and broad absorption, high brightness, chemo- and photo-stability, color-tunable emissions via adjusting their size and component materials, and large surface for biomodifications. By now QD-based FRET has been used as a well-established technique in various bioanalytical application, such as biomolecular structural analysis, medical diagnostic, as well as bioimaging in cells and tissues [181], [182]. However, the abovementioned applications were performed at either room temperature or 37℃, and only a few studies have investigated the temperature effect on QD-based FRET systems [183], [184]. Since it has been reported that there are thermally activated changes in the photoluminescence (PL) of the QDs [185]–[188], it is interesting to investigate the temperature effects on the QD-based FRET assays, which is important for the sensitivity, stability, and repeatability sensing of both temperature and biological targets. Therefore, the study focusing on the temperature responses of QDs luminescence and QD-based FRET is of practical importance in the development of biosensors, where different storage and/or application temperatures need to be considered.

In this work, the temperature response of widely used water-soluble CdSe/ZnS QDs (core–shell QDs, functionalized with dihydrolipoic acid (DHLA)-based compact ligands) emitting at 625 nm was analyzed by measuring their absorption and PL emission spectra under different temperatures. By using the QDs as both the nanoplatforms and FRET donors or acceptors, two prototypical FRET-based biosensing assays were developed as shown in **Figure 5.1**. In the two FRET systems, peptide-DNA is attached to the QD surface through metal-polyhistidine coordination. Cyanine 5 (Cy5) or Lumi4-Tb-NHS (Tb) labeled DNAs could specifically hybridize to the complementary DNA sequence in the peptide-DNA, such that QD-peptide-dsDNA-Cy5/Tb FRET complexes were formed. The temperature response of QDs and its effect on the biosensing performances of the two assays were investigated by combining steady-state and time-resolved PL measurements of the QD-based FRET signals. Despite thermal quenching of QD, Cy5, and Tb PL, the ratiometric FRET assay format can eliminate the temperature dependence and retain effective sensing of peptide-DNA. The PL intensities measured from the acceptor or donor channel of QD, Cy5, or Tb alone, as well as QD-to-Cy5 or Tb-to-QD FRET systems with fixed concentration of peptide-DNA show temperature sensitivity, which can be used for the temperature sensing. Combining the ratiometric FRET format with PL intensity recording at various temperatures, the target/temperature dual sensing can be achieved.

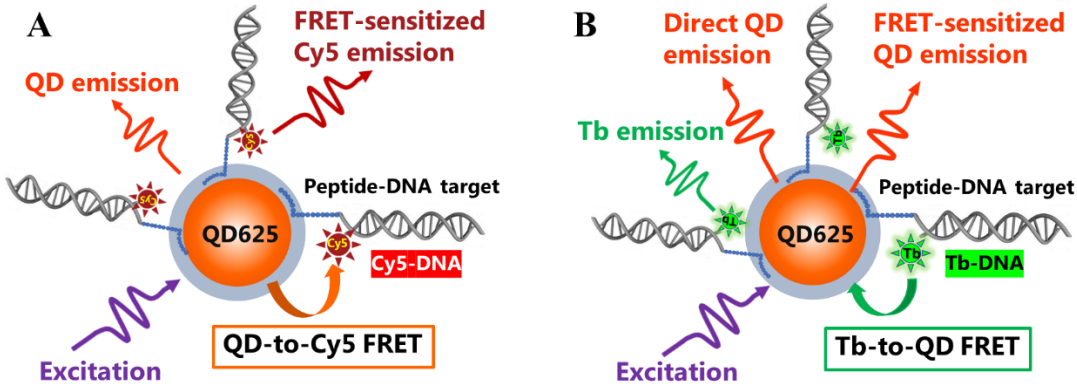

Figure 5.1. Principles of QD-based FRET. **(A)** Cy5-labeled DNA hybridizes to peptide-DNA attached to the QD625 surface, which leads to QD-to-Cy5 FRET. **(B)** In a similar design Tb-DNA hybridization to the peptide-DNA results in Tb-to-QD FRET.

5.2 Materials and methods

5.2.1 Materials

Lumi4-Tb-NHS (Tb) was provided by Lumiphore Inc. (Berkeley, CA, USA). CdSe/ZnS QDs emitting at 625 nm (QD625) were provided by Invitrogen by Life Technologies (Carlsbad, CA) and functionalized with DHLA-based compact ligands in-house. Peptide-oligonucleotides were synthesized by Biosynthesis (Lewisville, Texas, USA). All the other modified oligonucleotides were synthesized and purified with HPLC by Eurogentec (Liège, Belgium). The sequences and modifications of all the nucleic acids used in this study are listed in **Table 5.1**. Tris(hydroxymethyl)-aminomethane, bovine serum albumin, HEPES, and NaCl were purchased from Sigma-Aldrich (St. Louis, MO, USA). All chemicals were used as received. Water was purified by MAXIMA (USF Elga, UK). Zeba Spin Desalting Columns (7 kDa MWCO) were purchased from Thermo Fisher Scientific (Illkirch-Graffenstaden, France).

Tb-DNA conjugate was prepared according to the same procedure in **Section 4.2.2**: Lumi4-Tb-NHS (at an excess concentration) was mixed with amino-functionalized oligonucleotide in 100 mM carbonate buffer at pH 9.0 and incubated overnight at 4 °C. Then the conjugate was purified 3 times with HEPES buffer (100 mM, pH 7.4) by Zeba Spin Desalting Columns (7 kDa MWCO). The conjugation ratio was determined to be higher than 0.9 Tb/DNA by a linear combination of the respective absorbance values of Tb (ca. 340 nm using a molar absorptivity of ca. 26,000 M^{-1} cm^{-1}) and DNA (at ca. 260 nm) within the conjugate.

Table 5.1. Sequences and modifications of peptide-DNA target and DNA probes.

Name	Sequence (5'-3')	Modification
Peptide-DNA	TAGCTCGACAAAGTGCTCATAGTGCAGGTAG	5'-H6SLGAAAGSGC-SMCC-amino
Tb-DNA	CTACCTGCACTATGAGCACTTTGTCGAGCTA	3'-C6-NH_2
Cy5-DNA	CTACCTGCACTATGAGCACTTTGTCGAGCTA	3'-Cy5

5.2.2 Optical characterization

Absorption spectra (Cary 60 UV-Vis Spectrophotometer, Agilent) and emission spectra (Fluorolog-3, HORIBA) for QDs, and Tb and Cy5 functionalized with DNA were recorded in TRIS-Cl buffer (20 mM, pH 8.0). All the spectra are shown in **Figure 5.1**. According to FRET theory, it can be defined as an energy transfer process via dipole-dipole interaction between oscillating donor and acceptor in proximity (ca. 1-10 nm) [23], [175], [189]. So, FRET needs the energetic resonance between donor and acceptor, as expressed by the spectral overlap integral between donor emission and acceptor absorption:

$$J = \int \bar{I}_D(\lambda)\varepsilon_A(\lambda)\lambda^4 \, d\lambda \tag{5.1}$$

where $\bar{I}_D$ is the area-normalized (to unity) PL spectrum of donor, and $\varepsilon_A(\lambda)$ is the molar absorption of acceptor (**Figure 5.2**). Distance (R), orientation (κ^2), and energetic resonance (J) in combination with PL parameters of the donor (PL quantum yield (Φ_D) and PL lifetime (τ_D)), the refractive index of the surrounding medium (n), and Avogadro's number (N_{AV}) are used to define the FRET rate:

$$k_{FRET} = \frac{9(ln\,10)\kappa^2\Phi_D}{128\pi^5 N_{Av} n^4 \tau_D R^6} J \tag{5.2}$$

Förster distance R_0 (the donor-acceptor distance for which FRET is 50% efficient) was calculated by using **Equation 5.3**.

$$R_0 = 0.02108(\kappa^2 \Phi_D n^{-4} J(\lambda))^{\frac{1}{6}} \text{ (in nm)} \tag{5.3}$$

The orientation factor of κ^2 was taken as 2/3 due to dynamic averaging as found for other Tb-QD or Tb-Cy dye donor-acceptor systems [23]. The refractive index n of the aqueous solution was taken as 1.35. Φ_D represents the quantum yield of FRET donors, measured as 0.41 ± 0.01 and 0.80 ± 0.05 for QD625 and Tb respectively. Förster distance R_0 of the FRET pairs was calculated as R_0(QD625/Cy5) = 7.9 ± 0.4 nm and R_0(Tb/QD625) = 10.3 ± 0.5 nm.

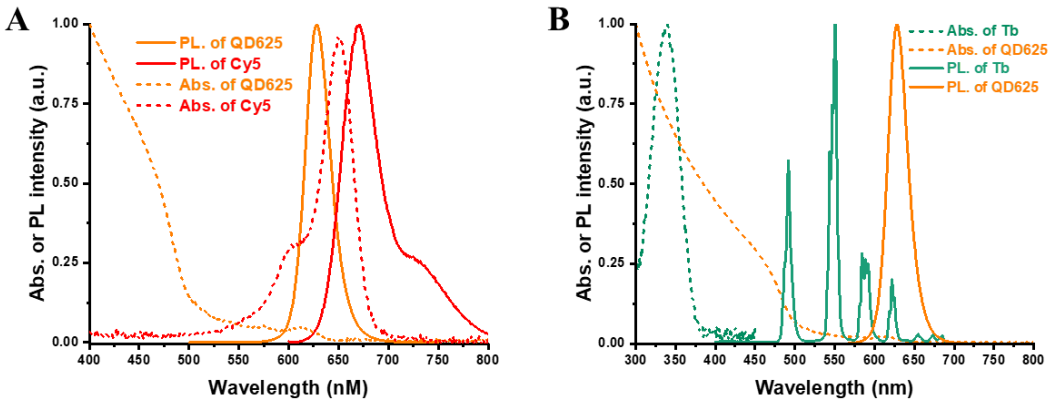

Figure 5.2. Absorption and emission spectra of the FRET pairs. **(A)** QD-to-Cy5 FRET pair: spectra of QD625 emission and absorption (orange solid line and orange dotted line), Cy5 emission (red solid line), and absorption (red dotted line) that partly overlaps with the emission of QD625. **(B)** Tb-to-QD FRET pair: emission (green solid line) and absorption (green dotted line) spectra of Tb (green), emission (orange solid line), and absorption (orange dotted line) spectra of QD625 that partly overlaps with Tb emission.

5.2.3 Temperature-dependent absorption and PL spectra of QDs

For temperature-dependent absorption and PL measurements, the water-soluble QDs were diluted to 3 nM with TRIS-Cl buffer (pH 8.0) and transferred into quartz cuvettes. Absorption spectra at different temperatures were measured by a Cary 5000 UV-Vis-NIR spectrophotometer with a Peltier-based temperature control. PL spectra at different temperatures were measured under excitation at 405 nm by a FluoTime 300 fluorescence spectrometer (PicoQuant) equipped with a Xenon arc lamp and an external thermostat for temperature control of the cuvette holder. At each temperature, the PL measurements were made after at least 15 min of thermal equilibration.

5.2.4 QD-based temperature/peptide-DNA duplexed FRET assays

FRET assays were prepared in DNA hybridization buffer (20 mM Tris-Cl, 500 mM NaCl, 0.1% BSA, pH 8.0). In each sample, 50 µL QD625 (0.5 nM in the final 150 µL mixture) was mixed with 50 µL Tb-DNA or Cy5-DNA (both at 10 nM in the final 150 µL mixture), to which 50 µL of peptide-DNA at different concentrations (from 0 nM to 10 nM in the final 150 µL mixture) was added. All samples were prepared three times and incubated for 2 h at room temperature (25°C). After incubation, the samples were transferred into black 96-well

microtiter plates and measured by a Tecan SPARK plate reader (Spark, TECAN, Switzerland) under different temperatures. For the QD-to-Cy5 FRET assay, the steady-state PL spectra and intensity were measured by exciting the samples at 405±10 nm, and collecting the signal of the QD625 donor and Cy5 acceptor at 625±5 nm and 668±5 nm, respectively. For the Tb-to-QD FRET system, the TG PL emission spectra and intensity measurements were under the excitation of 337±10 nm, and emission at 494±5 nm and 640±10 nm were measured for Tb and QD625, respectively. TG measurement was performed with a lag time of 100 μs and an integration time of 1500 μs. FRET ratio was used as the detection signal of DNA hybridization assays, which is calculated by **Equation 5.4**. Calibration curves show the increasing FRET ratios with increasing concentrations of peptide-DNA.

$$FRET\ ratio = \frac{I_A}{I_D} \tag{5.4}$$

Here I_A and I_D present the respective PL intensity of acceptor (A) and donor (D) in the FRET assays.

5.3 Results and discussion

5.3.1 Temperature sensitivity of the water-soluble CdSe/ZnS QDs

Firstly, the spectral measurements of water-soluble CdSe/ZnS QD625 in TRIS buffer were performed when the temperature changed from 10 to 80°C as shown in **Figure 5.3**. The absorption spectra show few features (exciton peaks around 620 and 560 nm are still well visible) suggesting that the QDs in this sample are of various diameters and may also be agglomerated into small clusters. With the temperature increasing from 10 to 50°C, the absorption spectra did not significantly change (**Figure 5.3 A)**. However, when the QDs were heated from 60 to 80°C, there was an increase in the extinction and the spectra shape became more featureless, which was probably caused by the formation of additional QD aggregates whose sizes were sufficient to significantly scatter the incident light. It has been reported that the aggregation of colloidal QDs is most often related to the disturbance in surface charges and thus depends on the nature and structure of surface ligands [94], [108], [190]. In our case, the DHLA-anchored carboxylic-acid-terminated ligands might show desorption of thiolate ligand

from the QD surface and the acidic groups' protonation at high temperatures, thus leading to the aggregation of QDs [94], [100]. Whereas the redshift with increasing temperature is not very obvious in the broad absorption spectra, it can clearly be observed in the PL spectra (**Figure 5.3 B**). This shift was most probably caused by increasing exciton carrier transfer between the QDs at higher temperatures and the thermal activation of emission from lower energy trap states [186], [188], [191].

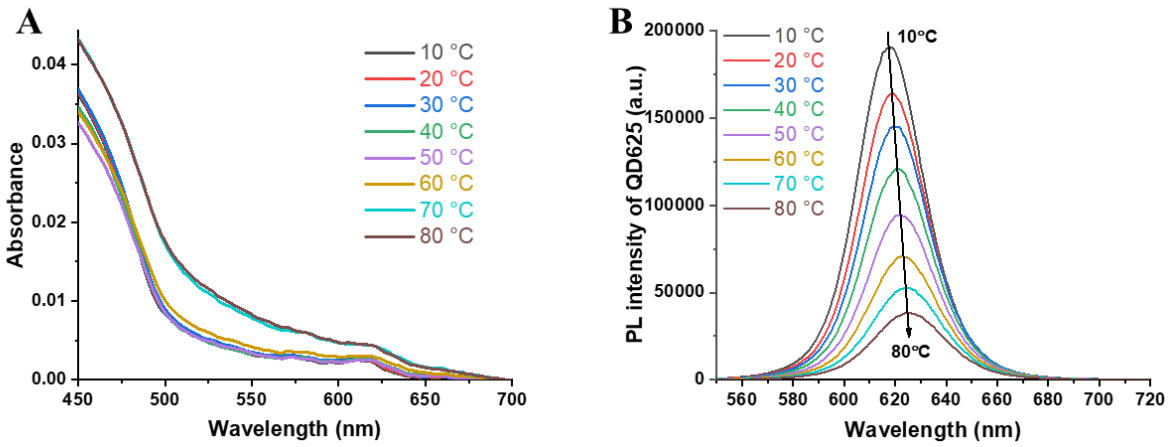

Figure 5.3. Spectra of temperature-dependent water-soluble CdSe/ZnS QDs. **(A)** Absorption spectra at indicated temperatures. **(B)** PL spectra at indicated temperatures.

The strong temperature dependence of the QD PL intensity was measured in different heating processes and is depicted in **Figure 5.4**. The results show that PL quenching of QDs at 80 °C recovered well after cooling down to 25°C in five heating-cooling cycles between these two temperature points (**Figure 5.4A**). After continuous heating from 10°C to 80°C, QD PL could only partly recover when cooled back to 10°C (**Figure 5.4B**). This partly irreversible quenching was probably caused by the QD surface oxidation, as well as aggregation and precipitation-induced quenching at high temperatures [185], [187]. Despite the partly irreversible quenching, relative quenching of QD PL intensity was found to be the same for all heating cycles (**Figure 5.4C**), which makes the PL intensity change applicable to temperature sensing. The relative PL intensity change over temperature was found to be -1.21±0.02% per °C (**Figure 5.4D**).

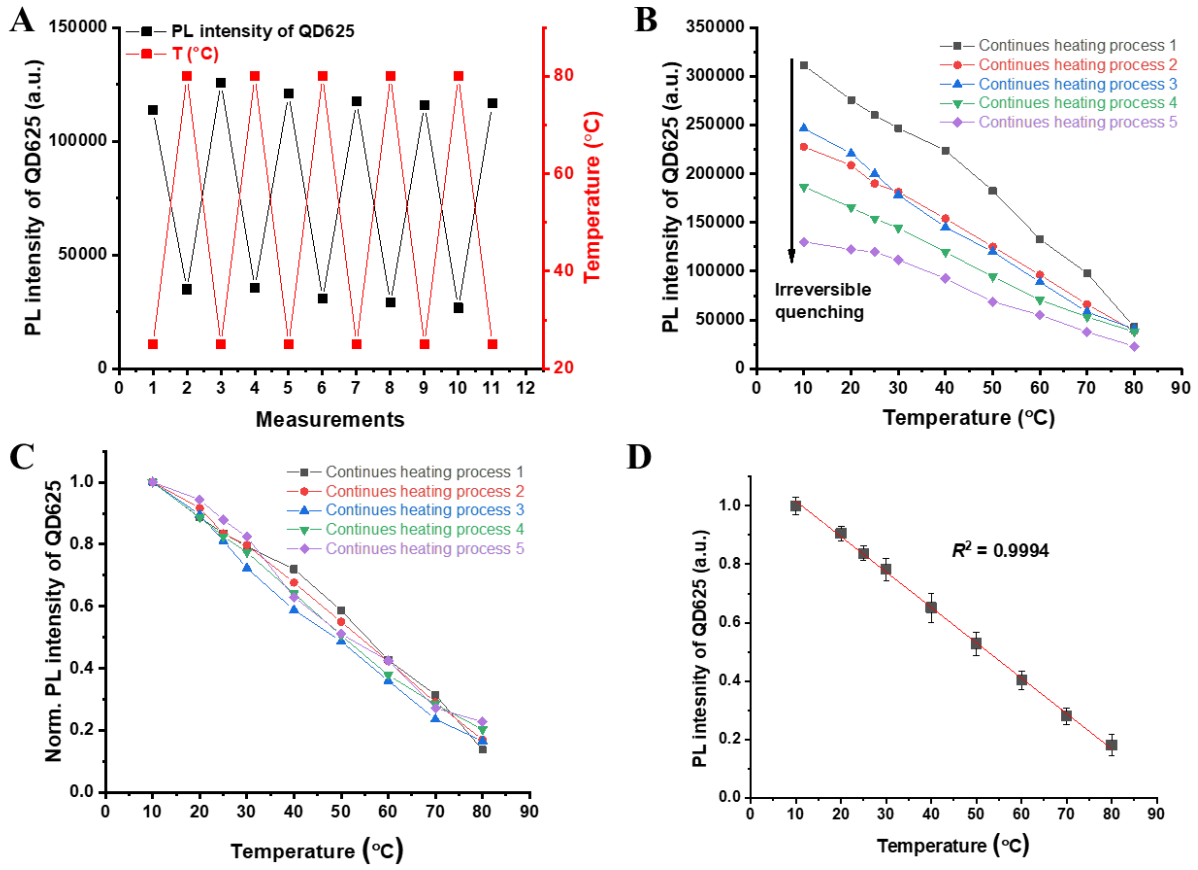

Figure 5.4. The effects of increasing temperature on water-soluble CdSe/ZnS QDs. **(A)** PL intensity of QDs in five cycles of heating and cooling between 25 °C and 80 °C. **(B)** PL intensity of QDs in five continuous heating and cooling cycles from 10 °C to 80 °C. **(C)** Normalized PL intensity of QDs in five continuous heating and cooling cycles. **(D)** Variation in normalized PL intensity of QDs with temperature in the range of 10°C to 80°C.

5.3.2 Temperature-dependent DNA sensing using the QD-Cy5 FRET assay

Investigating the temperature-dependent quenching behavior of QDs is not only relevant for developing temperature sensors. It is also of practical importance for evaluating their performance in biosensing and bioimaging applications that are usually performed at various different temperatures between ~20 °C and ~40 °C. Here, we scrutinized two representative FRET biosensing systems, in which QDs were used as FRET donors and acceptors, respectively.

The QD-to-Cy5 FRET system (**Figure 5.1A**) consisted of a QD625 donor probe and a Cy5-DNA acceptor probe, which are separated beyond FRET distances when freely floating in solution. The addition of a prototypical DNA target, which consisted of a 31 nt DNA sequence

appended by a hexa histidine (His_6)-containing peptide (cf. **Table 5.1**) for self-assembly to the QD surface, resulted in Cy5-DNA-DNA-peptide hybridization and the formation of QD-peptide-dsDNA-Cy5 complexes, in which QD donor and Cy5 acceptor were sufficiently close for FRET when excited at 405 nm (primarily QD625 excitation). We selected the peptide-DNA (and not the Cy5-DNA) as a prototypical target because of three main reasons. First, our second FRET system (vide infra) used Tb-DNA as the donor probe and QD625 as the acceptor probe. Thus, using exactly the same peptide-DNA as the target (instead of Cy5-DNA and Tb-DNA) provided a better comparison. Second, we wanted to use a purely biological target without a directly labeled fluorescent probe. Third, we wanted to evaluate if peptide-DNA and QD can be added separately and if His_6-QD attachment would be functional in parallel to DNA-DNA hybridization. Such a separation would be highly beneficial for storage and assay kit preparation because the QD would be an independent component without prior bioconjugation. We acknowledge that our prototypical FRET system is not an actual hybridization assay for quantifying independent (label-free) targets. However, for evaluation purposes and optimization, such prototypical FRET systems provide ideal platforms that can be easily translated into actual target detection (e.g., microRNA) [19] once a clinically relevant target is identified.

As expected, increasing concentrations of peptide-DNA resulted in decreasing QD and increasing Cy5 PL intensities due to QD-to-Cy5 FRET (**Figure 5.5**). Thus, we transferred the QD-to-Cy5 FRET assay to an endpoint measurement with the benchtop fluorescence plate reader, to validate the temperature dependence of the QD PL and the Cy5/QD PL ratio (FRET-ratio, **Equation 5.4**). Despite a relatively narrow temperature range of ~15 °C, the QD PL intensities showed a clear temperature dependence (increased PL quenching with increasing temperature) for all target concentrations (**Figure 5.6A**). Whereas both increasing temperatures and increasing target concentrations resulted in QD donor PL quenching, the Cy5 acceptor PL intensity increased with increasing target concentration but decreased with increasing temperatures (**Figure 5.6B**). The Cy5 PL intensity without target was not temperature dependent because there was no FRET sensitization from QDs and PL from directly excited Cy5 or QD at 665 nm was negligible. Thus, the signal was mainly composed of background. The FRET-ratio profited from approximately the same temperature dependence of the QD

donor and Cy5 acceptor PL and removed almost completely the temperature dependence (**Figure 5.6C**). A typical linear increase with peptide-DNA concentration ranging from 0 to ~8 nM followed by saturation at higher concentrations was found and the assay sensitivities (slopes of the linearly increasing parts) were approximately independent of the temperature.

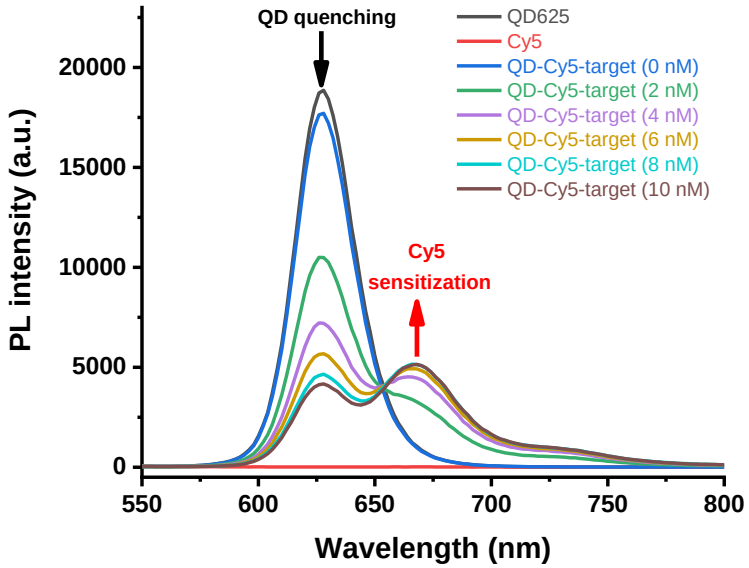

Figure 5.5. Peptide-DNA target concentration-dependent PL spectra of the QD625-Cy5 FRET sensor at 25 °C.

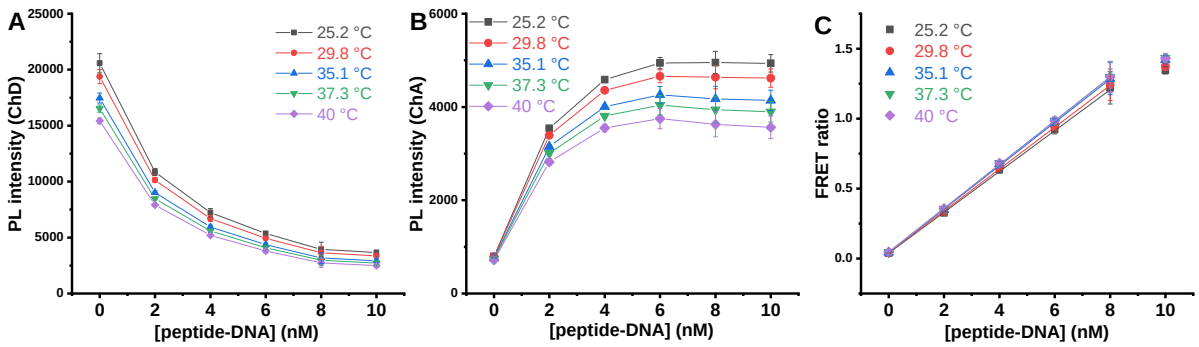

Figure 5.6. (A) Temperature and target concentration-dependent quenching of QD donor PL measured at 625±5 nm. **(B)** Temperature-dependent quenching combined with target concentration-dependent FRET sensitization of Cy5 acceptor PL measured at 668±5 nm. **(C)** The FRET-ratio assay calibration curves show strongly reduced temperature dependence and a typical linear increase with peptide-DNA concentration ranging from 0 to ~8 nM.

5.3.3 Temperature-dependent DNA sensing using the Tb-QD FRET assay

The Tb-to-QD FRET system (**Figure 5.1A**) consisted of Tb-DNA donor probes and QD625 acceptors, which are separated beyond FRET distances in the absence of target peptide-DNA. The addition of the His_6-containing peptide-DNA target (cf. **Table 5.1**), which can self-assembly to the QD surface, resulted in Tb-DNA-DNA-peptide hybridization and the formation of QD-peptide-dsDNA-Tb complexes, in which Tb donor and QD acceptor were sufficiently close for FRET to happen upon the excitation at 337 nm. Due to the exceptionally broad absorption of QDs, they are directly excited at the same time. Thus, the time-gated (TG) measurements were applied to suppress the PL emission background from QDs. As shown in **Figure 5.7**, the increasing concentration of peptide-DNA will induce the FRET-quenching of Tb and FRET-sensitization of QD. To investigate the temperature effect on this Tb-QD FRET assay, the FRET-sensitized QD PL and the QD/Tb PL ratio (FRET-ratio, **Equation 5.4**) were measured under different temperatures. As shown in **Figure 5.8A**, the PL intensity of the Tb donor is decreasing due to both FRET-quenching and increasing temperature, while the PL intensity of QD acceptor shows an increase from FRET-sensitization with increasing target concentration and thermal quenching with elevating temperature (**Figure 5.8B**). The ratiometric format of the FRET assay can eliminate the temperature dependence of Tb and QD PL intensity when we focus on the target sensing. As shown in **Figure 5.8C**, the FRET-ratio linearly increases with target concentrations increasing from 0 to 8 nM, which is in agreement with the QD-to-Cy FRET assay.

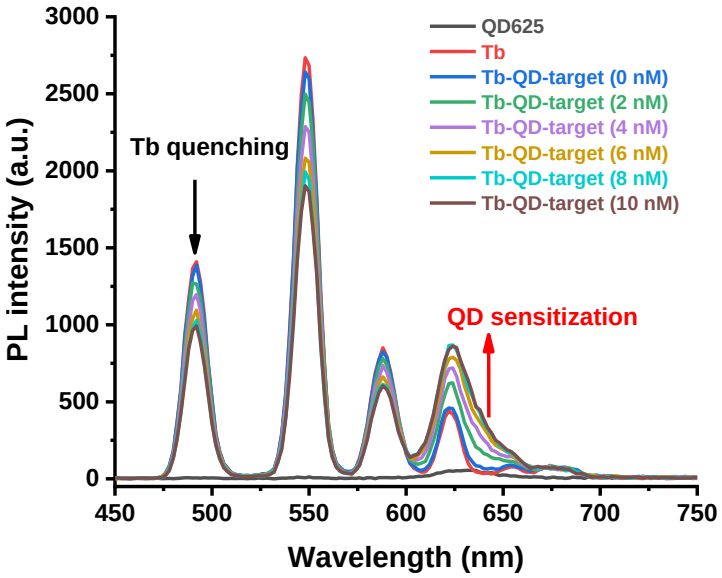

Figure 5.7. Peptide-DNA target concentration-dependent PL spectra of the Tb-QD625 FRET sensor at 25.1 °C from TG measurement with a lag time of 100 μs.

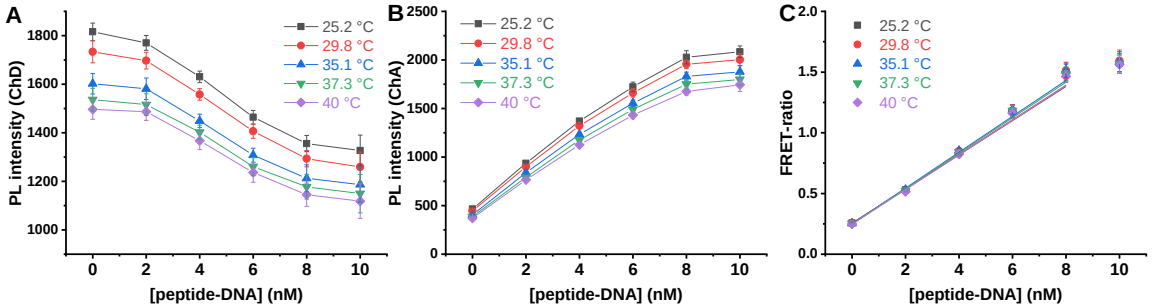

Figure 5.8. (A) Temperature and target concentration-dependent quenching of Tb donor PL measured at 494±10 nm with a time-gate of 100-1500 μs. **(B)** Temperature-dependent quenching combined with target concentration-dependent FRET sensitization of QD625 acceptor PL measured at 640±10 nm with a time-gate of 100-1500 μs. **(C)** The FRET-ratio (TG PL intensity ratio between QD625 and Tb), shows a linear increase with peptide-DNA concentration increasing, and the increasing temperature has negligible effect on it.

5.3.4 Simultaneous DNA/temperature sensing using QD-Cy5 and Tb-QD FRET assays

Considering that DNA target sensing via the FRET ratio is approximately independent of temperature but the QD PL intensity is temperature dependent, we can design a dual DNA/temperature sensor. The FRET ratios are used for target quantification (**Figures 5.6C** and

5.8C) whereas the QD PL intensities from the same experiments are used for temperature quantification (**Figure 5.9**). As shown in **Figure 5.9A**, the PL intensity of QD625 in QD-to-Cy5 FRET assay decreases both with temperature increasing and with target concentration increasing, and the relative PL intensity of QD625 in QD-Cy5 complex with fixed peptide-DNA concentration show similar temperature sensitivity as the QD625 alone, which can be used for temperature sensing (**Figure 5.9B**). In the Tb-QD FRET assay, FRET-sensitized PL intensity of QD625 (measured with a time-gate of 100-1500 μs) shows linearly quenching with increasing temperature (**Figure 5.9C**). By using the relative TG PL intensity for each Tb-QD complex with fixed peptide-DNA concentration, the QD-based temperature sensing can be realized (**Figure 5.9D**). Such dual DNA/temperature sensors realized via a single FRET probe (QD-Cy5 or Tb-QD) would be very interesting in investigating temperature-dependent biological binding inside cells or finding optimal temperatures for DNA hybridization or DNA amplification assays without the need for distinct experiments for temperature and hybridization optimization. We believe that our proof-of-concept demonstration is an important step toward such cellular probes and DNA assays and our future work will aim for the development of such dual DNA/temperature biosensors.

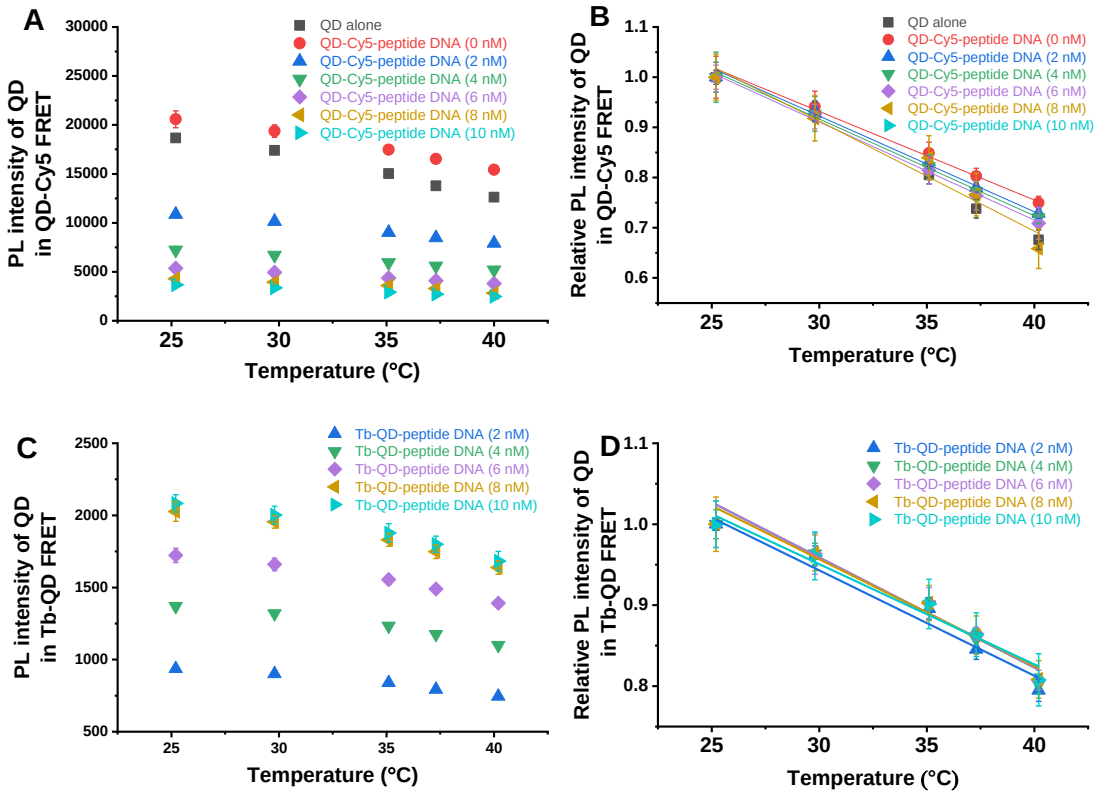

Figure 5.9. Temperature sensing by FRET assays. **(A)** The PL intensity of QD625 in QD-to-Cy5 FRET assay decreases both with temperature increasing and with target concentration increasing. **(B)** Relative PL intensity of QD625 in QD-to-Cy5 FRET assay decreases linearly with temperature increasing, the temperature sensitivity is approximately independent of target concentration. **(C)** FRET-sensitized PL intensity of QD625 in Tb-to-QD FRET (measured with a time-gate of 100-1500 μs) is quenched by increased temperature. (D) Relative TG PL intensity of FRET-sensitized QD shows a linearly decreasing with temperature increasing from 25 to 40 °C.

5.4 Conclusions and outlook

We showed that temperature significantly affected the PL intensity and stability of CdSe/ZnS-based (the exact composition is not disclosed by Thermo Fisher) core-shell QDs in aqueous solution. Results show that the PL intensity of QDs declines with the emission peak position shifting towards the red as temperature increases from 10 to 80 °C, which shows good reversibility. Continuous heating treatment induces partly irreversible PL quenching of QDs due to the surface oxidation reaction and particle precipitation and aggregation (when the temperature is over 60 °C). The temperature effect on QD-based assays can be eliminated by using a ratiometric FRET format (FRET ratio as the signal), which allows to remain efficient and temperature independent (between circa 25 and 40° C) sensing of DNA. The PL intensities of QD donors or acceptors within the same FRET assays show a temperature dependence, which can be used for simultaneous temperature sensing during DNA quantification. Our results emphasized the importance of temperature control for QD-based PL assays and that ratiometric FRET detection can remove the temperature dependence. Whereas our results are only a proof-of-concept demonstration of dual DNA/temperature sensing, we are planning to translate the concept into actual intracellular sensing and temperature-dependent hybridization analysis. We will also extend our study to other QDs (materials and sizes) to verify if the temperature dependence is a general issue and if this dependence is different for different QDs. Extension to protein-based assays (e.g., immunoassays) and combination with temperature-independent fluorophores for ratiometric temperature sensing are other routes to explore in the future.

CHAPTER 6

Summary and outlook

6. Summary and outlook

In summary, the thesis investigated three Tb-to-QD FRET-based bioassays for nano-surface biomolecular interactions probing and temperature/bio-target dual sensing. The unique photophysical properties of luminescent lanthanide-based materials and QDs provided extraordinary advantages to the developed biosensing methods. Firstly, the relatively large surface and good biocompatibility of water-soluble QDs enables the bioconjugation of various functional biomolecules (e.g., antibodies and peptide-DNA), which enables the nano-surface immunoassays (sandwich and displacement immunoassay) and DNA hybridization probing. Secondly, the long PL lifetime of Tb complex donors combined with TG measurements can efficiently suppress the auto-fluorescence background of the sample matrix, the emission of direct excited acceptors (QDs), and the light scattering from the excitation source, improving the sensitivity, accuracy, and reliability of the sensing methods. Apart from this, by controlling the donor-acceptor distance, the TG measurements of the same FRET pair (Tb-to-QD625) with distinct PL decay times were successfully applied for DNA multiplexing, which increased the working efficiency and reduced the time and reagent cost of the sensing method. Besides, the ratiometric format FRET assays (ratio between PL intensities of acceptor and donor) can eliminate or reduce the environmental effect (e.g., temperature) on the photophysical properties of FRET pairs, further offering the possibility of bio-target/temperature dual-sensing, which is conducive to expanding the application of FRET strategies in both biological interactions probing and medium environmental monitoring.

When looking ahead to future work, the displacement immunoassay format proposed in the first study offers a promising new concept for homogeneous immuno-sensing technology and can be further investigated and generalized. Firstly, the displacement efficiency has the potential to be improved by modifying the antibody-antigen binding site. Additionally, by integrating non-traditional antibodies (such as single-chain antibodies, nanobodies, and heavy-chain antibodies, etc.) of varying sizes into the FRET-based displacement immunoassays, a new approach to homogeneous multiplexing can be achieved. In the second study, the multiplexing capacity of the proposed method could be improved by introducing spectral multiplexing, and the idea of using distinct Ln-to-QD FRET configurations as PL probes opens up more

possibilities for biosensing and imaging. In the third study, the proof-of-concept of DNA/temperature dual sensing is undeniably intriguing, but our current work only provided preliminary results. Its application and performance in practical biological substrates need to be tested and evaluated (in vivo and in vitro), and the monitoring of more complex environmental factors is also of great significance.

CHAPTER 7

Abbreviations

7. Abbreviations

BSA	bovine serum albumin
CB	conduction band
cDNA	complementary DNA
Cy5	cyanine 5
Cys	cysteine
DHLA	dihydrolipoic acid
DMF	N,N-dimethylformamide
dsDNA	double-strand DNA
EGFR	epidermal growth factor receptor
ELISA	enzyme-linked immunosorbent assay
ET	energy transfer
FBS	fetal bovine serum
FRET	Förster resonance energy transfer
FWHM	full-width at half-maximum
HER2	human epidermal growth factor receptor 2
His6	hexahistidine
IR	infrared
LLC	luminescent lanthanide complex
Ln	lanthanide
LOD	limit of detection
LTC	luminescent Tb complex
MB	magnetic bead
NB	nanobody
NHS	N-hydroxy-succinimide
NIR	near-infrared
NP	nanoparticle
PEG	amino-polyethylene-glycol
PL	photoluminescence

QD	quantum dot
R0	Förster distance
RCA	rolling circle amplification
sAv	streptavidin
sEGFR	soluble epidermal growth factor receptor
sEGFRvIII	soluble epidermal growth factor receptor variant III
SMCC	succinimidyl 4-N-maleimidomethyl cyclohexane-1-carboxylate
sulfo-EMCS	N-ε-maleimidocaproyl-oxysulfosuccinimide ester
TCEP	tris(2-carboxyethyl)phospine hydrochloride
TG	time-gated
TR	time-resolved
UCNP	upconversion nanoparticle
UV	ultraviolet
VB	valence band
Vis	visible

CHAPTER 8

Bibliography

8. Bibliography

[1] "The Nobel Prize in Chemistry 2023," NobelPrize.org. Accessed: Oct. 13, 2023. [Online]. Available: https://www.nobelprize.org/prizes/chemistry/2023/popular-information/

[2] U. Resch-Genger, M. Grabolle, S. Cavaliere-Jaricot, R. Nitschke, and T. Nann, "Quantum dots versus organic dyes as fluorescent labels," *Nat. Methods*, vol. 5, no. 9, Art. no. 9, Sep. 2008, doi: 10.1038/nmeth.1248.

[3] K. D. Wegner and N. Hildebrandt, "Quantum dots: bright and versatile in vitro and in vivo fluorescence imaging biosensors," *Chem. Soc. Rev.*, vol. 44, no. 14, pp. 4792–4834, Jul. 2015, doi: 10.1039/C4CS00532E.

[4] "Quantum Dots in Bioanalysis: A Review of Applications across Various Platforms for Fluorescence Spectroscopy and Imaging - Eleonora Petryayeva, W. Russ Algar, Igor L. Medintz, 2013." Accessed: Oct. 13, 2023. [Online]. Available: https://journals.sagepub.com/doi/10.1366/12-06948

[5] N. Hildebrandt *et al.*, "Energy Transfer with Semiconductor Quantum Dot Bioconjugates: A Versatile Platform for Biosensing, Energy Harvesting, and Other Developing Applications," *Chem. Rev.*, vol. 117, no. 2, pp. 536–711, Jan. 2017, doi: 10.1021/acs.chemrev.6b00030.

[6] M. Cardoso Dos Santos, W. R. Algar, I. L. Medintz, and N. Hildebrandt, "Quantum dots for Förster Resonance Energy Transfer (FRET)," *TrAC Trends Anal. Chem.*, vol. 125, p. 115819, Apr. 2020, doi: 10.1016/j.trac.2020.115819.

[7] L. Stryer, "Fluorescence Energy Transfer as a Spectroscopic Ruler," *Annu. Rev. Biochem.*, vol. 47, no. 1, pp. 819–846, 1978, doi: 10.1146/annurev.bi.47.070178.004131.

[8] I. L. Medintz and H. Mattoussi, "Quantum dot-based resonance energy transfer and its growing application in biology," *Phys. Chem. Chem. Phys.*, vol. 11, no. 1, pp. 17–45, Dec. 2008, doi: 10.1039/B813919A.

[9] W. R. Algar, H. Kim, I. L. Medintz, and N. Hildebrandt, "Emerging non-traditional Förster resonance energy transfer configurations with semiconductor quantum dots: Investigations and applications," *Coord. Chem. Rev.*, vol. 263–264, pp. 65–85, Mar. 2014, doi: 10.1016/j.ccr.2013.07.015.

[10] S. Silvi and A. Credi, "Luminescent sensors based on quantum dot–molecule conjugates,"

Chem. Soc. Rev., vol. 44, no. 13, pp. 4275–4289, Jun. 2015, doi: 10.1039/C4CS00400K.

[11] D. Geiβler and N. Hildebrandt, "Lanthanide Complexes in FRET Applications," *Curr. Inorg. Chem. Discontin.*, vol. 1, no. 1, pp. 17–35.

[12] B. Hötzer, I. L. Medintz, and N. Hildebrandt, "Fluorescence in Nanobiotechnology: Sophisticated Fluorophores for Novel Applications," *Small*, vol. 8, no. 15, pp. 2297–2326, 2012, doi: 10.1002/smll.201200109.

[13] N. Weibel, L. J. Charbonnière, M. Guardigli, A. Roda, and R. Ziessel, "Engineering of Highly Luminescent Lanthanide Tags Suitable for Protein Labeling and Time-Resolved Luminescence Imaging," *J. Am. Chem. Soc.*, vol. 126, no. 15, pp. 4888–4896, Apr. 2004, doi: 10.1021/ja031886k.

[14] J. Xu, T. M. Corneillie, E. G. Moore, G.-L. Law, N. G. Butlin, and K. N. Raymond, "Octadentate Cages of Tb(III) 2-Hydroxyisophthalamides: A New Standard for Luminescent Lanthanide Labels," *J. Am. Chem. Soc.*, vol. 133, no. 49, pp. 19900–19910, Dec. 2011, doi: 10.1021/ja2079898.

[15] C. Chen *et al.*, "Single-Nanoparticle Cell Barcoding by Tunable FRET from Lanthanides to Quantum Dots," *Angew. Chem. Int. Ed.*, vol. 57, no. 41, pp. 13686–13690, 2018, doi: 10.1002/anie.201807585.

[16] N. Hildebrandt, K. D. Wegner, and W. R. Algar, "Luminescent terbium complexes: Superior Förster resonance energy transfer donors for flexible and sensitive multiplexed biosensing," *Coord. Chem. Rev.*, vol. 273–274, pp. 125–138, Aug. 2014, doi: 10.1016/j.ccr.2014.01.020.

[17] Y.-T. Wu *et al.*, "Quantum Dot–Based FRET Immunoassay for HER2 Using Ultrasmall Affinity Proteins," *Small*, vol. 14, no. 35, p. 1802266, 2018, doi: 10.1002/smll.201802266.

[18] X. Qiu, K. D. Wegner, Y.-T. Wu, P. M. P. van Bergen en Henegouwen, T. L. Jennings, and N. Hildebrandt, "Nanobodies and Antibodies for Duplexed EGFR/HER2 Immunoassays Using Terbium-to-Quantum Dot FRET," *Chem. Mater.*, vol. 28, no. 22, pp. 8256–8267, Nov. 2016, doi: 10.1021/acs.chemmater.6b03198.

[19] X. Qiu and N. Hildebrandt, "Rapid and Multiplexed MicroRNA Diagnostic Assay Using Quantum Dot-Based Förster Resonance Energy Transfer," *ACS Nano*, vol. 9, no. 8, pp. 8449–8457, Aug. 2015, doi: 10.1021/acsnano.5b03364.

[20] A. F. Gazdar, “Epidermal growth factor receptor inhibition in lung cancer: the evolving role of individualized therapy,” *Cancer Metastasis Rev.*, vol. 29, no. 1, pp. 37–48, Mar. 2010, doi: 10.1007/s10555-010-9201-z.

[21] M. T. Weigel and M. Dowsett, “Current and emerging biomarkers in breast cancer: prognosis and prediction,” *Endocr. Relat. Cancer*, vol. 17, no. 4, pp. R245–R262, Dec. 2010, doi: 10.1677/ERC-10-0136.

[22] T. Förster, “Zwischenmolekulare Energiewanderung und Fluoreszenz,” *Ann. Phys.*, vol. 437, no. 1–2, pp. 55–75, 1948, doi: 10.1002/andp.19484370105.

[23] N. Hildebrandt, “How to Apply FRET: From Experimental Design to Data Analysis,” in *FRET – Förster Resonance Energy Transfer*, John Wiley & Sons, Ltd, 2013, pp. 105–163. doi: 10.1002/9783527656028.ch05.

[24] B. W. van der Meer, “Förster Theory,” in *FRET – Förster Resonance Energy Transfer*, John Wiley & Sons, Ltd, 2013, pp. 23–62. doi: 10.1002/9783527656028.ch03.

[25] R. M. Clegg, “The History of Fret,” in *Reviews in Fluorescence 2006*, C. D. Geddes and J. R. Lakowicz, Eds., in Reviews in Fluorescence. , Boston, MA: Springer US, 2006, pp. 1–45. doi: 10.1007/0-387-33016-X_1.

[26] D. Shrestha, A. Jenei, P. Nagy, G. Vereb, and J. Szöllősi, “Understanding FRET as a Research Tool for Cellular Studies,” *Int. J. Mol. Sci.*, vol. 16, no. 4, Art. no. 4, Apr. 2015, doi: 10.3390/ijms16046718.

[27] X. Qiu and N. Hildebrandt, “A clinical role for Förster resonance energy transfer in molecular diagnostics of disease,” *Expert Rev. Mol. Diagn.*, vol. 19, no. 9, pp. 767–771, Sep. 2019, doi: 10.1080/14737159.2019.1649144.

[28] M. Imani, N. Mohajeri, M. Rastegar, and N. Zarghami, “Recent advances in FRET-Based biosensors for biomedical applications,” *Anal. Biochem.*, vol. 630, p. 114323, Oct. 2021, doi: 10.1016/j.ab.2021.114323.

[29] C. Fang, Y. Huang, and Y. Zhao, “Review of FRET biosensing and its application in biomolecular detection,” *Am. J. Transl. Res.*, vol. 15, no. 2, pp. 694–709, Feb. 2023.

[30] V. Gubala, L. F. Harris, A. J. Ricco, M. X. Tan, and D. E. Williams, “Point of Care Diagnostics: Status and Future,” *Anal. Chem.*, vol. 84, no. 2, pp. 487–515, Jan. 2012, doi: 10.1021/ac2030199.

[31] E. A. Jares-Erijman and T. M. Jovin, “FRET imaging,” *Nat. Biotechnol.*, vol. 21, no. 11, pp. 1387–1395, 2003, doi: 10.1038/nbt896.

[32] E. A. Jares-Erijman and T. M. Jovin, “Imaging molecular interactions in living cells by FRET microscopy,” *Curr. Opin. Chem. Biol.*, vol. 10, no. 5, pp. 409–416, Oct. 2006, doi: 10.1016/j.cbpa.2006.08.021.

[33] I. A. Darwish, “Immunoassay Methods and their Applications in Pharmaceutical Analysis: Basic Methodology and Recent Advances,” *Int. J. Biomed. Sci. IJBS*, vol. 2, no. 3, pp. 217–235, Sep. 2006.

[34] “The Immunoassay Handbook - 4th Edition.” Accessed: Sep. 22, 2023. [Online]. Available: https://shop.elsevier.com/books/the-immunoassay-handbook/wild/978-0-08-097037-0

[35] A. Q. Rani, B. Zhu, H. Ueda, and T. Kitaguchi, “Recent progress in homogeneous immunosensors based on fluorescence or bioluminescence using antibody engineering,” *Analyst*, vol. 148, no. 7, pp. 1422–1429, Mar. 2023, doi: 10.1039/D2AN01913B.

[36] W. R. Algar, N. Hildebrandt, S. S. Vogel, and I. L. Medintz, “FRET as a biomolecular research tool — understanding its potential while avoiding pitfalls,” *Nat. Methods*, vol. 16, no. 9, Art. no. 9, Sep. 2019, doi: 10.1038/s41592-019-0530-8.

[37] E. F. Ullman, M. Schwarzberg, and K. E. Rubenstein, “Fluorescent excitation transfer immunoassay. A general method for determination of antigens.,” *J. Biol. Chem.*, vol. 251, no. 14, pp. 4172–4178, Jul. 1976, doi: 10.1016/S0021-9258(17)33277-5.

[38] P. R. Selvin and J. E. Hearst, “Luminescence energy transfer using a terbium chelate: improvements on fluorescence energy transfer.,” *Proc. Natl. Acad. Sci.*, vol. 91, no. 21, pp. 10024–10028, Oct. 1994, doi: 10.1073/pnas.91.21.10024.

[39] H. Ueda *et al.*, “Homogeneous Noncompetitive Immunoassay Based on the Energy Transfer Between Fluorolabeled Antibody Variable Domains (Open Sandwich Fluoroimmunoassay),” *BioTechniques*, vol. 27, no. 4, pp. 738–742, Oct. 1999, doi: 10.2144/99274st04.

[40] Q. Wei *et al.*, “Development of an open sandwich fluoroimmunoassay based on fluorescence resonance energy transfer,” *Anal. Biochem.*, vol. 358, no. 1, pp. 31–37, Nov. 2006, doi: 10.1016/j.ab.2006.08.019.

[41] A. Kupstat, M. U. Kumke, and N. Hildebrandt, “Toward sensitive, quantitative point-of-

care testing (POCT) of protein markers: miniaturization of a homogeneous time-resolved fluoroimmunoassay for prostate-specific antigen detection," *Analyst*, vol. 136, no. 5, pp. 1029–1035, Feb. 2011, doi: 10.1039/C0AN00684J.

[42] M.-J. Chen, Y.-S. Wu, G.-F. Lin, J.-Y. Hou, M. Li, and T.-C. Liu, "Quantum-dot-based homogeneous time-resolved fluoroimmunoassay of alpha-fetoprotein," *Anal. Chim. Acta*, vol. 741, pp. 100–105, Sep. 2012, doi: 10.1016/j.aca.2012.06.042.

[43] D. W. Piston and G.-J. Kremers, "Fluorescent protein FRET: the good, the bad and the ugly," *Trends Biochem. Sci.*, vol. 32, no. 9, pp. 407–414, Sep. 2007, doi: 10.1016/j.tibs.2007.08.003.

[44] D. Geißler, S. Stufler, H.-G. Löhmannsröben, and N. Hildebrandt, "Six-Color Time-Resolved Förster Resonance Energy Transfer for Ultrasensitive Multiplexed Biosensing," *J. Am. Chem. Soc.*, vol. 135, no. 3, pp. 1102–1109, Jan. 2013, doi: 10.1021/ja310317n.

[45] V. Laitala and I. Hemmilä, "Homogeneous Assay Based on Anti-Stokes' Shift Time-Resolved Fluorescence Resonance Energy-Transfer Measurement," *Anal. Chem.*, vol. 77, no. 5, pp. 1483–1487, Mar. 2005, doi: 10.1021/ac048414o.

[46] S. H. Lim *et al.*, "Circulating tumour cells and circulating free nucleic acid as prognostic and predictive biomarkers in colorectal cancer," *Cancer Lett.*, vol. 346, no. 1, pp. 24–33, Apr. 2014, doi: 10.1016/j.canlet.2013.12.019.

[47] S. Y. Lin, J. A. Linehan, T. G. Wilson, and D. S. B. Hoon, "Emerging Utility of Urinary Cell-free Nucleic Acid Biomarkers for Prostate, Bladder, and Renal Cancers," *Eur. Urol. Focus*, vol. 3, no. 2, pp. 265–272, Apr. 2017, doi: 10.1016/j.euf.2017.03.009.

[48] "Molecular Diagnostics - 3rd Edition." Accessed: Sep. 22, 2023. [Online]. Available: https://shop.elsevier.com/books/molecular-diagnostics/patrinos/978-0-12-802971-8

[49] M. Lapin *et al.*, "Fragment size and level of cell-free DNA provide prognostic information in patients with advanced pancreatic cancer," *J. Transl. Med.*, vol. 16, no. 1, p. 300, Nov. 2018, doi: 10.1186/s12967-018-1677-2.

[50] B. N. Davis-Dusenbery and A. Hata, "MicroRNA in Cancer: The Involvement of Aberrant MicroRNA Biogenesis Regulatory Pathways," *Genes Cancer*, vol. 1, no. 11, pp. 1100–1114, Nov. 2010, doi: 10.1177/1947601910396213.

[51] L. E. Morrison, T. C. Halder, and L. M. Stols, "Solution-phase detection of polynucleotides using interacting fluorescent labels and competitive hybridization," *Anal.*

Biochem., vol. 183, no. 2, pp. 231–244, Dec. 1989, doi: 10.1016/0003-2697(89)90473-9.

[52] R. A. Cardullo, S. Agrawal, C. Flores, P. C. Zamecnik, and D. E. Wolf, "Detection of nucleic acid hybridization by nonradiative fluorescence resonance energy transfer.," *Proc. Natl. Acad. Sci.*, vol. 85, no. 23, pp. 8790–8794, Dec. 1988, doi: 10.1073/pnas.85.23.8790.

[53] S. Tyagi and F. R. Kramer, "Molecular Beacons: Probes that Fluoresce upon Hybridization," *Nat. Biotechnol.*, vol. 14, no. 3, Art. no. 3, Mar. 1996, doi: 10.1038/nbt0396-303.

[54] D. J. French, C. L. Archard, T. Brown, and D. G. McDowell, "HyBeaconTM probes: a new tool for DNA sequence detection and allele discrimination," *Mol. Cell. Probes*, vol. 15, no. 6, pp. 363–374, Dec. 2001, doi: 10.1006/mcpr.2001.0384.

[55] D. J. French, C. L. Archard, M. T. Andersen, and D. G. McDowell, "Ultra-rapid DNA analysis using HyBeacon^{TM} probes and direct PCR amplification from saliva," *Mol. Cell. Probes*, vol. 16, no. 5, pp. 319–326, Oct. 2002, doi: 10.1006/mcpr.2002.0425.

[56] D. J. French, D. Jones, D. G. McDowell, J. A. Thomson, and P. G. Debenham, "Analysis of multiple single nucleotide polymorphisms closely positioned in the ovine PRNPgene using linear fluorescent probes and melting curve analysis," *BMC Infect. Dis.*, vol. 7, no. 1, p. 90, Aug. 2007, doi: 10.1186/1471-2334-7-90.

[57] G. Tyler, "Rare earth elements in soil and plant systems - A review," *Plant Soil*, vol. 267, no. 1, pp. 191–206, Dec. 2004, doi: 10.1007/s11104-005-4888-2.

[58] M. H. V. Werts, "Making sense of Lanthanide Luminescence," *Sci. Prog.*, vol. 88, no. 2, pp. 101–131, May 2005, doi: 10.3184/003685005783238435.

[59] E. G. Moore, A. P. S. Samuel, and K. N. Raymond, "From Antenna to Assay: Lessons Learned in Lanthanide Luminescence," *Acc. Chem. Res.*, vol. 42, no. 4, pp. 542–552, Apr. 2009, doi: 10.1021/ar800211j.

[60] S. Schlücker, "Surface-Enhanced Raman Spectroscopy: Concepts and Chemical Applications," *Angew. Chem. Int. Ed.*, vol. 53, no. 19, pp. 4756–4795, 2014, doi: 10.1002/anie.201205748.

[61] J.-C. G. Bünzli and C. Piguet, "Taking advantage of luminescent lanthanide ions," *Chem. Soc. Rev.*, vol. 34, no. 12, pp. 1048–1077, Nov. 2005, doi: 10.1039/B406082M.

[62] M. C. Heffern, L. M. Matosziuk, and T. J. Meade, “Lanthanide Probes for Bioresponsive Imaging,” *Chem. Rev.*, vol. 114, no. 8, pp. 4496–4539, Apr. 2014, doi: 10.1021/cr400477t.

[63] J.-C. G. Bünzli, “Luminescent Lanthanide Probes as Diagnostic and Therapeutic Tools,” in *Metal Ions in Biological Systems*, CRC Press, 2004.

[64] P. Hänninen and H. Härmä, *Lanthanide Luminescence: Photophysical, Analytical and Biological Aspects*. Springer Science & Business Media, 2011.

[65] V. V. Zherdeva and A. P. Savitsky, “Using lanthanide-based resonance energy transfer for in vitro and in vivo studies of biological processes,” *Biochem. Mosc.*, vol. 77, no. 13, pp. 1553–1574, Dec. 2012, doi: 10.1134/S0006297912130111.

[66] J.-C. G. Bünzli, “Lanthanide light for biology and medical diagnosis,” *J. Lumin.*, vol. 170, pp. 866–878, Feb. 2016, doi: 10.1016/j.jlumin.2015.07.033.

[67] S. V. Eliseeva and J.-C. G. Bünzli, “Lanthanide luminescence for functional materials and bio-sciences,” *Chem. Soc. Rev.*, vol. 39, no. 1, pp. 189–227, Dec. 2009, doi: 10.1039/B905604C.

[68] R. D. Teo, J. Termini, and H. B. Gray, “Lanthanides: Applications in Cancer Diagnosis and Therapy,” *J. Med. Chem.*, vol. 59, no. 13, pp. 6012–6024, Jul. 2016, doi: 10.1021/acs.jmedchem.5b01975.

[69] Y. Min, J. Li, F. Liu, P. Padmanabhan, E. K. L. Yeow, and B. Xing, “Recent Advance of Biological Molecular Imaging Based on Lanthanide-Doped Upconversion-Luminescent Nanomaterials,” *Nanomaterials*, vol. 4, no. 1, Art. no. 1, Mar. 2014, doi: 10.3390/nano4010129.

[70] A. Thibon and V. C. Pierre, “Principles of responsive lanthanide-based luminescent probes for cellular imaging,” *Anal. Bioanal. Chem.*, vol. 394, no. 1, pp. 107–120, May 2009, doi: 10.1007/s00216-009-2683-2.

[71] X. Qiu, J. Guo, J. Xu, and N. Hildebrandt, “Three-Dimensional FRET Multiplexing for DNA Quantification with Attomolar Detection Limits,” *J. Phys. Chem. Lett.*, vol. 9, no. 15, pp. 4379–4384, Aug. 2018, doi: 10.1021/acs.jpclett.8b01944.

[72] A. P. Alivisatos, “Semiconductor Clusters, Nanocrystals, and Quantum Dots,” *Science*, vol. 271, no. 5251, pp. 933–937, Feb. 1996, doi: 10.1126/science.271.5251.933.

[73] K. Kalyanasundaram, E. Borgarello, D. Duonghong, and M. Grätzel, “Cleavage of Water

by Visible-Light Irradiation of Colloidal CdS Solutions; Inhibition of Photocorrosion by RuO2," *Angew. Chem. Int. Ed. Engl.*, vol. 20, no. 11, pp. 987–988, 1981, doi: 10.1002/anie.198109871.

[74] A. Efros and A. Efros, "Interband Light Absorption in Semiconductor Spheres," *Sov. Phys. Semicond.*, vol. 16, pp. 772–775, Jul. 1982.

[75] R. Rossetti, S. Nakahara, and L. E. Brus, "Quantum size effects in the redox potentials, resonance Raman spectra, and electronic spectra of CdS crystallites in aqueous solution," *J. Chem. Phys.*, vol. 79, no. 2, pp. 1086–1088, Jul. 1983, doi: 10.1063/1.445834.

[76] A. I. Ekimov, Al. L. Efros, and A. A. Onushchenko, "Quantum size effect in semiconductor microcrystals," *Solid State Commun.*, vol. 56, no. 11, pp. 921–924, Dec. 1985, doi: 10.1016/S0038-1098(85)80025-9.

[77] C. B. Murray, D. J. Norris, and M. G. Bawendi, "Synthesis and characterization of nearly monodisperse CdE (E = sulfur, selenium, tellurium) semiconductor nanocrystallites," *J. Am. Chem. Soc.*, vol. 115, no. 19, pp. 8706–8715, Sep. 1993, doi: 10.1021/ja00072a025.

[78] V. L. Colvin, M. C. Schlamp, and A. P. Alivisatos, "Light-emitting diodes made from cadmium selenide nanocrystals and a semiconducting polymer," *Nature*, vol. 370, no. 6488, Art. no. 6488, Aug. 1994, doi: 10.1038/370354a0.

[79] W. C. W. Chan and S. Nie, "Quantum Dot Bioconjugates for Ultrasensitive Nonisotopic Detection," *Science*, vol. 281, no. 5385, pp. 2016–2018, Sep. 1998, doi: 10.1126/science.281.5385.2016.

[80] M. Bruchez, M. Moronne, P. Gin, S. Weiss, and A. P. Alivisatos, "Semiconductor Nanocrystals as Fluorescent Biological Labels," *Science*, vol. 281, no. 5385, pp. 2013–2016, Sep. 1998, doi: 10.1126/science.281.5385.2013.

[81] E. Petryayeva, W. R. Algar, and I. L. Medintz, "Quantum Dots in Bioanalysis: A Review of Applications across Various Platforms for Fluorescence Spectroscopy and Imaging," *Appl. Spectrosc.*, vol. 67, no. 3, pp. 215–252, Mar. 2013, doi: 10.1366/12-06948.

[82] O. Chen *et al.*, "Compact high-quality CdSe–CdS core–shell nanocrystals with narrow emission linewidths and suppressed blinking," *Nat. Mater.*, vol. 12, no. 5, Art. no. 5, May 2013, doi: 10.1038/nmat3539.

[83] W. W. Yu, L. Qu, W. Guo, and X. Peng, "Experimental Determination of the Extinction Coefficient of CdTe, CdSe, and CdS Nanocrystals," *Chem. Mater.*, vol. 15, no. 14, pp.

2854–2860, Jul. 2003, doi: 10.1021/cm034081k.

[84] B. O. Dabbousi *et al.*, "(CdSe)ZnS Core−Shell Quantum Dots: Synthesis and Characterization of a Size Series of Highly Luminescent Nanocrystallites," *J. Phys. Chem. B*, vol. 101, no. 46, pp. 9463–9475, Nov. 1997, doi: 10.1021/jp971091y.

[85] X. Peng, M. C. Schlamp, A. V. Kadavanich, and A. P. Alivisatos, "Epitaxial Growth of Highly Luminescent CdSe/CdS Core/Shell Nanocrystals with Photostability and Electronic Accessibility," *J. Am. Chem. Soc.*, vol. 119, no. 30, pp. 7019–7029, Jul. 1997, doi: 10.1021/ja970754m.

[86] J. H. Yu *et al.*, "High-resolution three-photon biomedical imaging using doped ZnS nanocrystals," *Nat. Mater.*, vol. 12, no. 4, Art. no. 4, Apr. 2013, doi: 10.1038/nmat3565.

[87] Y. Kim, W. Kim, H.-J. Yoon, and S. K. Shin, "Bioconjugation of Hydroxylated Semiconductor Nanocrystals and Background-Free Biomolecule Detection," *Bioconjug. Chem.*, vol. 21, no. 7, pp. 1305–1311, Jul. 2010, doi: 10.1021/bc100114q.

[88] W. R. Algar and U. J. Krull, "Adsorption and Hybridization of Oligonucleotides on Mercaptoacetic Acid-Capped CdSe/ZnS Quantum Dots and Quantum Dot−Oligonucleotide Conjugates," *Langmuir*, vol. 22, no. 26, pp. 11346–11352, Dec. 2006, doi: 10.1021/la062217y.

[89] R. Wilson, D. G. Spiller, A. Beckett, I. A. Prior, and V. Sée, "Highly Stable Dextran-Coated Quantum Dots for Biomolecular Detection and Cellular Imaging," *Chem. Mater.*, vol. 22, no. 23, pp. 6361–6369, Dec. 2010, doi: 10.1021/cm1023635.

[90] R. Freeman, R. Gill, I. Shweky, M. Kotler, U. Banin, and I. Willner, "Biosensing and Probing of Intracellular Metabolic Pathways by NADH-Sensitive Quantum Dots," *Angew. Chem. Int. Ed.*, vol. 48, no. 2, pp. 309–313, 2009, doi: 10.1002/anie.200803421.

[91] A. Kongkanand, "Interfacial Water Transport Measurements in Nafion Thin Films Using a Quartz-Crystal Microbalance," *J. Phys. Chem. C*, vol. 115, no. 22, pp. 11318–11325, Jun. 2011, doi: 10.1021/jp2028214.

[92] V. R. Hering, G. Gibson, R. I. Schumacher, A. Faljoni-Alario, and M. J. Politi, "Energy Transfer between CdSe/ZnS Core/Shell Quantum Dots and Fluorescent Proteins," *Bioconjug. Chem.*, vol. 18, no. 6, pp. 1705–1708, Nov. 2007, doi: 10.1021/bc700147j.

[93] A. Hoshino *et al.*, "Physicochemical Properties and Cellular Toxicity of Nanocrystal Quantum Dots Depend on Their Surface Modification," *Nano Lett.*, vol. 4, no. 11, pp.

2163–2169, Nov. 2004, doi: 10.1021/nl048715d.

[94] H. Mattoussi *et al.*, “Self-Assembly of CdSe−ZnS Quantum Dot Bioconjugates Using an Engineered Recombinant Protein,” *J. Am. Chem. Soc.*, vol. 122, no. 49, pp. 12142–12150, Dec. 2000, doi: 10.1021/ja002535y.

[95] E.-C. Kang, A. Ogura, K. Kataoka, and Y. Nagasaki, “Preparation of Water-soluble PEGylated Semiconductor Nanocrystals,” *Chem. Lett.*, vol. 33, no. 7, pp. 840–841, Jul. 2004, doi: 10.1246/cl.2004.840.

[96] M. E. Åkerman, W. C. W. Chan, P. Laakkonen, S. N. Bhatia, and E. Ruoslahti, “Nanocrystal targeting in vivo,” *Proc. Natl. Acad. Sci.*, vol. 99, no. 20, pp. 12617–12621, Oct. 2002, doi: 10.1073/pnas.152463399.

[97] B. C. Mei, K. Susumu, I. L. Medintz, and H. Mattoussi, “Polyethylene glycol-based bidentate ligands to enhance quantum dot and gold nanoparticle stability in biological media,” *Nat. Protoc.*, vol. 4, no. 3, Art. no. 3, Mar. 2009, doi: 10.1038/nprot.2008.243.

[98] K. Susumu, B. C. Mei, and H. Mattoussi, “Multifunctional ligands based on dihydrolipoic acid and polyethylene glycol to promote biocompatibility of quantum dots,” *Nat. Protoc.*, vol. 4, no. 3, Art. no. 3, Mar. 2009, doi: 10.1038/nprot.2008.247.

[99] H. T. Uyeda, I. L. Medintz, J. K. Jaiswal, S. M. Simon, and H. Mattoussi, “Synthesis of Compact Multidentate Ligands to Prepare Stable Hydrophilic Quantum Dot Fluorophores,” *J. Am. Chem. Soc.*, vol. 127, no. 11, pp. 3870–3878, Mar. 2005, doi: 10.1021/ja044031w.

[100] K. Susumu *et al.*, “Multifunctional Compact Zwitterionic Ligands for Preparing Robust Biocompatible Semiconductor Quantum Dots and Gold Nanoparticles,” *J. Am. Chem. Soc.*, vol. 133, no. 24, pp. 9480–9496, Jun. 2011, doi: 10.1021/ja201919s.

[101] W. R. Algar, K. Susumu, J. B. Delehanty, and I. L. Medintz, “Semiconductor Quantum Dots in Bioanalysis: Crossing the Valley of Death,” *Anal. Chem.*, vol. 83, no. 23, pp. 8826–8837, Dec. 2011, doi: 10.1021/ac201331r.

[102] T. Nann and P. Mulvaney, “Single Quantum Dots in Spherical Silica Particles,” *Angew. Chem. Int. Ed.*, vol. 43, no. 40, pp. 5393–5396, 2004, doi: 10.1002/anie.200460752.

[103] D. Gerion *et al.*, “Synthesis and Properties of Biocompatible Water-Soluble Silica-Coated CdSe/ZnS Semiconductor Quantum Dots,” *J. Phys. Chem. B*, vol. 105, no. 37, pp. 8861–8871, Sep. 2001, doi: 10.1021/jp0105488.

[104] M. Darbandi, R. Thomann, and T. Nann, “Single Quantum Dots in Silica Spheres by Microemulsion Synthesis,” *Chem. Mater.*, vol. 17, no. 23, pp. 5720–5725, Nov. 2005, doi: 10.1021/cm051467h.

[105] S. T. Selvan, T. T. Tan, and J. Y. Ying, “Robust, Non-Cytotoxic, Silica-Coated CdSe Quantum Dots with Efficient Photoluminescence,” *Adv. Mater.*, vol. 17, no. 13, pp. 1620–1625, 2005, doi: 10.1002/adma.200401960.

[106] S. T. Selvan, P. K. Patra, C. Y. Ang, and J. Y. Ying, “Synthesis of Silica-Coated Semiconductor and Magnetic Quantum Dots and Their Use in the Imaging of Live Cells,” *Angew. Chem. Int. Ed.*, vol. 46, no. 14, pp. 2448–2452, 2007, doi: 10.1002/anie.200604245.

[107] K. E. Sapsford *et al.*, “Functionalizing Nanoparticles with Biological Molecules: Developing Chemistries that Facilitate Nanotechnology,” *Chem. Rev.*, vol. 113, no. 3, pp. 1904–2074, Mar. 2013, doi: 10.1021/cr300143v.

[108] J. B. Blanco-Canosa *et al.*, “Recent progress in the bioconjugation of quantum dots,” *Coord. Chem. Rev.*, vol. 263–264, pp. 101–137, Mar. 2014, doi: 10.1016/j.ccr.2013.08.030.

[109] A. Schroedter, H. Weller, R. Eritja, W. E. Ford, and J. M. Wessels, “Biofunctionalization of Silica-Coated CdTe and Gold Nanocrystals,” *Nano Lett.*, vol. 2, no. 12, pp. 1363–1367, Dec. 2002, doi: 10.1021/nl025779k.

[110] H. Akkiraju, J. Bonor, and A. Nohe, “Development of Fluorescently Tagged BMP-2 analog,” *Biophys. J.*, vol. 100, no. 3, p. 137a, Feb. 2011, doi: 10.1016/j.bpj.2010.12.952.

[111] Y. Wang, Y. Bai, and X. Wei, “Conjugation behaviours of CdTe quantum dots and antibody by a novel immunochromatographic method,” *IET Nanobiotechnol.*, vol. 5, no. 1, pp. 14–19, Mar. 2011, doi: 10.1049/iet-nbt.2010.0001.

[112] A. Hoshino *et al.*, “Quantum Dots Targeted to the Assigned Organelle in Living Cells,” *Microbiol. Immunol.*, vol. 48, no. 12, pp. 985–994, 2004, doi: 10.1111/j.1348-0421.2004.tb03621.x.

[113] J. M. Slocik, J. T. Moore, and D. W. Wright, “Monoclonal Antibody Recognition of Histidine-Rich Peptide Encapsulated Nanoclusters,” *Nano Lett.*, vol. 2, no. 3, pp. 169–173, Mar. 2002, doi: 10.1021/nl015706l.

[114] K. Boeneman *et al.*, “Quantum Dot DNA Bioconjugates: Attachment Chemistry Strongly

Influences the Resulting Composite Architecture," *ACS Nano*, vol. 4, no. 12, pp. 7253–7266, Dec. 2010, doi: 10.1021/nn1021346.

[115]E. R. Goldman *et al.*, "Avidin: A Natural Bridge for Quantum Dot-Antibody Conjugates," *J. Am. Chem. Soc.*, vol. 124, no. 22, pp. 6378–6382, Jun. 2002, doi: 10.1021/ja0125570.

[116] J. Zhou, Y. Yang, and C. Zhang, "Toward Biocompatible Semiconductor Quantum Dots: From Biosynthesis and Bioconjugation to Biomedical Application," *Chem. Rev.*, vol. 115, no. 21, pp. 11669–11717, Nov. 2015, doi: 10.1021/acs.chemrev.5b00049.

[117] A. R. Clapp, I. L. Medintz, B. R. Fisher, G. P. Anderson, and H. Mattoussi, "Can Luminescent Quantum Dots Be Efficient Energy Acceptors with Organic Dye Donors?," *J. Am. Chem. Soc.*, vol. 127, no. 4, pp. 1242–1250, Feb. 2005, doi: 10.1021/ja045676z.

[118] N. Hildebrandt, L. J. Charbonnière, M. Beck, R. F. Ziessel, and H.-G. Löhmannsröben, "Quantum Dots as Efficient Energy Acceptors in a Time-Resolved Fluoroimmunoassay," *Angew. Chem. Int. Ed.*, vol. 44, no. 46, pp. 7612–7615, 2005, doi: 10.1002/anie.200501552.

[119] Z. Farka, T. Juřík, D. Kovář, L. Trnková, and P. Skládal, "Nanoparticle-Based Immunochemical Biosensors and Assays: Recent Advances and Challenges," *Chem. Rev.*, vol. 117, no. 15, pp. 9973–10042, Aug. 2017, doi: 10.1021/acs.chemrev.7b00037.

[120] G. Bao, M. Tang, J. Zhao, and X. Zhu, "Nanobody: a promising toolkit for molecular imaging and disease therapy," *EJNMMI Res.*, vol. 11, no. 1, p. 6, Jan. 2021, doi: 10.1186/s13550-021-00750-5.

[121] E. A. Bastos-Soares *et al.*, "Single domain antibodies in the development of immunosensors for diagnostics," *Int. J. Biol. Macromol.*, vol. 165, pp. 2244–2252, Dec. 2020, doi: 10.1016/j.ijbiomac.2020.10.031.

[122] I. Jovčevska and S. Muyldermans, "The Therapeutic Potential of Nanobodies," *BioDrugs*, vol. 34, no. 1, pp. 11–26, Feb. 2020, doi: 10.1007/s40259-019-00392-z.

[123] M. Liu, L. Li, D. Jin, and Y. Liu, "Nanobody—A versatile tool for cancer diagnosis and therapeutics," *WIREs Nanomedicine Nanobiotechnology*, vol. 13, no. 4, p. e1697, 2021, doi: 10.1002/wnan.1697.

[124] T. S. Pillay and S. Muyldermans, "Application of Single-Domain Antibodies ('Nanobodies') to Laboratory Diagnosis," *Ann. Lab. Med.*, vol. 41, no. 6, pp. 549–558, Nov. 2021, doi: 10.3343/alm.2021.41.6.549.

[125] D. Schumacher, J. Helma, A. F. L. Schneider, H. Leonhardt, and C. P. R. Hackenberger, "Nanobodies: Chemical Functionalization Strategies and Intracellular Applications," *Angew. Chem. Int. Ed.*, vol. 57, no. 9, pp. 2314–2333, 2018, doi: 10.1002/anie.201708459.

[126] S. Oliveira, R. Heukers, J. Sornkom, R. J. Kok, and P. M. P. van Bergen en Henegouwen, "Targeting tumors with nanobodies for cancer imaging and therapy," *J. Controlled Release*, vol. 172, no. 3, pp. 607–617, Dec. 2013, doi: 10.1016/j.jconrel.2013.08.298.

[127] J. H. Soh, H.-M. Chan, and J. Y. Ying, "Strategies for developing sensitive and specific nanoparticle-based lateral flow assays as point-of-care diagnostic device," *Nano Today*, vol. 30, p. 100831, Feb. 2020, doi: 10.1016/j.nantod.2019.100831.

[128] C. Leduc *et al.*, "A Highly Specific Gold Nanoprobe for Live-Cell Single-Molecule Imaging," *Nano Lett.*, vol. 13, no. 4, pp. 1489–1494, Apr. 2013, doi: 10.1021/nl304561g.

[129] Q. Zhou, G. Li, Y. Zhang, M. Zhu, Y. Wan, and Y. Shen, "Highly Selective and Sensitive Electrochemical Immunoassay of Cry1C Using Nanobody and π–π Stacked Graphene Oxide/Thionine Assembly," *Anal. Chem.*, vol. 88, no. 19, pp. 9830–9836, Oct. 2016, doi: 10.1021/acs.analchem.6b02945.

[130] X. Tang, P. Li, Q. Zhang, Z. Zhang, W. Zhang, and J. Jiang, "Time-Resolved Fluorescence Immunochromatographic Assay Developed Using Two Idiotypic Nanobodies for Rapid, Quantitative, and Simultaneous Detection of Aflatoxin and Zearalenone in Maize and Its Products," *Anal. Chem.*, vol. 89, no. 21, pp. 11520–11528, Nov. 2017, doi: 10.1021/acs.analchem.7b02794.

[131] C. N. Loynachan *et al.*, "Platinum Nanocatalyst Amplification: Redefining the Gold Standard for Lateral Flow Immunoassays with Ultrabroad Dynamic Range," *ACS Nano*, vol. 12, no. 1, pp. 279–288, Jan. 2018, doi: 10.1021/acsnano.7b06229.

[132] S. Modi, N. F. Higgs, D. Sheehan, L. D. Griffin, and J. T. Kittler, "Quantum dot conjugated nanobodies for multiplex imaging of protein dynamics at synapses," *Nanoscale*, vol. 10, no. 21, pp. 10241–10249, May 2018, doi: 10.1039/C7NR09130C.

[133] Y. Wang, Y. Wang, G. Chen, Y. Li, W. Xu, and S. Gong, "Quantum-Dot-Based Theranostic Micelles Conjugated with an Anti-EGFR Nanobody for Triple-Negative Breast Cancer Therapy," *ACS Appl. Mater. Interfaces*, vol. 9, no. 36, pp. 30297–30305, Sep. 2017, doi: 10.1021/acsami.7b05654.

[134] K. Chen *et al.*, "Coupling metal-organic framework nanosphere and nanobody for

boosted photoelectrochemical immunoassay of Human Epididymis Protein 4," *Anal. Chim. Acta*, vol. 1107, pp. 145–154, Apr. 2020, doi: 10.1016/j.aca.2020.02.011.

[135] M. Díaz-González, A. de la Escosura-Muñiz, M. T. Fernandez-Argüelles, F. J. García Alonso, and J. M. Costa-Fernandez, "Quantum Dot Bioconjugates for Diagnostic Applications," *Top. Curr. Chem.*, vol. 378, no. 2, p. 35, Mar. 2020, doi: 10.1007/s41061-020-0296-6.

[136] P. T. Snee, "Semiconductor quantum dot FRET: Untangling energy transfer mechanisms in bioanalytical assays," *TrAC Trends Anal. Chem.*, vol. 123, p. 115750, Feb. 2020, doi: 10.1016/j.trac.2019.115750.

[137] Z. Tang, X. Liu, Y. Wang, Q. Chen, B. D. Hammock, and Y. Xu, "Nanobody-based fluorescence resonance energy transfer immunoassay for noncompetitive and simultaneous detection of ochratoxin a and ochratoxin B," *Environ. Pollut.*, vol. 251, pp. 238–245, Aug. 2019, doi: 10.1016/j.envpol.2019.04.135.

[138] Z. Tang *et al.*, "Ultrasensitive and rapid detection of ochratoxin A in agro-products by a nanobody-mediated FRET-based immunosensor," *J. Hazard. Mater.*, vol. 387, p. 121678, Apr. 2020, doi: 10.1016/j.jhazmat.2019.121678.

[139] B. Su *et al.*, "Fluonanobody-based nanosensor via fluorescence resonance energy transfer for ultrasensitive detection of ochratoxin A," *J. Hazard. Mater.*, vol. 422, p. 126838, Jan. 2022, doi: 10.1016/j.jhazmat.2021.126838.

[140] K. D. Wegner *et al.*, "Nanobodies and Nanocrystals: Highly Sensitive Quantum Dot-Based Homogeneous FRET Immunoassay for Serum-Based EGFR Detection," *Small*, vol. 10, no. 4, pp. 734–740, 2014, doi: 10.1002/smll.201302383.

[141] H. S. Afsari *et al.*, "Time-gated FRET nanoassemblies for rapid and sensitive intra- and extracellular fluorescence imaging," *Sci. Adv.*, vol. 2, no. 6, p. e1600265, Jun. 2016, doi: 10.1126/sciadv.1600265.

[142] K. D. Wegner *et al.*, "Nanobodies and Nanocrystals: Highly Sensitive Quantum Dot-Based Homogeneous FRET Immunoassay for Serum-Based EGFR Detection," *Small*, vol. 10, no. 4, pp. 734–740, Feb. 2014, doi: 10.1002/smll.201302383.

[143] H. S. Afsari *et al.*, "Time-gated FRET nanoassemblies for rapid and sensitive intra- and extracellular fluorescence imaging," *Sci. Adv.*, vol. 2, no. 6, p. e1600265, Jun. 2016, doi: 10.1126/sciadv.1600265.

[144] X. Qiu, K. D. Wegner, Y.-T. Wu, P. M. P. van B. en Henegouwen, T. L. Jennings, and N. Hildebrandt, “Nanobodies and Antibodies for Duplexed EGFR/HER2 Immunoassays Using Terbium-to-Quantum Dot FRET,” *Chem. Mater.*, vol. 28, no. 22, pp. 8256–8267, Nov. 2016, doi: 10.1021/acs.chemmater.6b03198.

[145] C. Léger *et al.*, “Picomolar Biosensing and Conformational Analysis Using Artificial Bidomain Proteins and Terbium-to-Quantum Dot Förster Resonance Energy Transfer,” *ACS Nano*, vol. 14, no. 5, pp. 5956–5967, May 2020, doi: 10.1021/acsnano.0c01410.

[146] C. C. S. Pedroso *et al.*, “Immunotargeting of Nanocrystals by SpyCatcher Conjugation of Engineered Antibodies,” *ACS Nano*, vol. 15, no. 11, pp. 18374–18384, Nov. 2021, doi: 10.1021/acsnano.1c07856.

[147] V. Müller *et al.*, “Prognostic and Predictive Impact of Soluble Epidermal Growth Factor Receptor (sEGFR) Protein in the Serum of Patients Treated with Chemotherapy for Metastatic Breast Cancer,” *Anticancer Res.*, vol. 26, no. 2B, pp. 1479–1487, Mar. 2006.

[148] J. Rak, “Extracellular Vesicles – Biomarkers and Effectors of the Cellular Interactome in Cancer,” *Front. Pharmacol.*, vol. 4, 2013, Accessed: Sep. 23, 2023. [Online]. Available: https://www.frontiersin.org/articles/10.3389/fphar.2013.00021

[149] W. A. Hendrickson, A. Pähler, J. L. Smith, Y. Satow, E. A. Merritt, and R. P. Phizackerley, “Crystal structure of core streptavidin determined from multiwavelength anomalous diffraction of synchrotron radiation.,” *Proc. Natl. Acad. Sci.*, vol. 86, no. 7, pp. 2190–2194, Apr. 1989, doi: 10.1073/pnas.86.7.2190.

[150] J. Guo *et al.*, “Conformational Details of Quantum Dot-DNA Resolved by Förster Resonance Energy Transfer Lifetime Nanoruler,” *ACS Nano*, vol. 13, no. 1, pp. 505–514, Jan. 2019, doi: 10.1021/acsnano.8b07137.

[151] E. G. Hofman *et al.*, “EGF induces coalescence of different lipid rafts,” *J. Cell Sci.*, vol. 121, no. 15, pp. 2519–2528, Aug. 2008, doi: 10.1242/jcs.028753.

[152] M. R. Zeronian, S. Doulkeridou, P. M. P. van Bergen en Henegouwen, and B. J. C. Janssen, “Structural insights into the non-inhibitory mechanism of the anti-EGFR EgB4 nanobody,” *BMC Mol. Cell Biol.*, vol. 23, no. 1, p. 12, Mar. 2022, doi: 10.1186/s12860-022-00412-x.

[153] K. R. Schmitz, A. Bagchi, R. C. Roovers, P. M. P. van Bergen en Henegouwen, and K. M. Ferguson, “Structural Evaluation of EGFR Inhibition Mechanisms for Nanobodies/VHH Domains,” *Structure*, vol. 21, no. 7, pp. 1214–1224, Jul. 2013, doi:

10.1016/j.str.2013.05.008.

[154] K. Boeneman Gemmill *et al.*, "Optimizing Protein Coordination to Quantum Dots with Designer Peptidyl Linkers," *Bioconjug. Chem.*, vol. 24, no. 2, pp. 269–281, Feb. 2013, doi: 10.1021/bc300644p.

[155] V. Müller *et al.*, "Prognostic and Predictive Impact of Soluble Epidermal Growth Factor Receptor (sEGFR) Protein in the Serum of Patients Treated with Chemotherapy for Metastatic Breast Cancer," *Anticancer Res.*, vol. 26, no. 2B, pp. 1479–1487, Mar. 2006.

[156] K. E. Sapsford *et al.*, "Kinetics of Metal-Affinity Driven Self-Assembly between Proteins or Peptides and CdSe−ZnS Quantum Dots," *J. Phys. Chem. C*, vol. 111, no. 31, pp. 11528–11538, Aug. 2007, doi: 10.1021/jp073550t.

[157] "Human soluble EGFR ELISA Kit (ab269558) | Abcam." Accessed: Sep. 23, 2023. [Online]. Available: https://www.abcam.com/products/elisa/human-soluble-egfr-elisa-kit-ab269558.html

[158] S. W. Bae, W. Tan, and J.-I. Hong, "Fluorescent dye-doped silica nanoparticles: new tools for bioapplications," *Chem. Commun.*, vol. 48, no. 17, pp. 2270–2282, Jan. 2012, doi: 10.1039/C2CC16306C.

[159] C. Lin, Y. Liu, and H. Yan, "Self-Assembled Combinatorial Encoding Nanoarrays for Multiplexed Biosensing," *Nano Lett.*, vol. 7, no. 2, pp. 507–512, Feb. 2007, doi: 10.1021/nl062998n.

[160] C. Larsson, I. Grundberg, O. Söderberg, and M. Nilsson, "In situ detection and genotyping of individual mRNA molecules," *Nat. Methods*, vol. 7, no. 5, Art. no. 5, May 2010, doi: 10.1038/nmeth.1448.

[161] D. Cai, K. B. Cohen, T. Luo, J. W. Lichtman, and J. R. Sanes, "Improved tools for the Brainbow toolbox," *Nat. Methods*, vol. 10, no. 6, Art. no. 6, Jun. 2013, doi: 10.1038/nmeth.2450.

[162] D. Geißler, L. J. Charbonnière, R. F. Ziessel, N. G. Butlin, H.-G. Löhmannsröben, and N. Hildebrandt, "Quantum Dot Biosensors for Ultrasensitive Multiplexed Diagnostics," *Angew. Chem. Int. Ed.*, vol. 49, no. 8, pp. 1396–1401, 2010, doi: 10.1002/anie.200906399.

[163] I. L. Medintz *et al.*, "Multiplex Charge-Transfer Interactions between Quantum Dots and Peptide-Bridged Ruthenium Complexes," *Anal. Chem.*, vol. 81, no. 12, pp. 4831–4839,

Jun. 2009, doi: 10.1021/ac900412j.

[164] E. Pershagen and K. E. Borbas, “Multiplex Detection of Enzymatic Activity with Responsive Lanthanide-Based Luminescent Probes,” *Angew. Chem. Int. Ed.*, vol. 54, no. 6, pp. 1787–1790, 2015, doi: 10.1002/anie.201408560.

[165] M. Grabolle, P. Kapusta, T. Nann, X. Shu, J. Ziegler, and U. Resch-Genger, “Fluorescence Lifetime Multiplexing with Nanocrystals and Organic Labels,” *Anal. Chem.*, vol. 81, no. 18, pp. 7807–7813, Sep. 2009, doi: 10.1021/ac900934a.

[166] H. H. Cui, J. G. Valdez, J. A. Steinkamp, and H. A. Crissman, “Fluorescence lifetime-based discrimination and quantification of cellular DNA and RNA with phase-sensitive flow cytometry,” *Cytometry A*, vol. 52A, no. 1, pp. 46–55, 2003, doi: 10.1002/cyto.a.10022.

[167] K. Hoffmann, T. Behnke, D. Drescher, J. Kneipp, and U. Resch-Genger, “Near-Infrared-Emitting Nanoparticles for Lifetime-Based Multiplexed Analysis and Imaging of Living Cells,” *ACS Nano*, vol. 7, no. 8, pp. 6674–6684, Aug. 2013, doi: 10.1021/nn4029458.

[168] K. Hoffmann, T. Behnke, M. Grabolle, and U. Resch-Genger, “Nanoparticle-encapsulated vis- and NIR-emissive fluorophores with different fluorescence decay kinetics for lifetime multiplexing,” *Anal. Bioanal. Chem.*, vol. 406, no. 14, pp. 3315–3322, May 2014, doi: 10.1007/s00216-013-7597-3.

[169] Y. Lu *et al.*, “On-the-fly decoding luminescence lifetimes in the microsecond region for lanthanide-encoded suspension arrays,” *Nat. Commun.*, vol. 5, no. 1, Art. no. 1, May 2014, doi: 10.1038/ncomms4741.

[170] Y. Lu *et al.*, “Tunable lifetime multiplexing using luminescent nanocrystals,” *Nat. Photonics*, vol. 8, no. 1, Art. no. 1, Jan. 2014, doi: 10.1038/nphoton.2013.322.

[171] X. Qiu, J. Guo, Z. Jin, A. Petreto, I. L. Medintz, and N. Hildebrandt, “Multiplexed Nucleic Acid Hybridization Assays Using Single-FRET-Pair Distance-Tuning,” *Small*, vol. 13, no. 25, p. 1700332, 2017, doi: 10.1002/smll.201700332.

[172] J. Guo, C. Mingoes, X. Qiu, and N. Hildebrandt, “Simple, Amplified, and Multiplexed Detection of MicroRNAs Using Time-Gated FRET and Hybridization Chain Reaction,” *Anal. Chem.*, vol. 91, no. 4, pp. 3101–3109, Feb. 2019, doi: 10.1021/acs.analchem.8b05600.

[173] J. Xu, J. Guo, N. Golob-Schwarzl, J. Haybaeck, X. Qiu, and N. Hildebrandt, “Single-

Measurement Multiplexed Quantification of MicroRNAs from Human Tissue Using Catalytic Hairpin Assembly and Förster Resonance Energy Transfer," *ACS Sens.*, vol. 5, no. 6, pp. 1768–1776, Jun. 2020, doi: 10.1021/acssensors.0c00432.

[174] "Streptavidine T1 Dynabeads™ MyOne™." Accessed: Sep. 28, 2023. [Online]. Available: https://www.thermofisher.com/order/catalog/product/fr/fr/65601

[175] J. R. Lakowicz, Ed., *Principles of Fluorescence Spectroscopy*. Boston, MA: Springer US, 2006. doi: 10.1007/978-0-387-46312-4.

[176] W. R. Algar, M. G. Ancona, A. P. Malanoski, K. Susumu, and I. L. Medintz, "Assembly of a Concentric Förster Resonance Energy Transfer Relay on a Quantum Dot Scaffold: Characterization and Application to Multiplexed Protease Sensing," *ACS Nano*, vol. 6, no. 12, pp. 11044–11058, Dec. 2012, doi: 10.1021/nn304736j.

[177] X. Fan, I. M. White, S. I. Shopova, H. Zhu, J. D. Suter, and Y. Sun, "Sensitive optical biosensors for unlabeled targets: A review," *Anal. Chim. Acta*, vol. 620, no. 1, pp. 8–26, Jul. 2008, doi: 10.1016/j.aca.2008.05.022.

[178] J. P. Lafleur, A. Jönsson, S. Senkbeil, and J. P. Kutter, "Recent advances in lab-on-a-chip for biosensing applications," *Biosens. Bioelectron.*, vol. 76, pp. 213–233, Feb. 2016, doi: 10.1016/j.bios.2015.08.003.

[179] A. R. Clapp, I. L. Medintz, J. M. Mauro, B. R. Fisher, M. G. Bawendi, and H. Mattoussi, "Fluorescence Resonance Energy Transfer Between Quantum Dot Donors and Dye-Labeled Protein Acceptors," *J. Am. Chem. Soc.*, vol. 126, no. 1, pp. 301–310, Jan. 2004, doi: 10.1021/ja037088b.

[180] J. Shi, F. Tian, J. Lyu, and M. Yang, "Nanoparticle based fluorescence resonance energy transfer (FRET) for biosensing applications," *J. Mater. Chem. B*, vol. 3, no. 35, pp. 6989–7005, Aug. 2015, doi: 10.1039/C5TB00885A.

[181] K. B. Gemmill *et al.*, "Examining the Polyproline Nanoscopic Ruler in the Context of Quantum Dots," *Chem. Mater.*, vol. 27, no. 18, pp. 6222–6237, Sep. 2015, doi: 10.1021/acs.chemmater.5b03181.

[182] Z. Jin and N. Hildebrandt, "Semiconductor quantum dots for in vitro diagnostics and cellular imaging," *Trends Biotechnol.*, vol. 30, no. 7, pp. 394–403, Jul. 2012, doi: 10.1016/j.tibtech.2012.04.005.

[183] W. Zhang, J. Li, H. Lei, and B. Li, "Temperature-dependent Förster resonance energy

transfer from upconversion nanoparticles to quantum dots," *Opt. Express*, vol. 28, no. 8, pp. 12450–12459, Apr. 2020, doi: 10.1364/OE.386601.

[184] A. Yeltik, B. Guzelturk, P. L. Hernandez-Martinez, A. O. Govorov, and H. V. Demir, "Phonon-Assisted Exciton Transfer into Silicon Using Nanoemitters: The Role of Phonons and Temperature Effects in Förster Resonance Energy Transfer," *ACS Nano*, vol. 7, no. 12, pp. 10492–10501, Dec. 2013, doi: 10.1021/nn404627p.

[185] N. V. Slyusarenko, M. A. Gerasimova, V. V. Slabko, and E. A. Slyusareva, "Temperature Sensitivity of Water-Soluble CdTe and CdSe/ZnS Quantum Dots Incorporated into Biopolymer Submicron Particles," *Russ. Phys. J.*, vol. 60, no. 3, pp. 477–484, Jul. 2017, doi: 10.1007/s11182-017-1097-4.

[186] H. C. Gardner, D. E. Gallardo, C. Bertoni, and S. Dunn, "Temperature shifted photoluminescence in CdTe nanocrystals," in *Nanophotonics*, SPIE, Apr. 2006, pp. 166–173. doi: 10.1117/12.661233.

[187] D. Zhou *et al.*, "Conducting the Temperature-Dependent Conformational Change of Macrocyclic Compounds to the Lattice Dilation of Quantum Dots for Achieving an Ultrasensitive Nanothermometer," *ACS Nano*, vol. 7, no. 3, pp. 2273–2283, Mar. 2013, doi: 10.1021/nn305423p.

[188] V. Biju, Y. Makita, A. Sonoda, H. Yokoyama, Y. Baba, and M. Ishikawa, "Temperature-Sensitive Photoluminescence of CdSe Quantum Dot Clusters," *J. Phys. Chem. B*, vol. 109, no. 29, pp. 13899–13905, Jul. 2005, doi: 10.1021/jp050424l.

[189] C. Berney and G. Danuser, "FRET or No FRET: A Quantitative Comparison," *Biophys. J.*, vol. 84, no. 6, pp. 3992–4010, Jun. 2003, doi: 10.1016/S0006-3495(03)75126-1.

[190] P. T. Snee, "The Role of Colloidal Stability and Charge in Functionalization of Aqueous Quantum Dots," *Acc. Chem. Res.*, vol. 51, no. 11, pp. 2949–2956, Nov. 2018, doi: 10.1021/acs.accounts.8b00405.

[191] A. Eychmüller, A. Hässelbarth, L. Katsikas, and H. Weller, "Photochemistry of Semiconductor Colloids. 36. Fluorescence Investigations on the Nature of Electron and Hole Traps in Q-Sized Colloidal CdS Particles," *Berichte Bunsenges. Für Phys. Chem.*, vol. 95, no. 1, pp. 79–84, 1991, doi: 10.1002/bbpc.19910950115.

CHAPTER 9

Panorama du sujet en français

9. Panorama du sujet en français

Le Prix Nobel de Chimie en 2023 a été décerné à Moungi G. Bawendi, Louis E. Brus et Alexei I. Ekimov, qui ont apporté d'importantes contributions à la découverte et à la synthèse des points quantiques (QDs) et ont "added colour to nanotechnology" [1]. Ces nanoparticules de de taille réduite, fluorescents et uniques offrent des applications innovantes dans divers domaines et jouent un rôle crucial dans le développement de la science des matériaux, de la photonique, des technologies de l'énergie et des sciences de la vie.

En raison de l'effet de confinement quantique, les QDs présentent des propriétés photophysiques exceptionnelles supérieures aux colorants organiques conventionnels [2], notamment ils possèdent des coéfficients d'extinction élevés, des pics d'émission photoluminescence (PL) étroits et symétriques, et des longueurs d'onde d'émission PL qui dépendent de la taille, etc., ce qui en fait des alternatives préférées aux colorants traditionnels pour la biosensibilité et l'imagerie [3], [4]. Outre le remplacement des fluorophores organiques, les QDs ont également suscité un intéret croissant en tant que candidats polyvalents de transfert d'énergie (TE) (donneurs ou accepteurs) dans les milieux biologique à l'échelle nanométrique [5]. En raison du ratio surface-volume élevé des QDs, des biomolécules fonctionnelles (par exemple, des protéines, des anticorps, des ADN à brin unique) et/ou des matériaux luminescents (donneurs ou accepteurs de TE) peuvent être conjugués aux QD, ce qui permet une detection à l'échelle nanométrique du milieu biologique [5], [6].

Dans les essais basés sur le TE, le Förster resonance energy transfer (FRET) est devenu l'une des techniques les plus prometteuses pour la biosensibilité en raison de sa grande sensibilité à la distance à l'échelle de l'interaction biomoléculaire (environ 1-20 nm) [7]. Les QDs se sont démontrés être d'excellents donneurs FRET pour une grande variété de fluorophores organiques, de protéines fluorescentes, de polymères et de nanoparticules métalliques (NPs) [8]–[10]. Cependant, les fluorophores organiques et les protéines fluorescentes souffrent souvent d'une faible photostabilité, de l'auto-quenching, et de l'influence de l'auto fluorescencede fond. Pour surmonter ces inconvénients, des paires de FRET constituées de composés à base de lanthanides ou de donneurs de nanoparticules et de QD accepteurs ont été proposées et développées [11], [12]. Par rapport aux colorants organiques

et aux protéines fluorescentes, les QDs présentent une grande photostabilité, une luminosité élevée. De plus les donneurs à base de lanthanides possèdent des durée de vie PL extrêmement longue (jusqu'aux milisecondes) [13], [14], ce qui permet la détection à résolution temporelle (TR) ou la détection temporellement retardée (TG) supprimant ainsi toute auto-fluorescence defond (à l'échelle des ns). En effet, la durée de vie de la photoluminescence des donneurs FRET non luminescents ou des accepteurs FRET sensibilisés peut être ajustée en fonction des efficacités FRET, ce qui offre un grand potentiel pour le multiplexage temporel. [15]. Par ailleurs, les sondes lanthanides et les QDs ont des pics d'émission étroits et distincts, ce qui offre la possibilité d'un multiplexage spectral en utilisant différents QDs comme accepteurs multiples. [16].

Plusieurs concepts sophistiqués de biosensibilité luminescente à base de lanthanides et de QDs ou de sondages multiples ont été présentés [17]–[19]. Bien que les tests de concept aient montré des caractéristiques très prometteuses pour des applications de détection avancées, leur optimisation, simplification et adaptation à une utilisation quotidienne dans un large éventail d'applications sont des défis qui restent à relever. De plus, l'influence des changements des conditions (par exemple, la température) et des interactions biologiques sur les propriétés photophysiques et de transfert d'énergie des lanthanides à la surface des nanoparticules a été largement sous-exploitée. Par conséquent, l'objectif de cette thèse est d'étudier les interactions biomoléculaires (en prenant les réactions des protéines et l'hybridation de l'ADN comme cas représentatifs) à la surface des QDs par des essais FRET de Lanthanide-to-QD (un complexe de terbium a été utilisé comme composé typique à base de lanthanides) et l'effet de la température sur les systèmes de FRET à base de QD.

La thèse se compose deneuf chapitres. L'introduction (**Chapitre 1**), est suivie d'une présentation du contexte scientifique de la recherche (**Chapitre 2**) d'une description de la théorie de FRET, les applications de FRET, les lanthanides et les QDs. Les **Chapitres 3**, **4** et **5** abordent trois études individuelles, comprenant une introduction, des matériaux et des méthodes, des résultats et des discussions, ainsi que des conclusions. Le résumé et les perspectives de l'ensemble du travail sont abordés au **Chapitre 6**, suivi des abréviations, de la bibliographie et de le panorama du sujet.

Dans la première étude, les interactions des protéines à la surface des QD basées sur le

FRET du complexe terbium-QD ont été étudiées en prenant le récepteur du facteur de croissance épidermique (EGFR, un biomarqueur important pour divers types de cancers humains) [20], [21], comme modèle de protéine. Deux nano-anticorps ingénieux de petite taille (NB1 et NB2) dirigés contre l'EGFR ont été produits avec différentes marquages C-terminales (marqueurs de hexahistidine (His_6), biotine, et cystéine (Cys)). Nous montrons qu'ils peuvent être efficacement attachés à trois des QDs biocompatibles les plus couramment utilisés avec trois coatings de surface courants, à savoir des ligands zwitterioniques compacts (CL4), le polyéthylène-glycol amino (PEG) et la streptavidine (sAv), respectivement. Pour démontrer la fonctionnalité de biosensibilité de cet outil polyvalent de bioconjuguaison, trois immunoessais sandwich FRET sans rinçage et rapides pour la quantification de l'EGFR ont été développés. Comme le montre la **Figure 1.1A**, les NB2 sont marqués avec des marquage d'His_6 (NB2-H), de Cys (NB2-C) et de biotine (NB2-B), respectivement, tandis que le NB1 est marqué avec le complexe Lumi4-Tb (Tb-NB1). Ensuite, les NB2-H, NB2-B et NB2-C sont respectivement attachés sur QD625-CL4, QD705-sAv et QD705-PEG, pour former les conjugués NB2-H-QD625-CL4, NB2-B-QD705-sAv et NB2-C-QD705-PEG. Étant donné que le NB1 et le NB2 se fixent à différents domaines de l'EGFR de manière non compétitive, leurs conjugués ont été utilisés avec succès pour détecter le récepteur du facteur de croissance épidermique soluble (sEGFR, un biomarqueur pronostique et prédictif du cancer du sein métastatique) dans des essais immunologiques en sandwich, avec des limites de détection (LOD) similaires de 0,5 ± 0,2 nM (NB2-C-QD705-PEG), 0,7 ± 0,2 nM (NB2-B-QD705-sAv) et 0,8 ± 0,2 nM (NB2-H-QD625-CL4) pour le sEGFR, respectivement. Nous avons ensuite développé un nouveau concept de biosensibilité (**Figure 1.1B)**, dans lequel les nanocorps marqués His_6 (NB1-H) ont été déplacés de la surface des QD par la liaison non compétitive du NB1 à l'EGFR. Ce nouveau modèle d'essai, qui ne nécessitait qu'un seul type de nanocorps et aucune bioconjugaison des QD, a été utilisé pour la quantification du sEGFR et de la variante soluble du récepteur du facteur de croissance épidermique III (sEGFRvIII, un biomarqueur pronostique pour le glioblastome). La limite de détection de 80 ± 20 pM (16 ± 4 ng/mL) était trois fois inférieure à la concentration seuil en clinique du sEGFR et jusqu'à 10 fois inférieure par rapport aux trois essais FRET en sandwich conventionnels mentionnés ci-dessus qui nécessitaient une paire de nanocorps différents. L'essai de déplacement de nanocorps réduit considérablement les coûts et

le main-doeuvre (pour le criblage et la production d'anticorps et la bioconjugaison), facilite grandement l'assemblage et le stockage des kits d'essai (uniquement un type de conjugué Tb-NB et un type de QD non marqué), offre une analyse rapide (mélanger et mesurer) et peut quantifier des biomarqueurs pertinents à des concentrations cliniquement pertinentes.

Ma contribution à cette étude inclut la conception expérimentale, la préparation des conjugués NB-Tb, l'optimisation des conditions de réaction, la réalisation des expériences d'essai de déplacement, l'analyse des données et leur interprétation, ainsi que la rédaction du manuscrit. Dr. Yu-tang Wu a contribué à la préparation des conjugués NB-QD et aux expériences d'essai en sandwich. Sofia Doulkeridou a préparé les nanocorps. Prof. Dr. Xue Qiu a aidé à la conception des études. Dr. Kimihiro Susumu a préparé les QD625-CL4. Tous les auteurs ont contribué à la rédaction et à la révision du manuscrit et ont approuvé sa version finale pour la revue (**Ruifang Su**, Yu-Tang Wu, Sofia Doulkeridou, Xue Qiu, Thomas Just Sørensen, Kimihiro Susumu, Igor L. Medintz, Paul M. P. van Bergen en Henegouwen, and Niko Hildebrandt. A Nanobody-on-Quantum Dot Displacement Assay for Rapid and Sensitive Quantification of the Epidermal Growth Factor Receptor (EGFR). *Angewandte Chemie International Edition* **2022**, 61(33), e202207797. Article 4 dans la liste des publications originales).

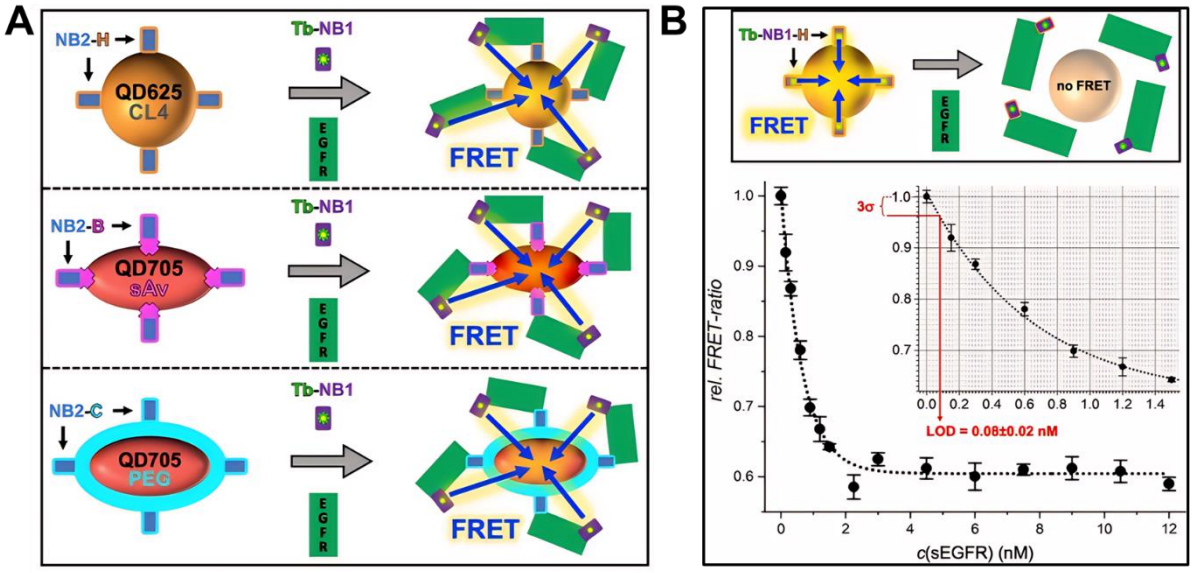

Figure 1.1. Représentation schématique des immunoessais pour la détection de l'EGFR. **(A)** Principe des immunoessais sandwich FRET basés sur les nanocorps (NB) Tb-to-QD. **(B) En haut** : Principe des immunoessais de déplacement de nanocorps Tb-to-QD FRET. **En bas** : Courbes de calibration des

immunoessais FRET de déplacement de nanocorps avec une limite de détection (LOD) de 0,08 ± 0,02 nM de sEGFR.

Dans la deuxième étude, une stratégie de multiplexage temporel est présentée pour la détection des cibles d'ADN basée sur la mesure PL TG de trois différentes sondes FRET (Lumi4-Tb) Tb-QD avec des décroissances PL temporellement distinctes réglées par la distance Tb-QD. Différentes sondes FRET Tb-QD ont été fonctionnalisées avec différentes séquences peptide-cADN (partie de la séquence complémentaire de l'ADN cible spécifique) et utilisées comme sondes PL distinctes. Des microbilles magnétiques (MB) ont été fonctionnalisées avec d'autres séquences cADN (une autre partie de la séquence complémentaire de l'ADN cible spécifique) via la réaction biotine-streptavidine. En présence des ADN cibles correspondants, différentes sondes Tb-QD peuvent être immobilisées sur les MB par hybridation d'ADN entre la séquence peptide-cADN, l'ADN cible et l'ADN cible sur les MB (**Figure 1.2 gauche**). Après séparation magnétique et resuspension, tout le signal de fond des sondes FRET Tb-QD-peptide-cADN libres peut être éliminé, et les mesures TG des sondes Tb-QD sur les MB dans des fenêtres temporelles distinctes après excitation pulsée permettent une détection sans autofluorescence, sensible et sélective des différentes cibles d'ADN (**Figure 1.2 droite**). Les résultats montrent que les intensités PL des différentes sondes FRET dans les différentes fenêtres temporelles augmentent avec la concentration croissante de l'ADN cible dans chaque essai de détection individuel. Les courbes d'étalonnage des essais ont été obtenues en traçant l'intensité PL TG du QD accepteur sensibilisé par FRET de chaque sonde en fonction des concentrations cibles correspondantes. Les plages de concentration de détection linéaire des ADN cibles 1, 2 et 3 sont de 0,625 pM à 0,375 nM, de 2,5 pM à 0,5 nM et de 6,25 pM à 2 nM, et les LODs sont respectivement de 0,56 pM, 0,94 pM et 10,3 pM. Ces sensibilités permettent de distinguer des différences de concentration de quelques pM sur toute la plage de concentrations dynamiques. Le concept de multiplexage temporel a été utilisé avec succès pour la récupération sélective, sensible et précise des trois ADN différents à des concentrations allant de faibles picomolaires à nanomolaires à partir de onze échantillons différents.

Ma contribution à cette étude comprend la conception et la réalisation des expériences, l'analyse des données et la rédaction du manuscrit. Dr. Kimihiro Susumu a préparé les QD625

(modifiés avec des ligands CL4). Tous les autres auteurs ont contribué à la conception des expériences et ont fourni des conseils. Le manuscrit est actuellement en préparation. (**Ruifang Su**, Kimihiro Susumu, Igor L. Medintz, Thomas Just Sørensen, and Niko Hildebrandt, Multiplexed picomolar nucleic acid sensing using time-resolved terbium-to-quantum dot FRET. Article 2 dans la liste des publications originales).

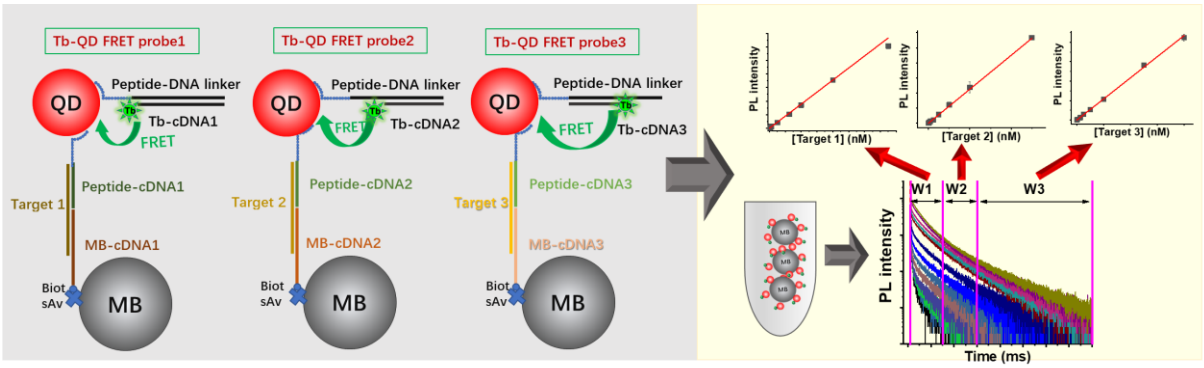

Figure 1.2. Représentation schématique du triplexage temporel de l'ADN basé sur la FRET Tb-QD. **À gauche:** En présence d'ADN cible, les sondes de FRET Tb-vers-QD composées de peptides-ADNc et les ADNc sur les billes magnétiques vont s'hybrider avec l'ADN cible pour former les complexes Tb-QD-ADN-MB. **À droite:** Après séparation magnétique et resuspension, la mesure de PL TG à partir de trois fenêtres temporelles (W1, W2 et W3) des sondes Tb-QD sur les billes magnétiques permet de réaliser la quantification spécifique des cibles d'ADN.

Dans la troisième étude, la réponse à la température des QDs largement utilisés et dispersible en milieu aqueux (QDs core-shell à base de CdSe/ZnS, fonctionnalisés avec des ligands compacts à base d'acide dihydrolipoïque (DHLA)) a été analysée en mesurant leurs spectres d'absorption et d'émission PL à différentes températures. En utilisant les QDs à la fois comme nanoplateformes et donneurs ou accepteurs de FRET, deux essais prototypiques de détection basés sur le FRET ont été développés comme illustré dans la **Figure 1.3**. Dans les deux systèmes de FRET, des peptides-ADN étaient attachés à la surface des QDs grâce à une coordination métal-polyhistidine. Les ADN marqués au Cyanine 5 (Cy5) ou au Lumi4-Tb-NHS (Tb) pouvaient s'hybrider spécifiquement avec la séquence d'ADN dans le peptide-ADN, créant ainsi des complexes de FRET QD-peptide-dsDNA-Cy5/Tb. La réponse à la température des QDs et son effet sur les performances des deux essais de détection ont été étudiés en combinant des mesures PL en régime stationnaire et en régime TR des signaux de FRET basés sur les QDs. Les résultats montrent que l'intensité PL des QDs diminue et que la position du pic d'émission

se déplace vers le rouge avec l'augmentation de la température de 10 à 80 °C, ce qui démontre une excellente réversibilité. Un traitement thermique continu induit une extinction partielle irréversible de la PL des QDs en raison de la réaction d'oxydation de la surface,de la précipitation et de l'agrégation des particules (lorsque la température dépasse 60 °C). L'effet de la température sur les essais basés sur les QDs peut être éliminé en utilisant un format de FRET ratiométrique (le FRET ratio comme signal), ce qui permetune détection efficace des cibles d'ADN indépendamment de la température. L'intensité PL des donneurs ou accepteurs de QD dans les essais de FRET reste sensible à la température, ce qui peut être utilisé pour une détection simultanée de la température pendant la quantification de l'ADN. En combinant le format d'essai de FRET ratiométrique avec la capacité de détection de la température des QDs, il est possible réaliser une double détection de cible et de la températureLes résultats mettent en évidence l'importance du contrôle de la température pour les essais PL basés sur les QDs et fournissent des informations importantes pour leur application dans le domaine des sciences de la vie. Le développement de la stratégie de détection double cible/température biologique est propice à l'expansion des applications des systèmes de FRET dans les domaines biomédicaux et à nano-surfaces.

Ma contribution à cette étude inclut la conception et la réalisation des expériences, l'analyse des données et la rédaction du manuscrit. Dr. Kimihiro Susumu a préparé les QD625 (modifiés avec des ligands CL4). Tous les autres auteurs ont contribué à la conception de l'expérience et ont fourni des conseils. Le manuscrit est actuellement en préparation. (**Ruifang Su**, Nicolaj Kofod, Kimihiro Susumu, Igor L. Medintz, Niko Hildebrandt, and Thomas Just Sørensen. Quantum dot-based FRET assays for simultaneous temperature-DNA sensing. Article 1 dans la liste des publications originales).

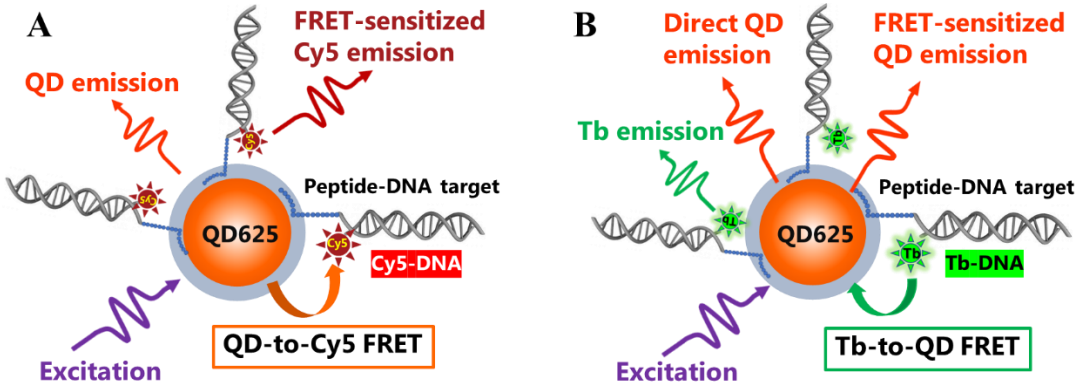

Figure 1.3. Principes du FRET basé sur les QD. **(A)** L'ADN marqué au Cy5 s'hybride à l'ADN du peptide fixé à la surface des QD625, ce qui entraîne le FRET QD-vers-Cy5. **(B)** Dans une conception similaire, l'hybridation de l'ADN-Tb à l'ADN du peptide entraîne le FRET Tb-vers-QD.

Exploration des interactions nanosurface-biologiques/environnementales par Förster resonance energy transfer des complexes de lanthanides vers les points quantiques

Mots-clés: points quantiques, terbium, FRET, assai immunologique, multiplexage, détection de la température

Résumé: En raison des propriétés photophysiques uniques des points quantiques (QD) et des matériaux de lanthanides (Ln), leur application dans le Förster resonance energy transfer (FRET) suscite un intérêt particulier pour la détection les interactions biologiques à l'échelle nanométrique et la détection de milieux biochimiques. Cette thèse se concentre sur le développement de biosenseurs pour les interactions biomoléculaires et la détection des changements de conditions basés sur le FRET de Ln vers les QD. Pour la détection représentative des cibles de protéines, un kit de bibliothèque de conjugués nanocorps-marqueurs-QD a été développée, et un essai immunologique de déplacement simplifié et sensible a été établi. La détection simultanée de plusieurs cibles étant très demandée, une méthode de multiplexage par division temporelle basée sur la FRET déclenchée en fonction du temps a été mise au point en utilisant des ADN comme analytes représentatifs. De plus, en combinant le format d'essai FRET ratiométrique avec la sensibilité à la température des QDs, un concept de détection double ADN/température a été démontré. Les découvertes de ce travail sont propices à l'extension des stratégies de FRET de Ln vers les QDs dans le multiplexage d'ordre supérieur des interactions biologiques/environnementales en sciences de la vie.

Probing nanosurface-biological/environment interactions by Förster resonance energy transfer from lanthanide complexes to quantum dots

Keywords: quantum dots, terbium, FRET, immunoassay, multiplexing, temperature sensing

Abstract: Due to the unique photophysical properties of quantum dots (QDs) and lanthanide (Ln) materials, their application in Förster resonance energy transfer (FRET) is of particular interest for nanoscale biological interactions and environmental sensing. This thesis focuses on the development of biosensors for biomolecular interactions and environmental change probing based on Ln-to-QD FRET. For representative protein target sensing, a nanobody-tag-QD conjugate toolkit was developed and a simplified and sensitive displacement immunoassay was established. Since the simultaneous detection of multiple targets is highly demanded, a time-gated FRET-based temporal multiplexing method was then developed by taking DNA as the representative analytes. Moreover, by combining the ratiometric FRET assay format with the temperature sensitivity of QDs, a DNA/temperature dual sensing concept was demonstrated. The discoveries of this work are conducive to expanding the Ln-to-QD-based FRET strategies into higher-order multiplexing of biological/environmental interactions in the life sciences.